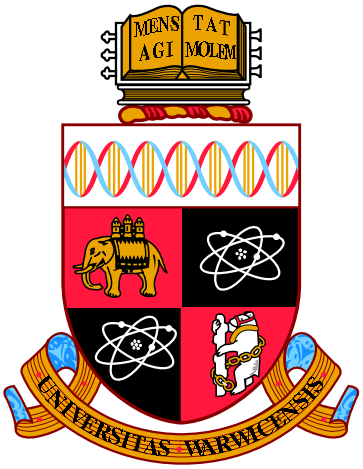

Observations of Remnant Planetary Systems at White Dwarfs

by

David John Wilson

Thesis

Submitted to the University of Warwick

for the degree of

Doctor of Philosophy

Department of Physics

September 2017

THE UNIVERSITY OF WARWICK

Some say the world will end in fire,
Some say in ice.
From what I've tasted of desire
I hold with those who favour fire.
But if it had to perish twice,
I think I know enough of hate
To say that for destruction ice
Is also great
And would suffice.

Robert Frost

Contents

Acknowledgments

0.1 Personal acknowledgements

This PhD would not be possible without many people, most of whom I will probably forget to mention. Sorry.

Foremost in those I have remembered is my supervisor, Professor Boris Gänsicke, who, since convincing me that white dwarfs were interesting over a free lunch, has never been anything but supportive and encouraging, except when I made terrible plots, which was probably a good thing, and when I wrote overly long sentences, which I still think have their merits. Thanks also to my various collaborators, especially to Detlev Koester for being patient when my physics was incorrect and to Jay Farihi for being impatient when my spelling was incorrect.

Thank you also to all of my fellow PhD students at Warwick for their friendship, support and advice, along with a steady supply of boardgames and other distractions. Particular thanks to Mark for helping me pretend I know how to code.

Thank you to the Astrobites Collaboration for letting me write about space (and/or microwaves) on the internet and to astronomy Twitter for connecting me to a wider world.

Finally, thank you to my family and above all my parents, for feeding and clothing me for most of my life, supplying me with a steady stream of books with pictures of space rockets, and for taking me outside one night in 1997 to look at Comet Hale-Bopp. I promise to continue to do my best to never get a real job.

0.2 Institutional acknowledgements

The research leading to these results has received funding from the European Research Council under the European Union's Seventh Framework Programme (FP/2007-2013) / ERC Grant Agreement n. 320964 (WDTracer).

This thesis has made use of observations from the following observatories and institutions:

The NASA/ESA *Hubble Space Telescope*, obtained at the Space Telescope Science Institute, which is operated by the Association of Universities for Research in Astronomy, Inc., under NASA contract NAS 5-26555. These observations are associated with program IDs 11561, 12169, 12869, 12474 and 13719.

SDSS-III, funding for which has been provided by the Alfred P. Sloan Foundation, the Participating Institutions, the National Science Foundation, and the U.S. Department of Energy Office of Science.

The William Herschel Telescope on the island of La Palma, maintaned by the Isaac Newton Group in the Spanish Observatorio del Roque de los Muchachos of the Instituto de Astrofsica de Canarias.

The Gemini North Telescope under program GN-2010A-Q-94.

The Gemini South Telescope under program GS-2010A-Q-17.

ESO Telescopes at the La Silla Paranal Observatory under programme IDs 093.D-0838(A),087.D-0139(C),091.D-0296(A), 386.C-0218(E), 081.C-0466(A), 082.C-0495(A), 383.C-0695(A), 386.C-0218(B) and 094.D-0344(A).

The W.M. Keck Observatory, which is operated as a scientific partnership among the California Institute of Technology, the University of California and the National Aeronautics and Space Administration. The Observatory was made possible by the generous financial support of the W.M. Keck Foundation. I wish to recognize and acknowledge the very significant cultural role and reverence that the summit of Mauna Kea has always had within the indigenous Hawaiian community. I am most fortunate to have the opportunity to conduct observations from this mountain.

This research made use of Astropy, a community-developed core Python package for Astronomy (Astropy Collaboration, 2013).

Declarations

I declare that this thesis has not been submitted in any previous application for a higher degree.

Chapters 1, 2 and 7 explain the background to the science, describe the methods used and summarise the thesis respectively, and are entirely my own work. The remaining chapters report the scientific results of the thesis. Three of the chapters have already been published in the literature and the fourth is in preparation for submission. In all four cases I performed the bulk of the scientific analysis and am lead author on the resulting papers.

Chapter 3 was published as Wilson et al. (2014). Boris Gänsicke contributed to the analysis and provided observational data and Detlev Koester provided the white dwarf model atmospheres. Additional observations were provided and/or carried out by Roberto Raddi, Elmé Breedt, John Southworth and Steven Parsons.

Chapter 4 was published as Wilson et al. (2015). Boris Gänsicke contributed to the analysis and provided observational data, Detlev Koester provided the white dwarf model atmospheres and Odette Toloza extracted the time-tag lightcurve. Additional observations were provided and/or carried out by Anna Pala, Elmé Breedt and Steven Parsons.

Chapter 5 was published as Wilson et al. (2016). Boris Gänsicke contributed to the analysis and provided observational data, Jay Farihi assisted with the analysis and Detlev Koester provided white dwarf model atmospheres.

Chapter 6 is based on data from a *Hubble Space Telescope* program of which I am PI, Program ID 13719. Boris Gänsicke and Jay Holburg contributed to the analysis, and Detlev Koester and Simon Preval provided model spectra. Additional observations were provided by Jay Farihi, P. Wilson Cauley, Claudia Belardi, Knox Long, Paul Chote, Mark Hollands, Seth Redfield, Matt Burleigh, Martin Barstow and Sarah Casewell.

Abstract

The detection of remnant planetary systems at white dwarfs allows the end stages of planetary evolution to be explored observationally. This thesis presents observations of white dwarfs and describes the contributions they make to planetary science.

Firstly, white dwarf science probes the end states of the majority of known planetary systems, including the Solar system. In Chapter 3 I present the discovery of strongly variable emission lines from gas in a debris disc around the white dwarf SDSS J1617+1620. Time-series spectroscopy obtained during the period 2006–2014 has shown the appearance and then complete disappearance of strong double-peaked Ca II emission lines. These observations represent unambiguous evidence for short-term variability in the debris environment of evolved planetary systems. Possible explanations for this extraordinary variability include the impact onto the debris disc of a single small rocky planetesimal, or interactions between material in a highly eccentric debris tail.

I also use observations of white dwarfs to contribute to exoplanet science more generally. Metal pollution from planetary debris is visible in spectra of white dwarfs, providing the only technique to directly measure the bulk chemical composition of rocky extrasolar material. Chapter 4 presents a detailed study of the metal-polluted white dwarf SDSS J0845+2257, using high-resolution *HST*/COS and VLT spectroscopy to detect hydrogen and eleven metals originating in an orbiting debris disc. The chemistry of the debris is broadly similar to the Earth, but enhanced abundances of core material (Fe, Ni) suggest that the planetesimal from which the debris formed may have lost a portion of its mantle.

Conversely, in Chapter 5 I focus on the detection of just carbon and oxygen, but at 16 different white dwarfs to search for hypothetical "carbon planets". I find no evidence for carbon-rich planetesimals, with C/O$<$ 0.8 by number in all 16 systems. I place an upper limit on the occurrence of carbon-rich systems at $<$ 17 percent. The range of C/O of the planetesimals is consistent with that found in the Solar System.

White dwarfs can also be fascinating objects in their own right. In Chapter 6 I present *HST* observations of the mysterious white dwarf GD 394, a hot, extremely metal-polluted white dwarf. Extreme ultraviolet observations in the mid 90s revealed a 1.15 day periodicity with a 25 per cent amplitude, hypothesised to be due to a surface accretion spot. I obtained phase-resolved *HST*/STIS high-resolution FUV spectra of GD 394 that sample the entire period, along with a large body of supplementary data. I use these data to test the hypothesis of an accretion spot, search for variability in accretion rates over decades-long timescales, and probe the immediate circumstellar environment of GD 394.

Abbreviations

ADS ... Astrophysics Data System

COS ... Cosmic Origins Spectrograph

DRx ... Data Release x

ESO ... European Southern Observatory

EUV ... Extreme Ultraviolet

EUVE ... *Extreme Ultraviolet Explorer*

FORS ... Focal Reducer and Low Dispersion Spectrograph

FUSE ... *Far Ultraviolet Spectroscopic Explorer*

FUV ... Far Ultraviolet

FWZI ... Full Width-Zero Intensity

GALEX ... *Galaxy Evolution Explorer*

HST ... *Hubble Space Telescope*

IRAF ... Image Reduction and Analysis Facility

IR ... Infrared

ISIS ... Intermediate Dispersion Spectrograph and Imaging System

$\log g$ ... Logarithmic acceleration due to gravity

LSST ... Large Synoptic Survey Telescope

MJD ... Modified Julian Date

NIR ... Near Infrared

NUV ... Near Ultraviolet

SDSS ... Sloan Digital Sky Survey

SPY ... ESO Supernova Ia Progenitor Survey

$T_{\rm eff}$ ... Effective temperature

UVB ... Ultraviolet/Blue

UVES ... Ultraviolet and Visual Echelle Spectrograph

VLT ... Very Large Telescope

VIS ... Visible

WD ... White Dwarf

WHT ... William Herschel Telescope

The use of *italics* denotes a spacecraft. Chemical elements and molecules are referred to by their standard chemical symbols throughout, e.g. C ... Carbon.

Chapter 1

Introduction

"This is what you must remember: the ending of one story is just the beginning of another. This has all happened before, after all. People die. Old orders pass. New societies are born. When we say the world has ended, it's usually a lie, because the planet is just fine.

But this is the way the world ends.
This is the way the world ends.
This is the way the world ends.
For the last time"

N.K. Jemisin, The Fifth Season

1.1 The post-main sequence evolution of the Solar system

Around seven and a half billion years from now, Planet Earth will most likely cease to exist. This is not the wild imagining of an apocalyptic prophet, but a prediction born of centuries of scientific inquiry. Of course, there is nothing to stop humanity, or whoever follows us, destroying Earth before then, but that 7.5 Gyr figure represents a hard deadline, an ending penned into the Universe the moment the Sun left its stellar nursery.

Schröder & Connon Smith (2008) provide the latest model of the fate of the Solar system planets, which is a function of both the mass of the Sun and the size of each planet's orbit. The Sun is currently prevented from gravitational collapse by radiation pressure generated by core fusion of hydrogen into helium, placing it on the "Main Sequence" of stellar evolution (Figure 1.1). When the Sun reaches an age of 10 Gyr, 5.4 Gyr from now, that core hydrogen will have been exhausted, and fusion will move on to successive shells of hydrogen around the now helium core. The core will contract, but the outer envelope will expand outwards for over 2 Gyr to a maximum of 1.19 au, 256 times its current radius. Whilst the Sun's effective temperature ($T_{\rm eff}$) will drop from around 5750 K to a low point of 2600 K, its luminosity will increase by a factor of 2700 due to the increased surface area, moving up the Red Giant Branch (RGB) of the Hertzsprung-Russel (HR) diagram (Figure 1.1).

Mercury and Venus will certainly be engulfed and destroyed, but the fate of the Earth is less certain. The high luminosity of the Sun during the RGB will drive a greatly increased Solar wind, such that the Sun may have lost a third of its current mass by the tip of the RGB. To conserve angular momentum the Earth's orbit will have expanded to as much as 1.7 au, leading Sackmann et al. (1993) to conclude that the Earth will survive this phase. However, they neglected tidal interactions between the expanding Sun and Earth, which when accounted for predict that the Earth is indeed engulfed around 7.59 Gyr from the present, near the tip of the Sun's RGB phase (Schröder & Connon Smith, 2008). Only by a combination of the extreme uncertainties in models of the Solar mass loss rate, maximum size and strength of the tidal forces does Earth escape destruction (Veras, 2016a).

The Sun will reach a maximum radius soon after the engulfment of the Earth, then begin to contract back to eleven times its current radius before the ignition of core helium drives a second phase of expansion along the asymptotic giant branch (AGB). Without sufficient remaining envelope mass to burn, the Sun will not exceed its previous maximum radius on the AGB, so Mars and the four gas giants will not be threatened with engulfment.

At the end of the AGB the Sun will have lost half of its initial mass. The semi-major axes of the remaining planets will therefore have doubled to conserve angular momentum, although as the mass loss time scale of the Sun is long in comparison with the planets'

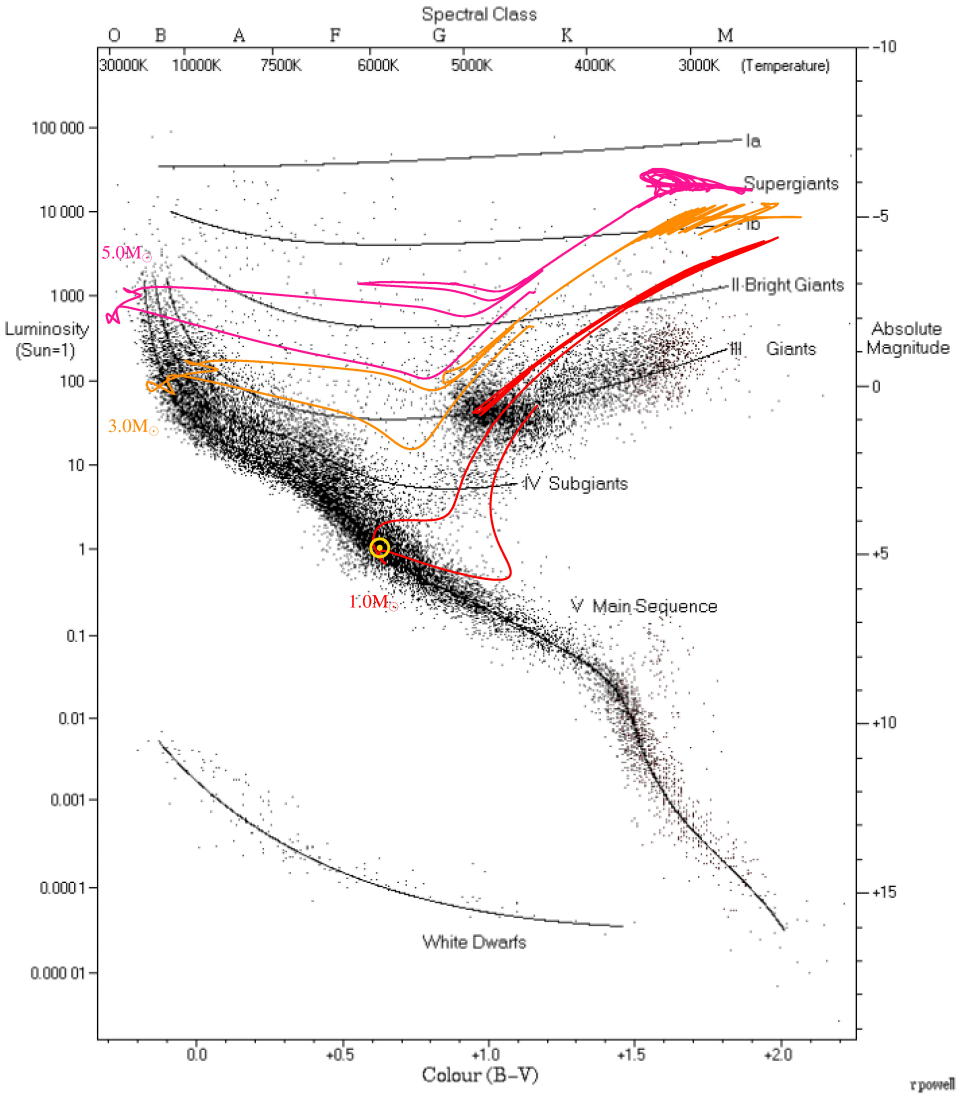

Figure 1.1: Hertzsprung-Russel (HR) diagram showing the luminosity/magnitude against colour/T_{eff} of stars at different stages of their life cycles. Overplotted are MESA stellar models retrieved from the MIST database (Dotter, 2016; Choi et al., 2016) for stars with 1, 3 and 5 $M_{\odot}$. The current position of the Sun is shown in yellow. Adapted from an HR Diagram by Richard Powell under a CC License.

orbital periods such expansion will be adiabatic, and the planets will retain both their (near) circular orbits and existing period ratios (Veras, 2016a). Once the stellar mass loss has ended, Mars and the giant planets will remain stable in their new orbits for many Gyr (Duncan & Lissauer, 1998), although this rosy outlook may be challenged if the hypothetical Planet 9 exists (Batygin & Brown, 2016; Veras, 2016b). Conversely, the increased insolation during the giant branches will almost totally destroy asteroids and other planetesimals out to around 7 au, either via thermal evaporation or by spinning them up via the YORP mechanism until they become internally unbound (Veras et al., 2014a). The stability of the Kuiper belt dwarf planets has not been modelled in detail, although Duncan & Lissauer (1998) predict that Pluto is likely destroyed by an encounter with Neptune.

At the end of the AGB the helium at the core of the Sun will have entirely fused into carbon and oxygen, and the remaining mass of the Sun will not generate enough pressure to fuse these into heavier elements. Without the outward pressure from nuclear fusion to balance the infalling mass, the core will shrink until it is held up by electron degeneracy pressure, reaching a final radius of $\approx 1 R_{\oplus}$ and mass $\approx 0.5\,M_{\odot}$. This and similar stellar remnants are known as white dwarfs.

We are left with the following picture of the Solar system ~8 Gyr from now: A tiny, slowly cooling white dwarf; a gap of ~3 au left by the engulfed planets; Mars at approximately twice its current orbital separation; and finally the gas giants, also on expanded orbits, along with a vast number of planetesimals and other debris (Veras, 2016a).

Beyond providing a scientifically rigorous version of the apocalypse myths found throughout human culture, what is the relevance of the future described here? Far from being an interesting but theoretical endeavour, modelling the end stages of the Solar system has implications for current *observational* astronomy. Evolution into a white dwarf is not just the end-stage of the Sun, but of over 95 per cent of stars, including the vast majority of the thousands of stars now known to host extrasolar planetary systems. Furthermore, many planet-hosting stars have already undergone such evolution into white dwarfs, and their remnant planetary systems are not only observable, but can be use to explore aspects of planetary science that are inaccessible via observations of main sequence systems.

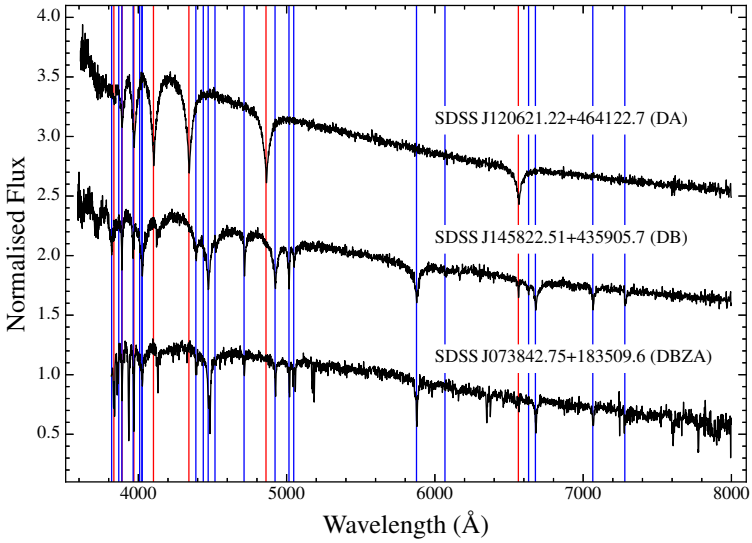

Figure 1.2: Example SDSS spectra of hydrogen atmosphere (DA), helium atmosphere (DB) and metal-polluted (D*Z) white dwarfs retrieved from the Montreal White Dwarf Database (MWDD, Dufour et al., 2017). The red and blue lines show the wavelengths of hydrogen and helium absorption features respectively, with additional lines in the third spectrum due to metal pollution.

1.2 Physical properties of white dwarfs

In order to understand the observational signatures of remnant planetary systems, some discussion of white dwarf physical properties is required. White dwarfs are the end points of stellar evolution for all stars below 8–11 $M_{\odot}$, depending on metallicity (Siess, 2007), which includes roughly 95 per cent of all stars (Althaus et al., 2010) and nearly all confirmed planet host stars[1].

1.2.1 Classification

White dwarfs are classified primarily by their spectral absorption features. Table 1.1 lists all the designations used (McCook & Sion, 1999; Koester, 2013). Of most relevance to this thesis are the DA and DB classes, which have spectra dominated by hydrogen or helium lines respectively. The dominant lines are mostly, but not always, equivalent to the most abundant atomic species in their photospheres: As hydrogen lines are stronger than helium for a given abundance, some white dwarfs classified DA are in fact helium dominated (see for e.g. Kilkenny, 1986; Gentile Fusillo et al., 2017). White dwarfs with both hydrogen and helium lines are classified DAB or DBA, depending on which lines are stronger. If

[1]A notable exception are the pulsar planets (Wolszczan & Frail, 1992).

Table 1.1: White dwarf spectral classifications (Koester, 2013, MWDD). Combinations are also used: e.g. DABZ for a hydrogen atmosphere with helium and metal lines.

Spectral type	Definition
DA	Only hydrogen lines, no helium or metals observed
DB	Only helium He I lines, no hydrogen or metals observed
DC	Continuous spectrum with no lines
DO	Strong ionized helium (He II) lines
DZ	Only metal lines observed
DQ	Strong carbon features
"Hot" DQ	Carbon atmospheres, $T_{\rm eff} = 18000 - 24000$ K,
PG 1159	He II and strongly ionized carbon and oxygen
Dox	Oxygen atmosphere
Suffixes	
Z	Metal lines present
P	Magnetic white dwarfs with detected polarization
H	Magnetic white dwarfs with Zeeman splitting detected
X	Peculiar or unclassifiable spectrum
E	Emission lines present
? or:	Uncertain classification
V	Variable

metal lines are present then a Z is added to the classification. Below 10000 K and 6000 K absorption lines from helium and hydrogen respectively are no longer produced in optical wavelengths, leaving either a pure blackbody spectrum (DC) or a spectrum with metal lines only (DZ). Example DA, DB and D*Z spectra are shown in Figure 1.2.

1.2.2 Cooling timescales

Without core fusion releasing energy, radiation from the photosphere causes the internal energy of the white dwarf to fall and thus cool over time. For a given mass, the white dwarf temperature can therefore be converted into a time since the end of the AGB, referred to as the cooling age or cooling time (Fontaine et al., 2001). Figure (1.3) shows cooling tracks for a selection of typical white dwarf masses and atmospheric types. The cooling roughly follows a power law, with complications induced by the presence (or lack thereof) of convection disrupting heat transfer to the surface, and by the onset of core crystallisation at $T_{\rm eff} \approx 5000$ K releasing more energy.

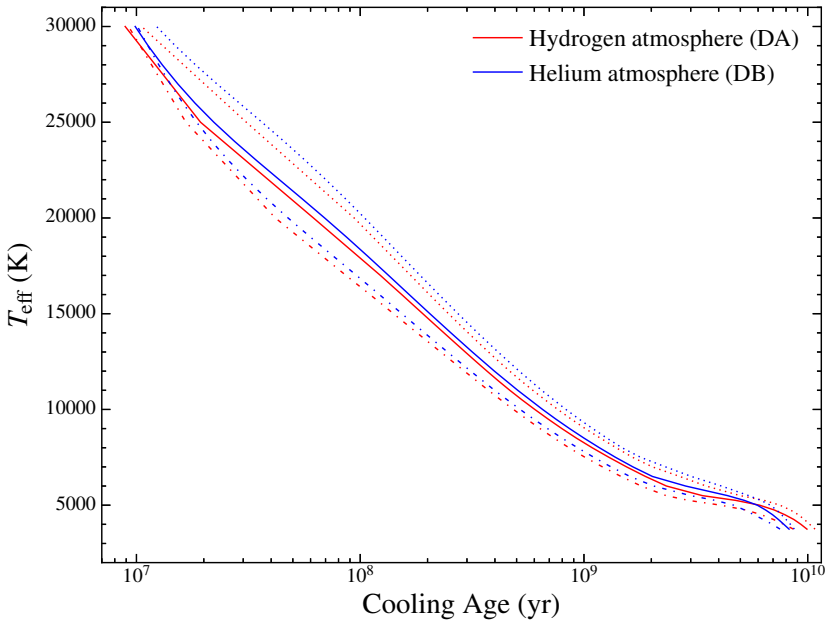

Figure 1.3: Cooling tracks for white dwarf of mass (from top to bottom) $0.7M_{\odot}$, $0.6M_{\odot}$ and $0.8M_{\odot}$ (Holberg & Bergeron, 2006; Kowalski & Saumon, 2006; Tremblay et al., 2011a) .

1.2.3 Mass distribution

The top panel of Figure (1.4) shows the distribution of all masses measured for white dwarfs found in the Montreal White Dwarf Database (MWDD, Dufour et al., 2017)[2] with an average value of $\approx 0.6\,M_{\odot}$. The initial mass of a star from which a given white dwarf formed can be estimated by observations of white dwarfs in clusters, whereby the cooling ages of the white dwarfs are subtracted from the cluster age to give the life time of the progenitor, which is directly related to its mass. Combining these measurements produces the Initial-To-Final Mass Relationship (IFMR), although they combine model-dependent uncertainties in the white dwarf mass, cooling age, cluster age and progenitor mass so have a large scatter. Applying the IFMR of Casewell et al. (2009) to the white dwarf mass distribution, we find an average progenitor mass of $2.2\,M_{\odot}$, equivalent to an A-type star. By comparing with the mass distribution of known planet host stars[3] (Figure 1.4, bottom panel) we arrive at one of the major contributions that white dwarf observations can provide to exoplanetary science: Probing a range of host star masses almost completely unexplored at main sequence systems.

[2] `http://montrealwhitedwarfdatabase.org/`
[3] `http://exoplanets.org/`

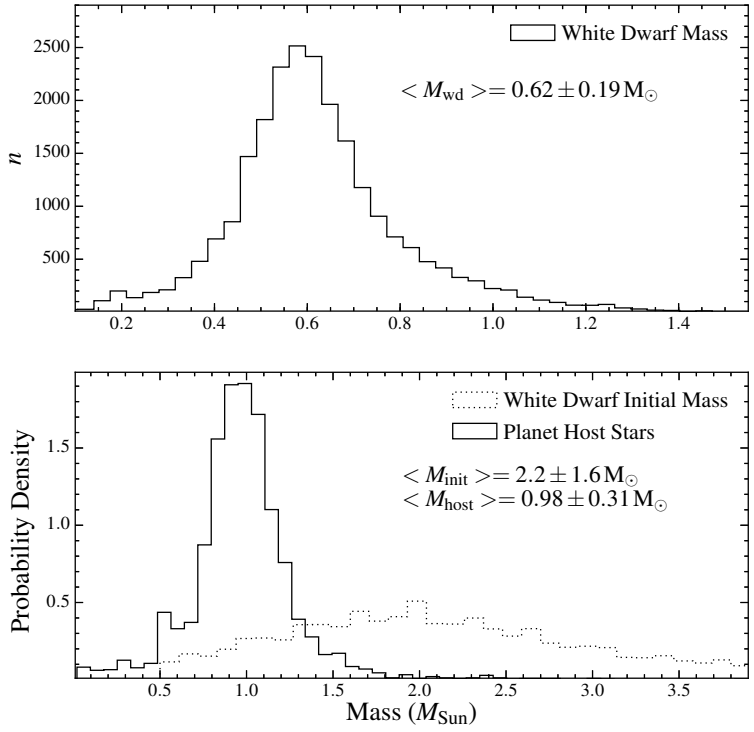

Figure 1.4: Top: Mass distribution of known white dwarfs, retrieved from the Montreal White Dwarf Database (MWDD, Dufour et al., 2017). Bottom: Normalised mass distribution for known exoplanet host stars in the NASA exoplanet archive (Han et al., 2014) compared with the white dwarf progenitor masses.

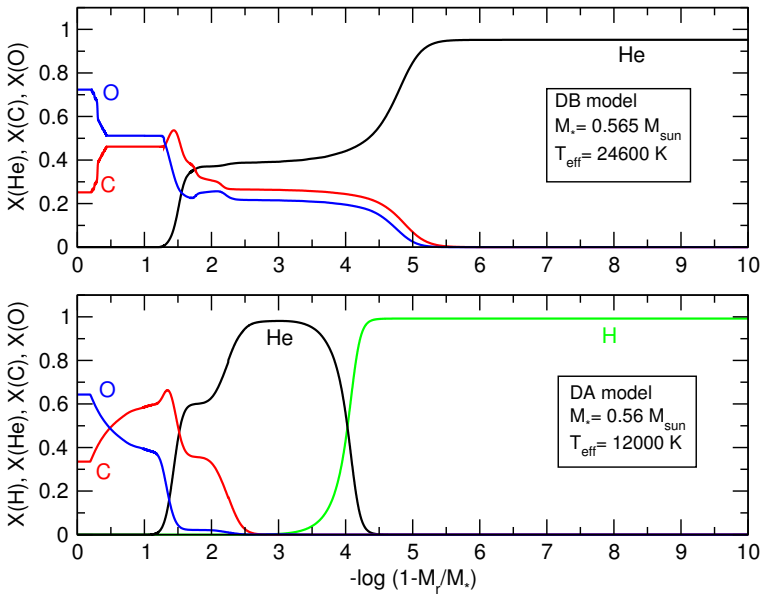

Figure 1.5: Figure 17 from Althaus et al. (2010) showing the interior structure of helium (DB, top) and hydrogen (DA, bottom) atmosphere white dwarfs. The x-axis shows the depth into the white dwarf in terms of enclosed mass, with 0 being the centre, whilst the y-axis shows the mass fraction contributed by each element. The complete lack of mixing in the outermost layers produces pure hydrogen or helium photospheres.

1.2.4 Metal diffusion timescales

The other key feature of white dwarfs with implications for planetary science arises from their high surface gravity ($\log g$), a consequence of their high mass coupled with extremely small ($\approx 1 R_{\oplus}$) radii. The average white dwarf has $\log g \approx 8$ in cgs units, compared with $\log g = 4.44$ and $\log g = 2.99$ for the Sun and Earth respectively. Consequently, white dwarfs are chemical stratified from core to photosphere by atomic weight. Figure 1.5 shows a model for the interior structure of typical white dwarfs from Althaus et al. (2010). Most of the mass is concentrated in a carbon/oxygen core, the product of helium burning in the progenitor giant stages, surrounded by a $\sim 0.01 M_{\odot}$ layer of helium then, in roughly 80 per cent of white dwarfs, a $\sim 10^{-4} M_{\odot}$ hydrogen layer. The outer layers are chemically pure, such that in most cases no traces of the core are observed in white dwarf spectra. Exceptions include the DQ white dwarfs, which have broad carbon absorption features in otherwise helium dominated photospheres, produced by core carbon dredged up by a convective envelope, and Dox white dwarfs with oxygen-dominated atmospheres (Gänsicke et al., 2010; Kepler et al., 2016). Limited core carbon dredge-up is also possibly present in some DB white dwarfs (Chapter 4).

In addition to carbon, oxygen, hydrogen and helium, white dwarfs may initially re-

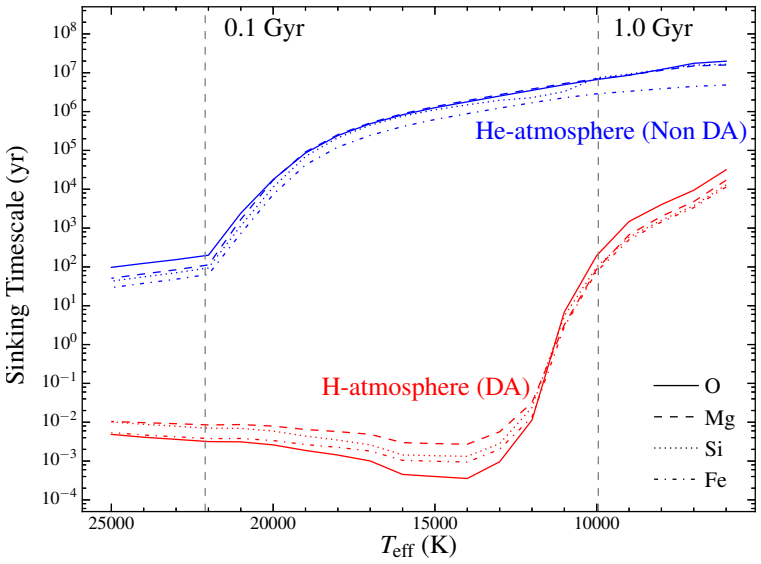

Figure 1.6: Sinking timescales for the four primary chemical constituents of the Earth in hydrogen and helium atmosphere white dwarfs. The horizontal dashed lines show the cooling time at that temperature for a 0.6 $M_{\odot}$ DA white dwarf. Note that 1 day = 2.7×10^{-3} yr. Based on Wyatt et al. (2014), timescales from Koester (2009).

tain other metals in their atmospheres due to radiative levitation, where ions are accelerated by momentum transfer from photons. Whilst this effect is strong at high temperatures, the exact point at which it becomes negligible is unclear. Predictions vary for the effects of radiative levitation between $\approx 30000 - 20000$ K and are dependent on both the metal species and abundance (Chayer & Dupuis, 2010a). Below 20000 K, approximately 0.13 Gyr after the white dwarf formation, radiative levitation is most likely negligible, and the only force acting on photospheric metals is gravity. Figure (1.6) shows the timescales on which metals diffuse out of the visible photosphere of white dwarfs, which are dependent on the atomic mass of the metal as well as the white dwarf $T_{\rm eff}$ and atmospheric structure. For hydrogen atmosphere white dwarfs with $T_{\rm eff} > 13000$ K, the time scales are < 1 yr due to their radiative outer atmospheres. Helium atmosphere white dwarfs and hydrogen atmospheres with $T_{\rm eff} < 13000$ K form convection zones, which suspend the metals and extend the sinking timescales to $\sim 10^2$ yr to $\sim 10^7$ yr, still much shorter than the white dwarf cooling age (Koester, 2009). The key implication of these timescales is that, within $\approx 50 - 100$ Myr of their formation, white dwarfs should have no metals in their photospheres.

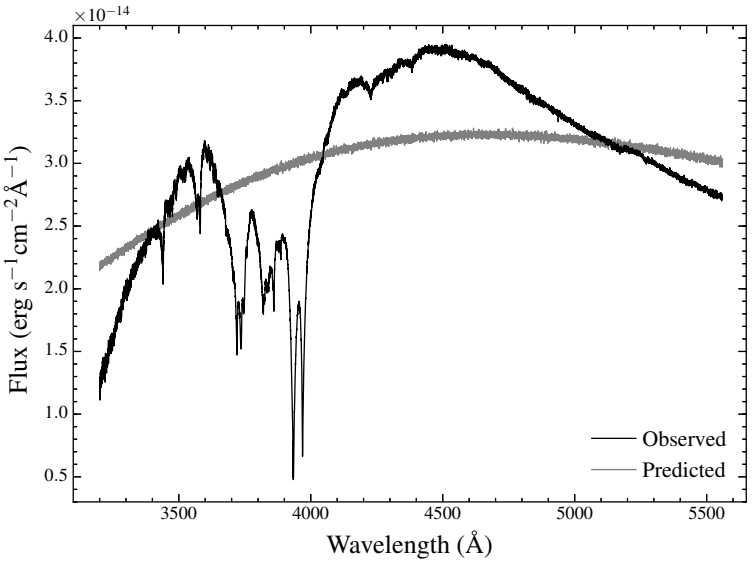

Figure 1.7: Spectrum of van Maannen's star (vMa 2, black) compared with a blackbody curve with the same signal to noise (S/N) and $T_{\rm eff}$ ($\approx$ 6215 K, grey), which is the predicted spectrum of vMa 2 from white dwarf evolutionary models. Every line in the observed spectrum is due to metal pollution. The spectrum was obtained with the X-shooter spectrum, which is described in detail in Chapter 2.

1.3 Remnants of planetary systems

1.3.1 Historical Background

The first observational evidence that planetary systems were extant at white dwarfs was obtained nearly a century ago, although its full implications were not understood for another ninety years (Zuckerman, 2014). van Maanen (1917) reported the discovery of what appeared to be an F star, having no visible spectral features apart from the Ca II H and K lines (Figure 1.7). However, a follow up parallax observation (van Maanen, 1919) showed that it was surprisingly close to the Sun (4.3 parsecs is the modern value) and thus far too faint to be an F-star. It was later identified as a white dwarf, the first isolated example to be discovered[4].

The presence of the calcium lines was unexpected, because with a cooling age of 3.67 Gyr all metals should have long sunk out the photosphere (Fontaine & Michaud, 1979). Further such metal polluted white dwarfs were later discovered, with the leading explana-

[4]The first recorded use of the term "white dwarf" was made by the astronomer Willem Luyten, although it took him two papers to get there: (Luyten, 1922a) refers to them as "white stars" and "dwarf stars" separately, followed eight months later by Luyten (1922b) where he explicitly classifies the object C.P.D. -40 7376 as a white dwarf. Note that the scan supplied by ADS for the second paper is incorrect, but it can be found at the end of Aitken (1922). I am indebted to the anonymous Wikipedia editor who identified the correct location.

tion being that they were accreting metals from the Interstellar Medium (ISM). However the ISM model has a number of flaws, most notably the existence of old DZ white dwarfs that have made several orbits of the Milky Way and accreted none of the hydrogen that dominates the ISM, and of DAZ atmosphere white dwarfs with sinking timescales too short for their metals to have lasted from the last time they left high density regions of the ISM (Farihi et al., 2010).

The first hint of the now-accepted explanation came from infrared observations of the white dwarf G 29-38 by Zuckerman & Becklin (1987), which showed excess flux at wavelengths longer than $\approx 1.5\,\mu$m (Figure 1.8.a). Initially thought to be a brown dwarf companion, Graham et al. (1990) found that the excess was varying in time with the (pulsating) white dwarf, and suggested that it was caused by thermal re-emission from circumstellar dust. Over a decade later, Jura (2003) showed that the infrared excess could be modelled as a disc of dusty debris orbiting the white dwarf, formed by the tidal disruption of an asteroid scattered in from a remnant planetary system (Debes & Sigurdsson, 2002). The dust would be confined between an outer radius at the incoming asteroid's Roche limit and an inner radius where the dust efficiently sublimates into gas. The gas then accretes onto the white dwarf, producing the photosphereic metal lines observed at G 29-38 by Koester et al. (1997). By extension, accretion of disrupted asteroids could be responsible for most or all metal polluted white dwarfs, a hypothesis strengthened by the second detection of an infrared excess consistent with a dusty disc (Kilic et al., 2005; Becklin et al., 2005). More than three dozen white dwarfs with dusty discs are known at the time of writing (Farihi, 2016).

Confirmation of the disc model came a few years later with two results, which form the ground work for the remainder of this thesis. First Gänsicke et al. (2006) detected emission from gaseous calcium at the white dwarf SDSS J1228+1040. The emission shows a distinct double-peaked morphology, the result of Doppler shifts induced by the Keplerian rotation of a disc around the white dwarf (Horne & Marsh, 1986, Figure 1.8.b). The lines therefore provided a measurement of the radial position of the disc, which was found to lie exactly where predicted by the asteroid disruption model, i.e., between the Roche and sublimation radii. Soon afterwards, Zuckerman et al. (2007) obtained high resolution spectroscopy of the white dwarf GD 362, from which the abundances of 15 different metals were measured. The abundance ratios of these metals closely matched those of rocky objects in the Solar system, not only confirming the asteroid accretion scenario but opening the only avenue to directly measure the chemical composition of rocky extrasolar material (Figure 1.8.c).

Thus, 90 years after its original detection, the origin of the metals at van Maannen's star, and indeed all metal polluted white dwarfs was established (Zuckerman, 2014). As

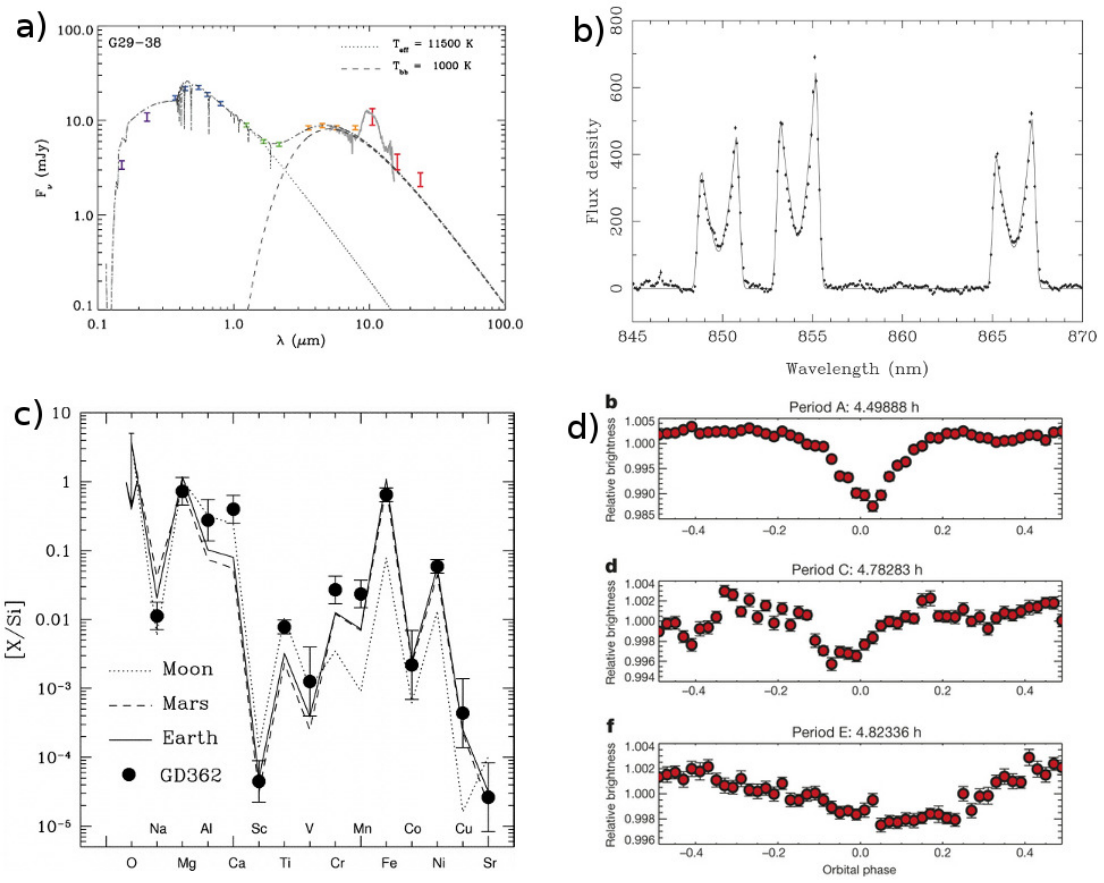

Figure 1.8: Four key observations establishing the existence and observability of remnant planetary systems at white dwarfs. a) The spectral energy distribution (SED) of the white dwarf G 29-38, a combination of the 11500 K white dwarf and a ∼ 1000 K infrared excess from dusty debris (modern data collated by Farihi, 2016). b) Observations of double-peaked gaseous emission at the white dwarf SDSS J1228+1040, showing that the inner and outer radii of the debris disc sit between the sublimation and Roche limits (Gänsicke et al., 2006). c) The chemical composition of the metal pollution in GD 362 compared with Solar system objects, confirming its origin as rocky material (Zuckerman et al., 2007). d) K2 light curves of WD 1145+017 with deep transits from an actively disrupting planetesimal (Vanderburg et al., 2015).

with the Solar system, the expansion and mass loss of the white dwarf progenitors results in the engulfment of their inner planetary systems and the orbital expansion of the outer system. Surviving planetesimals are scattered back inwards towards the white dwarf via chance encounters with larger planets (Debes & Sigurdsson, 2002). As they reach the Roche radius the gravity of the white dwarfs overcome the internal binding of the unfortunate planetesimals and they are tidally disrupted into a stream of debris, before circularising into discs (Veras et al., 2014b). Finally the debris sublimates and accretes onto the white dwarfs, producing the metal absorption lines, eventually sinking out of the white dwarf photospheres.

The only missing evidence was the direct detection of a rocky object at a white dwarf. Eventuality, in 2015 the resurrected *Kepler* spacecraft observed transits from an actively disrupting planetesimal at WD 1145+017 (Vanderburg et al., 2015). Follow up observation have shown that at least six separate pieces of the planetesimal are orbiting the white dwarf at the Roche radius, coupled with an infrared excess and strong metal pollution (Gänsicke et al., 2016; Xu et al., 2016, , Figure 1.8.d).

1.3.2 State of the art

Planetary objects

Despite several searches (Faedi et al., 2011; Belardi et al., 2016), no bona fide planet has yet been detected orbiting a white dwarf. The closest candidate is a directly imaged $7\,M_{Jup}$ object in a 2500 au orbit around the WD 0806-661, but this could be a brown dwarf binary companion (Luhman et al., 2011; Rodriguez et al., 2011). Transiting planets are in principle easy to detect at white dwarfs, as the small radius of the white dwarf results in deep transits for even small planets (Agol, 2011). However, the small white dwarf radii means that the transit probability is low, $\sim$ 1 per cent for close-in planets (which will have been cleared out by engulfment or orbital expansion in the giant phases, although planets may be scattered in later) and decreasing by several orders of magnitude for planets on wider orbits. Thus far, the only transiting planetary object detected is the disrupting planetesimal at WD 1145+017, which a combination of observations and dynamical simulations suggests to be a differentiated object with $\sim 0.1 - 1\,M_{Ceres}$ (Rappaport et al., 2016; Gurri et al., 2017; Veras et al., 2017).

Future projects such as the Large Synoptic Survey Telescope (LSST) and the *PLATO* space mission will have the coverage to detect more transiting objects, both disrupting planetesimals and intact planets, depending on their (currently unconstrained) occurrence rate. Agol (2011) notes that white dwarfs host a habitable zone (approximately defined as the orbital radius where the equilibrium temperature of a planet is such that liquid water could

exist on its surface) at ≈ 0.01 au, with $p_{\rm orb} \approx 0.5$ days. Due to the relatively slow changes in luminosity of white dwarfs with cooling ages $\gtrsim 1.0$ Gyr (Figure 1.3), this habitable zone would endure for many Gyr longer than it took life to arise on Earth. As white dwarfs will outlive most other cosmic objects, if such planets exist they will eventually become the last habitable worlds in the Universe.

Debris discs

Infrared excess consistent with dusty debris disc have been detected at roughly 40 white dwarfs (Rocchetto et al., 2015; Farihi, 2016), mainly via observations with the *Spitzer* and *WISE* space telescopes which observe at longer infrared wavelengths than ground-based facilities. Unbiased surveys with these facilities have yielded occurrence rates for detectable infrared emission at 1–3 per cent, much lower than the corresponding statistic for metal pollution. Suggested reasons for this disparity include the existence of narrow, undetectable discs and direct accretion of planetesimals as gas (Brown et al., 2017; Bonsor et al., 2017). Xu & Jura (2014) discovered the first, and thus far only published, example of a variable infrared excess, charting a 35 per cent flux decrease in under 300 days from the disc at WD J0959-0200. Both the average masses and lifetimes of the discs are currently unconstrained, although observations of DBZ white dwarfs with long sinking timescales, where the mass in the atmosphere is thought to be similar to that in the disc, produce estimates of $\sim 10^{22}$ g and $\sim 10^{6}$ yr respectively (Girven et al., 2012).

A subset of the detected debris discs show emission from a gaseous component, most often detected as double-peaked emission from the Ca II 8600 Å triplet. Emission from O, Mg, Si and Fe has also been observed in some cases (Manser et al., 2016b). The gaseous material is not thought to be a separate structure from the dusty material detected via infrared excess, as they overlap in their radial extent (Brinkworth et al., 2009, 2012; Melis et al., 2010). The temperature beyond the sublimation radius should not be sufficiently high to produce the gaseous material (Hartmann et al., 2011), suggesting that the gas is produced by self interaction between disc particles or via impact from external objects (Jura, 2008). Alternatively the gas is spreading from the sublimation radius via angular momentum exchange, which may induce an eventual runaway evolution of the debris disc (Rafikov, 2011; Metzger et al., 2012).

The gaseous emission at several of the discs shows variability on timescales of order years, implying a dynamic environment. In most cases the overall strength of the lines remains unchanged but the shape of the line profile varies, thought to be caused by general relativistic precession of a fixed structure. The most extensively (and first) observed gaseous disc component orbits the white dwarf SDSS J1228+1040. Manser et al. (2016b) used Doppler tomography to reveal a spiral structure in the disc, which precesses on a

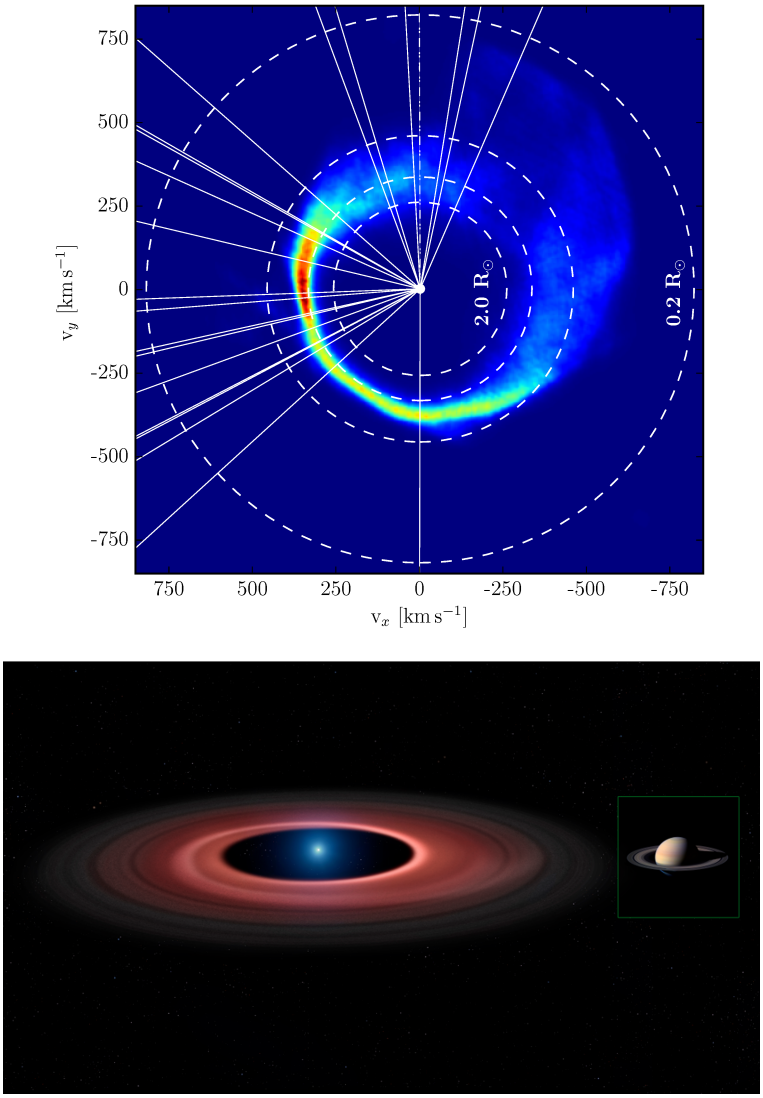

Figure 1.9: Top: Map of the debris disc at SDSS J1228+1040, showing an intensity map in Doppler space inferred from the gaseous emission lines. Bottom: Artists impression of the physical interpretation of the disc as precessing spiral (Manser et al., 2016b, Image Credit: Mark Garlick).

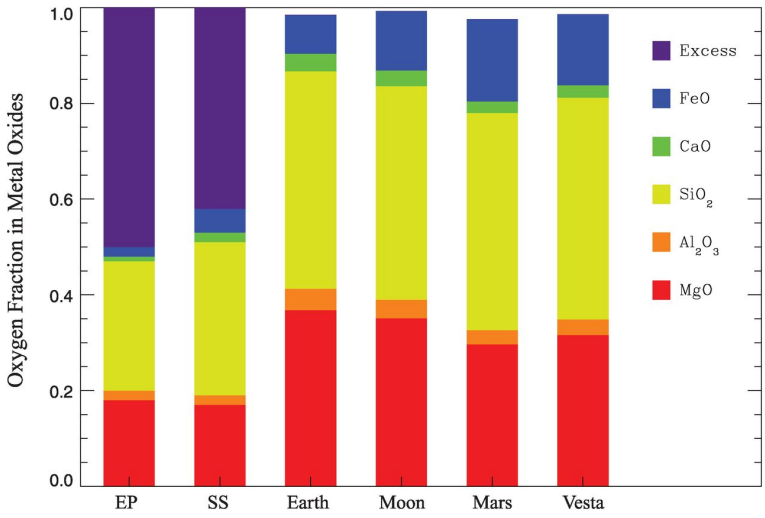

Figure 1.10: Oxygen budget of the debris at GD 61, compared with Solar system objects. The oxygen abundance is too high for it all to have originated in common oxides, suggesting that water makes up a large fraction of the debris. From Farihi et al. (2013a).

$\approx 25 - 30$ yr period (Figure 1.9). Chapter 4 discusses a second example of a gaseous disc component displaying this type of variation. On the other hand, Chapter 3 presents a disc demonstrating a different, and thus far unique form of variation: transient gaseous emission.

Metal pollution

Spectroscopic observations of the metal pollution in white dwarf atmospheres yields two main scientific results. Firstly, the proportion of white dwarfs with metal pollution places a lower limit on the fraction of white dwarfs, and by extension of their A-star progenitors, which host planetary systems. Unbiased surveys of hydrogen- (Koester et al., 2014a) and helium- (Zuckerman et al., 2010) atmosphere white dwarfs found that approximately 25–50 per cent are metal polluted, which agrees to first order with the fraction of main-sequence stars with planets. The true fraction of white dwarfs with planetary systems could of course be higher, as many may not be currently undergoing accretion events.

Over a thousand metal polluted white dwarfs have now been identified (Kleinman et al., 2013; Kepler et al., 2015; Hollands et al., 2017), but in most cases pollution from only one or two metals is detected, usually Ca in optical observations and Si in the ultraviolet. Detection of more metals is hindered by the requirement for high resolution, high signal-to-noise data, which usually demands telescopes of 8 m class or larger as well as, in most cases, ultraviolet spectroscopy with the *Hubble Space Telescope*. The number of white dwarfs for which these observations have been carried out is nevertheless increasing rapidly, as they offer the only technique to directly measure the bulk chemical composition of rocky

extrasolar material, analogous to how the compositions of Solar system bodies are inferred from meteorites (Lodders & Fegley, 2011).

These measurements are necessary for a complete understanding of exoplanetary science, as in most cases the only detectable characteristic of intact planets is their densities, obtained by combining mass and radius measurements from precision radial velocity measurements and transit photometry respectively. Intriguingly, these densities have a wide spread, and do not follow a simple mass-radius relationship (Weiss & Marcy, 2014; Dressing et al., 2015). This may imply that some small exoplanets have compositions distinct from the rocky (and icy) planets and moons of the Solar System, which are all, to first order, a combination of H_2O, $MgSiO_3$ and Fe (Allègre et al., 2001). Modelling exoplanets with a greater variety of bulk chemistries may account for the differences in bulk densities. However, it is impossible to unambiguously infer the internal composition of a planet from its density alone. Seager et al. (2007) and Sohl et al. (2012) computed mass-radius relationships for different planetary compositions, finding a significant degeneracy between different densities, interior structures and compositions. Debris measurements at white dwarfs therefore provide an irreplaceable resource to explore the chemical diversity of rocky exoplanets.

At some white dwarfs pollution by many different metals has been detected, with a record of 16 species recovered in the case of GD 362 (Xu et al., 2013). Over a dozen white dwarfs show pollution from all four of O, Mg, Si and Fe, which make up >90 per cent of the bulk Earth (Gänsicke et al., 2012; Dufour et al., 2012; Klein et al., 2011; Jura et al., 2012; Farihi et al., 2013a; Xu et al., 2014; Raddi et al., 2015). Detailed conclusions can therefore be drawn about the compositions of the disrupted planetesimals. To zeroth order the pollution is similar to rocky objects in the Solar system, dominated by the same four elements with a distinct lack of volatile material (Jura, 2006; Farihi et al., 2009). Within this overall similarity the compositions display the same wide diversity found in the Solar system. Remarkable observations include the detection of oxygen-rich debris at several white dwarfs, suggesting that the debris had a large water/ice fraction (Farihi et al., 2013a; Raddi et al., 2015). In one case the ice was coupled with the first detection of nitrogen, consistent with the accretion of a comet-like Kuiper belt object analogue (Xu et al., 2017). Another interesting aspect of planetary chemistry that can be probed is the survival of iron-rich core material, an example of which is presented in Chapter 4.

With the increasing sample size of detailed composition measurements, it is becoming possible to draw statistical conclusions about rocky exoplanet chemistry and place constraints on the parameter space of extant compositions. I have carried out the first study of this kind, exploring the existence of carbon-rich worlds (Chapter 5).

1.4 Thesis Outline

This thesis proceeds as follows. Chapter 1 provides an introduction to the topic, which I presume you have just read. Chapter 2 discusses the general observational and modelling techniques utilised across the thesis. Chapters 3–6 detail the science results. In Chapter 3 I present the discovery of a white dwarf showing variable gaseous emission from a debris disc. Chapter 4 is a detailed analysis of debris chemistry at a heavily polluted white dwarf. For Chapter 5 I show how general conclusions about planetary composition can be drawn from white dwarf studies. In Chapter 6 I present a suite of observations of the mysterious variable white dwarf GD 394. I end in Chapter 7 with a summary of the thesis and discuss the future of this research area.

Chapter 2

Methods

"The day the world ends, no one will be there, just as no one was there when it began. This is a scandal. Such a scandal for the human race that it is indeed capable collectively, out of spite, of hastening the end of the world by all means just so it can enjoy the show."

Jean Baudrillard, Cool Memories

The work in this thesis relies on two main scientific techniques: Spectroscopic observations of white dwarfs, using both ground-based and space telescopes, and using those spectra to measure the chemistry of planetary debris. Here I describe the basic aspects of these techniques that have general applications to the following science chapters.

2.1 Spectroscopy

The dominant observational technique used in this thesis is spectroscopy, whereby the light from a white dwarf is split by a diffraction grating into its constituent wavelengths and reflected onto a detector. Spectroscopy allows emission and absorption lines from various elements to be resolved, with which we can measure white dwarf atmospheric parameters, metal abundances, and debris disc morphology. There are dozens of professional grade spectrographs, each with their own complementary capabilities. Figure 2.1 shows a schematic diagram of X-shooter, one of the primary instruments utilized in this thesis, which I use here as an example to describe the mechanics of a spectrograph. Key characteristics of further spectrographs used in this work are listed in Table 2.1.

X-shooter is mounted on the Very Large Telescope (VLT) at Cerro Paranal in Chile, an array of four telescopes with 8.2 m primary mirrors referred to as Unit Telescopes (UTs) along with four 1.8 Auxiliary Telescopes (ATs). When combined into the VLT Interferometer they become the most powerful optical telescope in the world, but each UT usually operates independently. X-shooter is mounted on the Cassigrain focus of UT2. Another of the instruments used in this project, the Ultraviolet and Visual Echelle Spectrograph (UVES), is also mounted on UT2 at the Nasmyth focus.

With reference to Figure 2.1, a spectrograph functions as follows. Light from the target is reflected by the telescope through the shutter (top), which can be closed to protect the interior of the spectrograph from stray light when not in use. Below the shutter are the flat field and arc lamps, which can be introduced into the light path for calibration (Section 2.1.1). Movable mirrors can direct some or all of the light to an acquisition and guiding camera, used to first acquire the target and then keep the telescope tracking the target during an exposure. In many spectrographs, including X-shooter, the light is then split into different channels via dichroic filters. In X-shooter the channels cover three fixed wavelength ranges (UVB, covering the wavelength range 3000–5595 Å; VIS, covering the wavelength range 5595–10240 Å; and NIR, covering the wavelength range 10240–24800 Å), but the number of channels, wavelength ranges covered and whether or not those ranges are fixed is different for each spectrograph. Splitting into channels increases spectral resolution (R), as a shorter wavelength range is projected onto each pixel, and allows each detector to be optimised for specific wavelengths.

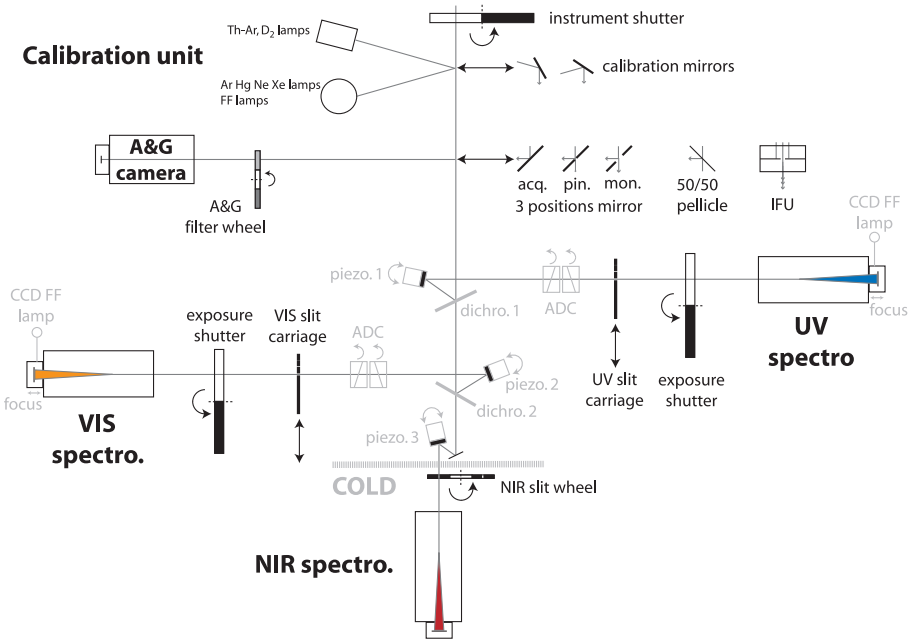

Figure 2.1: Schematic diagram of X-shooter, an echelle spectrograph. The two dichroics split incoming light into three separate paths (UVB, VIS and NIR), allowing it to observe from 3000–25000 Å at medium ($R \sim 4000 - 17000$) resolution simultaneously.

The light then passes through a slit $\approx$ 1 arcsecond wide, which can be adjusted for local sky conditions. Along with the seeing conditions, the slit width determines the intrinsic resolution of the spectrum. After the slit the light encounters a diffraction grating, which splits the light into its component wavelengths and reflects it onto a detector. X-shooter uses an cross-dispersed echelle grating, which projects different orders of a spectrum onto separate parts of the detector. This has the advantage that the entire detector is used, rather than just a single strip, allowing a wider wavelength coverage for a given spectral resolution. However, this complicates the calibration process as each spectral trace must be isolated, separately extracted and combined.

Most ground-based telescopes use charged-coupled devices (CCDs) as detectors. In a CCD, each pixel is a semiconductor capacitor, which when exposed to light gain electron charges in linear proportion to the incident flux. At the end of the exposure a charge is applied that causes each pixel to sequentially shunt its charge to the next pixel. The voltage across the final pixel is then measured, or read out, and the process repeated until a record of the signal at each pixel has been obtained, producing a digital image. The conversion from charge to voltage induces readout noise due to uncertainties in the voltage measurement, which can be ameliorated by making multiple measurements. This increases the total readout time, so a compromise must be made if the observations are time limited. Readout

times on X-shooter range from 100–400 s. Pixels can also be binned together when read out, exchanging resolution for a further decrease in readout noise.

2.1.1 Reduction

In order to turn the digital image of the spectrum into usable data, the spectrum must be calibrated or "reduced", using calibration data obtained along with the spectrum. The precise characteristics of a telescope change on a nightly basis or even during a night, being affected by factors such as temperature and the strains induced on the structure when moved to different positions. Calibration data is therefore usually obtained on the same night as the target observation. The steps taken to reduce a spectrum are as follows:

Bias subtraction

The first stage of calibration is to account for the intrinsic behaviour of the CCD. Each pixel has a "bias" level, an induced voltage offset which ensures that the pixel always returns positive values when read out. The bias varies both by pixel and in time, and is removed from the spectrum by constructing a master bias frame from an average of several zero-second exposures then subtracting it from the science frame.

Flat field subtraction

Each pixel has a slightly different response to incident light. This is accounted for by taking flat frames, which expose the CCD to a uniform brightness white light, usually provided by a lamp inside the spectrograph. As with the bias frames, the flats are combined into a master flat which is then divided out from the spectrum.

Extraction

The 2-d spectrum on the CCD is then extracted into a 1-d spectrum, during which the sky background is also removed. This is achieved by identifying the location of the spectrum on the CCD (or locations, in the case of an echelle spectrograph). A polynomial is fitted to the spectrum, with the pixels in a Gaussian fit to either side extracted and summed using a weighted average. At the same time a sky spectrum is extracted from pixels to either side of the target spectrum and subtracted.

Wavelength calibration

The next step is wavelength calibration, where the each pixel position on the CCD is converted into a wavelength. This is achieved using arc frames, exposures of lamps contain-

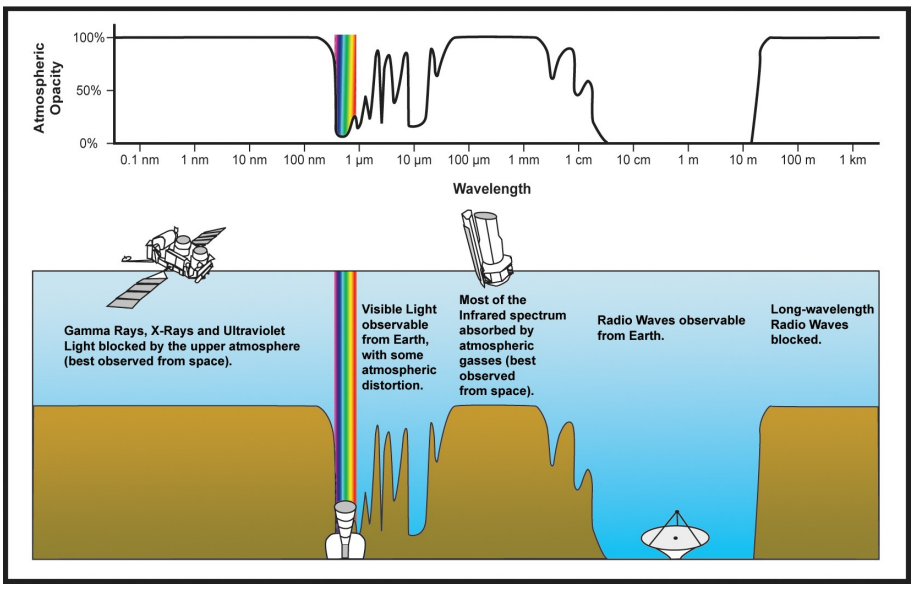

Figure 2.2: Windows of the electromagnetic spectrum visible from the ground. Most wavelengths are absorbed by the Earth's atmosphere and can only be observed from space, including the ultraviolet region critical for studying white dwarfs. Image Credit: NASA.

ing high temperature gases that produce well-characterised emission lines, from which the wavelength at each pixel can be mapped onto the frame. As this step is most sensitive to CCD flexure during a night, arcs should be obtained whenever any major change is made to the set up (e.g. moving the telescope to a new target.)

Flux calibration

The spectrum is then flux calibrated, accounting for wavelength-dependent atmospheric transmittance and detector sensitivity. A well-modelled, bright standard star is observed, usually at the beginning and end of each night, and the ratio between the observed standard and its model spectrum applied to the science spectrum.

Telluric line removal

Finally, the spectrum may have telluric lines removed. These are features produced by atmospheric molecules such as water, and are usually removed by comparison with either model spectra or template telluric spectra. Telluric lines usually only affect short lengths of the spectrum and are difficult to remove precisely, so this step is often skipped if the affected areas are not needed for the intended science goals.

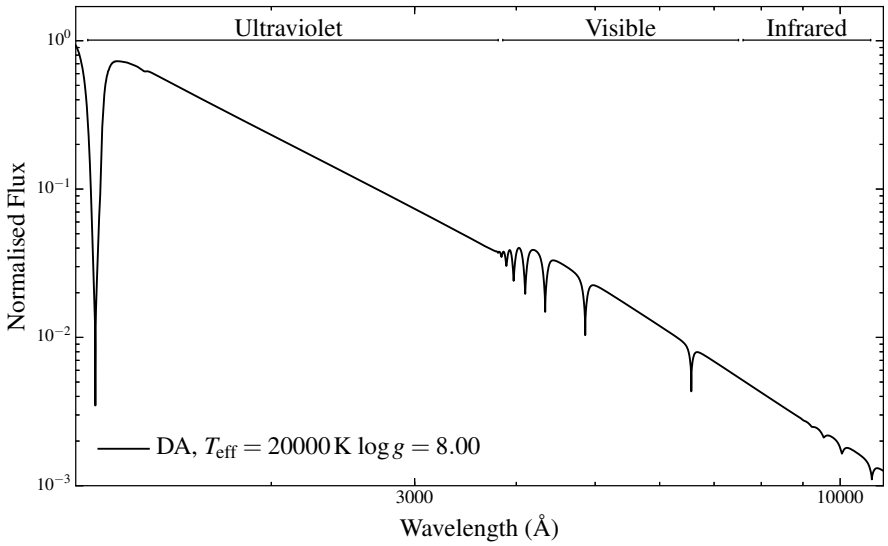

Figure 2.3: Model spectrum of a typical white dwarf (provided by Boris Gänsicke) showing the difference in flux between the visible and ultraviolet wavelength regions.

2.1.2 Space telescopes

Even with the multiple techniques used to extend wavelength coverage employed in X-shooter, ground based telescopes are physically incapable of observing more than a short range of the electromagnetic spectrum. This is due to absorption of the majority of wavelengths by molecules in the Earth's atmosphere, leaving only small windows where light from astronomical objects reaches the ground (Figure 2.2). A number of molecular species are involved, with the dominant species being H_2O at infrared wavelengths and molecular oxygen and ozone in the ultraviolet. Atmospheric absorption places a severe constraint on observations of white dwarfs with $T_{\rm eff} \gtrsim 10000\,{\rm K}$ from the ground, as the ultraviolet flux from a white dwarf can be several orders of magnitude higher than the optical flux (Figure 2.3). Furthermore, the absorption lines of many elements useful for measuring debris composition, such as Si, O, and Fe, are stronger and/or more numerous in the ultraviolet. Fortunately, ultraviolet observations are possible from space using the *Hubble Space Telescope* (*HST*).

Launched in 1990, *HST* is a robotic observatory in a roughly 540 km orbit above the Earth, based around a reflecting telescope with a 2.4 m primary mirror, with four active instruments onboard. Two of those instruments, the Cosmic Origins Spectrograph (COS, Green et al., 2012) and the Space Telescope Imaging Spectrograph (STIS), have provided data for this thesis. Here I look at COS in more detail, focusing on the differences between it and a ground-based spectrograph such as X-shooter.

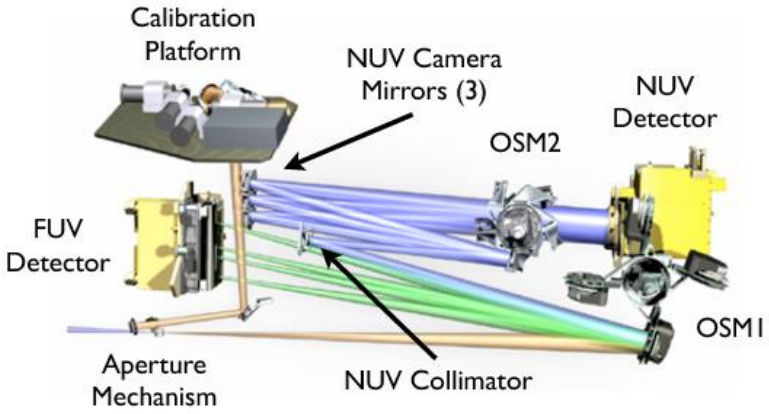

Figure 2.4: Optics of the Cosmic Origins Spectrograph (COS) drawn to scale, taken from the COS Instrument Handbook. Incoming light entering from the left is split into the Far-ultraviolet (FUV, 900–2150 Å, green path) and Near-ultraviolet (NUV, 1650–3200 Å, blue path) channels.

The overall operation of COS (Figure 2.4)[1] is similar to X-shooter, both in producing a spectrum and the steps required for calibration. However, the wavelength range is completely different. COS has two wavelength channels: the Far-ultraviolet (FUV), covering 900–2150 Å; and the Near-ultraviolet (NUV) covering 1650–3200 Å. The diffraction gratings are not fixed, with several gratings available that offer reduced wavelength coverage in return for increased resolution, or vice versa. A further difference between COS and X-shooter is the choice of detector. Instead of a CDD, COS uses photon counters[2], allowing each separate photon that encounters the detector to be recorded in time and position. This allows changes in the target flux to be detected within an exposure, in contrast with a CCD where the flux is time-averaged over the exposure. COS spectra can therefore be used to produce lightcurves of targets with ~ms cadence, a capability demonstrated in Chapter 4. Photon counters are not used on ground-based telescopes as they operate poorly when not in a vacuum and are less efficient at detecting the lower energy photons in the optical range.

[1]The Wikipedia description of Figure 2.4 has autocorrected the "blue ray" of the NUV path to "Blu-ray". As far as I am aware, COS cannot be used to watch films.

[2]Specifically, a cross delay line (XDL) for the FUV channel and a Multi-Anode Micro-channel Array (MAMA) detector on the NUV (the flight spare of the NUV detector on STIS). The precise differences between the two are best left to an engineering thesis.

[3]*FUSE* used an array of four rectangular mirrors.

Table 2.1: List of spectrographs used in this project. The resolution is qualitative as the exact value depends on the grating used. Chapters where data from the spectrographs are used is also given. The entry for the Gemini Multi-Object Spectrographs (GMOS) covers both identical spectrographs mounted on the Gemini North and South telescopes.

Telescope/Instrument	Mirror diameter (m)	λ coverage (Å)	Resolution	Chapter
Ground-based				
SDSS/BOSS	2.5	3600–10400	Low	3, 4
WHT/ISIS	4.2	3000–10000	Medium	3, 4, 6
VLT/X-shooter	8.2	3000–25000	Medium	3, 4
VLT/UVES	8.2	3000–11000	High	3, 4
Keck/HIRES	10	3000–10000	High	6
Gemini/GMOS	8.1	3600–9400	Medium	3, 4
Space-based				
HST/COS	2.4	1150–3200	Medium	4, 5
HST/STIS	2.4	1150–10300	Medium–High	6
FUSE	$4 \times (0.39 \times 0.35)^3$	905–1187	Medium	6

2.2 Measuring metal accretion onto white dwarfs

Once white dwarf spectra have been obtained using the techniques described above, they must be analysed to extract useful information such as the atmospheric parameters and metal abundances. This involves fitting model spectra to the data. The models used here have been developed over many decades by Detlev Koester. Here I summarise the physics behind them, based on Koester (2009, 2010); Koester et al. (2014a). Note that these concern 1-d model atmospheres, which are slowly being superseded by 3-d models (Tremblay et al., 2011b) that more accurately describe convection. However the 3-d models do not yet fully incorporate metal accretion and diffusion, so cannot be used here.

2.2.1 White dwarf model atmospheres

The objective of white dwarf atmospheric models is to take the observed data, usually in the form of spectra, and return atmospheric parameters such as the effective temperature ($T_{\rm eff}$), surface gravity ($\log g$) and metal abundances, accomplished by fitting the appropriate model spectrum to the data. To produce a grid of models for this purpose, the white dwarf atmosphere must be simulated. This is computationally expensive so a number of assumptions are made: Firstly, that the atmosphere is thin relative to the star and is comprised of homogeneous, plane, and parallel layers, where density, pressure and temperature only vary vertically; secondly that the atmosphere is in hydrostatic equilibrium; thirdly that there is no energy generation or loss within the atmosphere itself; and lastly, the atmosphere is in Local Thermal Equilibrium (LTE). Each of these approximations may have domains in

which it does not apply. Most notably the LTE approximation is invalid for white dwarfs with $T_{\rm eff} > 50000\,{\rm K}$, and convective atmospheres obviously vary in more than the radial direction.

With these assumptions in place, the equation of state and absorption coefficients are calculated for each layer, which when combined determine how energy is transmitted through the layers to eventually emerge as a photospheric spectrum. The intensity as a function of wavelength can then be calculated for each layer in a radiative atmosphere. Convection zones cannot be realistically simulated in 1-d, so a mixing-length approximation is used where the energy flux due to convection is incorporated over a certain multiple of the pressure scale height, calibrated using observations of pulsating white dwarfs where the depth of the convection zone can be estimated.

With all of the appropriate physics taken into account, the model produces a spectrum for the surface intensity of the white dwarf over all wavelengths at low resolution. This can then be used to calculate higher resolution spectra over the wavelength coverage of the observations, incorporating the contribution of up to thousands of weak metal absorption lines that would be computationally impractical to include at each stage of the model. For given atmospheric parameters, the strength of each line is proportional to the atmospheric abundance of the element, unless the line saturates at very high abundances. The exact method of retrieving the final abundances varies by user, but usually involves producing a grid of model spectra with different atmospheric parameters and metal abundances and finding which spectrum best fits the data. The abundances are then tweaked until a good fit is achieved.

2.2.2 The accretion-diffusion scenario

Fitting model atmospheres to spectra returns the atmospheric parameters and metal abundances of the white dwarf. However, the metal abundances are not necessarily those of the disrupted planetesimal that the white dwarf is accreting, as each metal diffuses out of the photosphere on a different timescale. The timescales are dependent on the mass and charge of the element and on the depth of the white dwarf envelope, as well as the white dwarf $T_{\rm eff}$ and, in hotter white dwarfs, radiative levitation. The depth at which an atom is no longer in the envelope (i.e., no longer affecting the spectrum) and therefore where the diffusion timescale can be calculated introduces some uncertainty. In convective white dwarfs it is simply the base of the convection zone (Koester, 2009), but there is no clear boundary in a radiative atmosphere, so the convention is to calculate the diffusion timescale at a Rosseland optical depth of 2/3 (Koester et al., 2014a). In hydrogen atmosphere white dwarfs with $T_{\rm eff} \gtrsim 20000\,{\rm K}$, metals may also be suspended by transfer of momentum from photons, known as radiative levitation (Chayer et al., 1994, 1995a; Chayer & Dupuis, 2010b). This

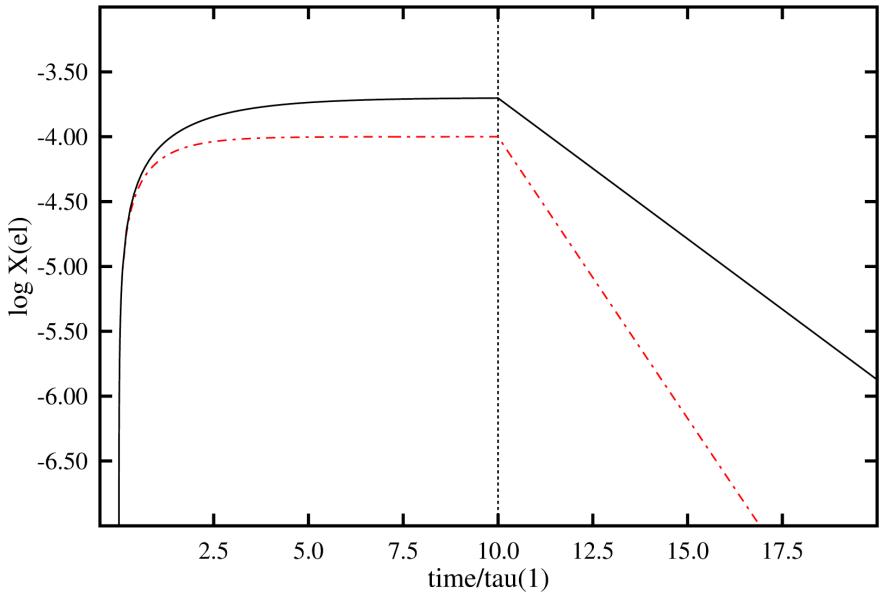

Figure 2.5: Example of the accretion-diffusion model for two elements with different diffusion timescales. The plot shows the atmospheric abundances of each element as a function of time. After the initial switch-on, the metals accreting and diffusing take approximately five diffusion timescales to reach a steady state. After the accretion ends the metals are removed from the atmosphere in a few diffusion timescales. Figure taken from Koester (2009).

has the effect of suspending small amounts ($\log[X/H] \sim -8.00$) of some elements, in particular Si and C, in the photosphere (Koester et al., 2014b). White dwarfs with metal abundances at or below these levels do not require ongoing accretion (Chayer, 2014). Where the metal abundances are too high to be supported by radiative levitation alone (as in all of the objects discussed in this thesis), the levitation is treated as a negative component of the diffusion timescales. Diffusion timescales have been calculated independently by Detlev Koester and by the Montreal white dwarf group, taking into account radative levitation and/or convection where necessary, and show good agreement[4].

To convert the abundances measured in the photosphere into the actual composition of the debris, a steady-state approximation is used where each element undergoes a constant flow through the atmosphere. The accretion rate is then calculated as the mass of each element in the atmosphere divided by the diffusion timescale. Assuming that the accretion rate is constant, the accretion takes roughly five diffusion timescales to reach a steady-state (Figure 2.5). When the accretion event ends the metals take ≈5–10 diffusion timescales

[4]Compare `http://www1.astrophysik.uni-kiel.de/ koester/astrophysics/astrophysics.html` with `http://dev.montrealwhitedwarfdatabase.org/evolution.html`.

to leave the atmosphere. For hydrogen atmosphere white dwarfs with $T_{\rm eff} > 13000\,{\rm K}$, where the diffusion timescales are less than one year, the steady-state assumption is almost certainly valid. A handful of white dwarfs have high-resolution spectra taken a decade or more apart (see for e.g. Chapter 6 and Manser et al., 2016b), none of which show changes in absorption line strength, indicating that the accretion rates are constant over these timescales. The chances of randomly observing a white dwarf with short diffusion timescales in either the build-up or post-event stages is therefore unlikely, so the steady-state approximation is valid and the abundances of the accreting debris can be known with confidence.

However, the picture is less clear for white dwarfs with convection zones, where the diffusion timescales extend from hundreds to millions of years. Given that the orbiting debris discs show variation on a timescale of years (Xu & Jura, 2014) it would be surprising if the accretion rates remained constant for the five diffusion timescales required to reach a steady-state, and at the very longest diffusion timescales the mass that would have sunk into the atmosphere over this time can become unrealistically large. Furthermore, the requirement for the build-up to a steady-state requires the accretion rate to be constant from the start of the event. As the disruption of a planetesimal and circularisation into a disc may take many years (Veras et al., 2014b), the rate is likely to change with the circumstellar environment. Each of these factors combined means that the steady-state assumption does not necessarily apply to white dwarfs with long diffusion timescales. Unfortunately those same objects are often the most useful for measuring planetesimal chemistry, as even trace elements are retained in quantities large enough to be detectable. It has become convention to present multiple models for the debris chemistry at these objects, comparing (for example) the steady-state assumption with the instantaneous atmospheric abundances (Xu et al., 2014), or with the chemistry at several diffusion timescales after accretion switch-off (Raddi et al., 2015). Looking forward, the increasing sample size of observed white dwarfs with short diffusion timescales may allow those with long diffusion timescales to be excluded from general studies of planetary chemistry, whilst advances in theoretical modelling of accretion events may shed light on the appropriate conversion from atmospheric to debris metal abundances.

2.3 Gaseous emission from debris discs

In addition to the detection of absorption lines produced by accreted debris, spectroscopy of white dwarfs can also be used to probe their circumstellar environment. Following on from the detection of gaseous emission from a disc at SDSS J1228+1040 (Chapter 1, Gänsicke et al., 2006), seven more examples have been detected (Gänsicke et al., 2007,

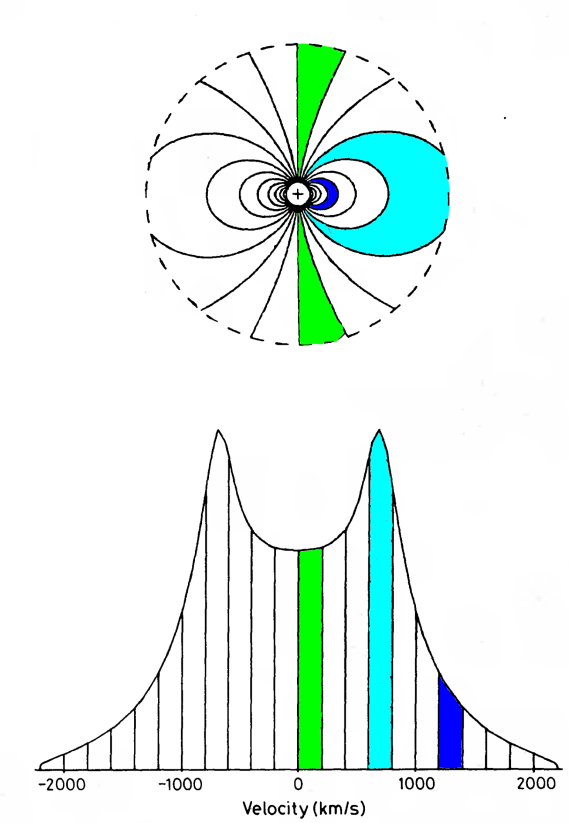

Figure 2.6: Schematic demonstrating the formation of double-peaked emission lines (bottom) from material in a gaseous disc (top). Viewed from below, each part of the disc is moving at a different velocity relative to the observer, producing the colour-coded Doppler-shifted emission. Figure adapted from Horne & Marsh (1986)

2008; Gänsicke, 2011; Dufour et al., 2012; Melis et al., 2012; Farihi et al., 2012; Guo et al., 2015). In each case, the star also has a infrared excess produced by orbiting dusty material, and the gasoeus material likely forms a component of the dust disc, rather than being a seperate structure (Farihi, 2016).

The gas produces distinctive double-peaked emission, as seen in the schematic in Figure 2.6. The emission (bottom) is produced by the Keplarian motion of material in the disc (top). View from the bottom of the figure, the green material is moving laterally to the observer so has little to no Doppler shift, producing emission near the rest wavelength at the centre of the double-peak. Material in the light blue portion near the of the disc is moving slowly, so is only slightly Doppler-shifted, but accounts for most of the emitting surface, forming the peaks. The small amount of material close to the star (dark blue) forms the weak edges of the double-peak, highly shifted from the rest wavelength due to its large orbital velocity. Material on one side of the disc (the right-hand-side in the example) is is moving away from the observer, red-shifting the emission, whilst material on the other side is moving towards the observer and produces the blue-shifted side of the emission feature. The orbital velocities span a few hundred km s^{-1}.

Double-peaked emission therefore not only reveals the presence of a disc but can be used to measure its radial dimensions by converting the Doppler velocities into orbital radii, although the inclination is unknown. The results provide a powerful confirmation that the infrared excesses, and by extension the metal pollution, is produced by tidally disrupted planetesimals. The gaseous components are invariably found to have radial extents bounded by the sublimation radius at the inner edge and the tidal disruption radius at the outer edges. Spatial positions cannot be measured from the infrared excess as fits to the infrared flux are degenerate between factors such as the temperature profile and fine structure (Girven et al., 2012).

2.4 Conclusion

As long as their limitations are known and, if possible, corrected or otherwise accounted for, the combination of spectroscopy and model atmospheres provide a powerful tool to explore remnant planetary systems. The next four chapters present the results of observations of multiple systems exploring a variety of phenomena.

Chapter 3

Variable emission from gas in a debris disc around a metal-polluted white dwarf

"And I beheld when he had opened the sixth seal, and, lo, there was a great earthquake; and the sun became black as sackcloth of hair, and the moon became as blood; and the stars of heaven fell unto the earth, even as a fig tree casteth her untimely figs, when she is shaken of a mighty wind."

Revelation 6:12-13, The Bible, Authorised (King James) Version.

Based on Wilson et al. (2014). Boris Gänsicke contributed to the analysis and provided observational data and Detlev Koester provided the white dwarf model atmospheres. Additional observations were provided and/or carried out by Roberto Raddi, Elmé Breedt, John Southworth and Steven Parsons.

A handful of metal-polluted white dwarfs with dusty debris discs show emission from the 8600Å Ca II triplet, indicative of a gaseous component to the debris disc (Gänsicke et al., 2006, 2007, 2008; Gänsicke, 2011; Dufour et al., 2012; Melis et al., 2012; Farihi et al., 2012; Guo et al., 2015). The double-peaked morphology of the Ca II lines dynamically constrains the gas to be located within the Roche radius of the white dwarf, with the inner disc radii being a few ten white dwarf radii, broadly consistent with the sublimation radius. Time series spectroscopy of several white dwarfs has shown that the emission is variable, but in most cases the line profiles change shape in a regular fashion consistent with a disc undergoing general relativistic precession (Manser et al., 2016b, Chapter 4). Here we report the discovery of a different and thus far unique form of variability: transient Ca II emission from a debris disc around the metal-polluted white dwarf SDSS J161717.04+162022.4.

3.1 Discovery

We applied the procedure outlined in Gänsicke et al. (2008) to search for white dwarfs with Ca II emission in Data Release (DR) 7 of the Sloan Digital Sky Survey (SDSS, Abazajian et al. 2009), and identified two new systems, the He-atmoshere (DB)
SDSS J073842.56+183509.6 (see also Dufour et al. 2012) and the H-atmosphere (DA) SDSS J161717.04+162022.4 (henceforth SDSS J1617+1620, Gänsicke 2011). The SDSS spectrum revealed Mg II 4481 Å absorption in the white dwarf atmosphere, and *Spitzer* observations of SDSS J1617+1620 confirmed the expected presence of circumstellar dust (Brinkworth et al., 2012).

The DR 7 spectrum of SDSS J1617+1620 was obtained on 2008 March 3. Only later, we realised that the star had an earlier DR 6 (Adelman-McCarthy et al., 2008) spectrum, obtained on 2006 July 1, in which the Ca II emission lines are weakly detected, at best. Intrigued by this clear evidence for variability, we initiated spectroscopic monitoring, using the William Herschel Telescope (WHT), Gemini North, and the ESO Very Large Telescope (VLT).

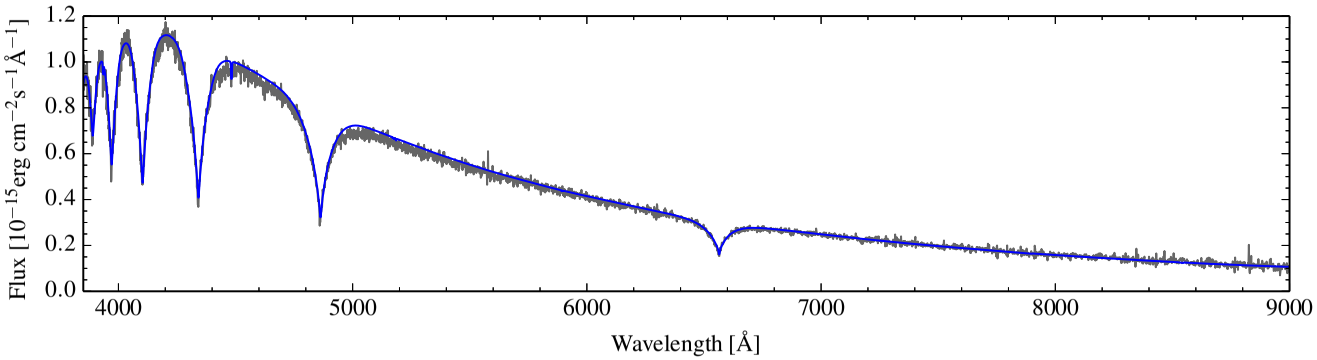

Figure 3.1: Spectrum of SDSS J1617+1620 obtained by SDSS in 2006 (grey). The atmospheric parameters, $T_{\rm eff} = 13520 \pm 200$ K and $\log g = 8.11 \pm 0.08$, were determined by averaging the fits to both SDSS spectra. The corresponding model spectrum is shown in blue. Photospheric absorption of Ca K 3934 Å and Mg II 4481 Å is detected in both SDSS spectra.

3.2 Follow-up observations

The log of the observations is given in Table 3.1. The first follow-up spectra of SDSS J1617+1620 were obtained using the Intermediate dispersion Spectrograph and Imaging System (ISIS) spectrograph mounted on the WHT, with observations carried out on 2009 February 17 and 2010 April 23. On both occasions two 1800s exposures were taken, with a third 540s exposure obtained in 2010. Observations were obtained simultaneously through the blue and red arms of the instrument. The CCDs were binned by factors of 2 (spectral) and 3 (spatial) to limit the impact of readout noise on the observations. The blue arm was equipped with the R600B grating and had a wavelength coverage of 3690–4110 Å at a reciprocal dispersion of 0.45 Å per binned pixel and a resolution of approximately 1 Å. The red arm had the R316R grating in 2009 , covering 5760–8890 Å with a reciprocal dispersion of 1.85 Å per binned pixel and a resolution of approximately 3.5 Å, and the R1200R grating in 2010, with a reciprocal dispersion of 1.52 Å per binned pixel and a resolution of approximately 1.1 Å. The data were reduced and the spectra optimally extracted using the PAMELA[1] code (Marsh, 1989) and the Starlink[2] packages FIGARO and KAPPA. Copper-neon and copper-argon arc lamp exposures were taken before and after the observations and the wavelength calibrations were linearly interpolated from them. We removed the telluric lines and flux-calibrated the target spectra using observations of BD +75 325 in 2007 and SP1036+433 in 2010.

The next observations were obtained on 2010 June 10 at the Gemini North Telescope, where four 900s exposures were obtained in the *i*-band using the R831 grating, with a central wavelength setting of 8600Å. The CCDs were binned by a factor of 2x2 and the wavelength was calibrated using CuAr arcs taken at the end of the night. As with the WHT images, the spectra were again reduced using standard STARLINK procedures, and then optimally extracted using PAMELA. The wavelength calibration was done using MOLLY.

Observations at the VLT with X-shooter (Vernet et al., 2011) in 2011 March–June and the Ultraviolet and Visual Echelle Spectrograph (UVES, Dekker et al. 2000) on 2013 May 05 were reduced using the REFLEX[3] software developed by ESO. After this a heliocentric correction was applied to the REFLEX products. Where multiple observations were made on the same night the spectra were coadded.

A final VLT observations was obtained with the FOcal Reducer and low dispersion Spectrograph (FORS, Appenzeller et al. 1998), taking 3 long-slit spectra with an exposure time of 300 s on 2014 April 30. We covered the near-IR spectral range (7750–9250 Å),

[1] PAMELA and MOLLY were written by T. R. Marsh and can be obtained from `http://www.warwick.ac.uk/go/trmarsh`

[2] The Starlink software and documentation can be obtained from `http://starlink.jach.hawaii.edu/`

[3] The Reflex software and documentation can be obtained from `http://www.eso.org/sci/software/reflex/`

Table 3.1: Log of observations SDSS J1617+1620

Date	Telescope/ Instrument	Wavelength Range (Å)	Spectral Resolution (Å)	Total Exposure Time (s)
2006 July 01	SDSS	3800-9200	0.9	5700
2008 March 03	SDSS	3800-9200	0.9	14700
2009 February 17	WHT	3690-8890	1.6	3600
2010 April 23	WHT	3630-8850	0.5	3600
2010 June 10	Gemini N	7750-8960	0.7	3600
2011 March 21	X-shooter	2990-24790	0.2	6990
2011 May 31	X-shooter	2990-24790	0.2	16380
2011 June 05	X-shooter	2990-24790	0.2	8190
2013 May 05	UVES	3760-9440	0.05	4800
2014 April 30	FORS	7750-9550	0.8	900

using the standard resolution collimator (2×2), the dispersion grism GRIS_1028z+29, and the order separator filter OG590 that give a dispersion of 0.8 Å/pixel, which corresponds to a resolving power R~3800 at 8500 Å. We reduced the data in a standard fashion, using traditional IRAF routines for long-slit spectroscopy, i.e. the 3 spectra were bias subtracted, flat-fielded, wavelength calibrated, sky-subtracted, flux calibrated, and finally combined. The spectrophotometric standard G138-31 was observed soon after SDSS J1617+1620 at similar airmass, although the night was not photometric and only relative flux calibration has been possible.

Comparing the two SDSS spectra (Figure 3.2) shows the dramatic increase in the strength of the Ca II 8600 Å emission line triplet between 2006 and 2008, revealing the formation of a gaseous component in the debris disc around SDSS J1617+1620. The WHT observations, less than a year later, show a significant reduction in the strength of the emission lines, as does the Gemini spectrum. The X-shooter spectra show a further decrease in the strength of the Ca II triplet from the WHT and Gemini data, although the emission lines were still clearly visible on this occasion. However by the time of the UVES observation in 2013 the emission lines appear to have disappeared below the detection threshold. Thanks to the high resolution of the VLT instruments the Ca K 3934 Å and Mg II 4481 Å absorption lines are clearly detected and well defined, allowing for an accurate measurement of the metal abundances in the atmosphere of SDSS J1617+1620.

The FORS spectrum, as with the UVES observations a year before, shows no indication of the Ca II 8600Å emission lines, confirming the disappearance of the gaseous emission.

3.3 White Dwarf Parameters

The atmospheric parameters of SDSS1617+1620 were calculated by fitting model spectra to the SDSS spectroscopy (Figure 3.1) as described by Koester (2010). We report the average parameters obtained from the two SDSS spectra, estimating the uncertainty from the discrepancy between the two fits, as $T_{\rm eff} = 13520 \pm 200$ K and $\log g = 8.11 \pm 0.08$. The corresponding mass, radius, and cooling age, computed from the hydrogen-atmosphere cooling models of Bergeron and collaborators[4], are $M_{\rm wd} = 0.68 \pm 0.05\,{\rm M}_{\odot}$, $R_{\rm wd} = 0.0120 \pm 0.007\,{\rm R}_{\odot}$, and $T_{\rm cool} = 350 \pm 50$ Myr. Using the initial-mass to final-mass relations of Catalán et al. (2008), Kalirai et al. (2008), Williams et al. (2009) and Casewell et al. (2009) suggests a main-sequence progenitor mass of $2.2-3.0\,{\rm M}_{\odot}$, similar to the majority of the metal-polluted white dwarfs (Jura & Xu, 2012; Koester et al., 2014a).

3.4 Variability of the Calcium II Triplet

The dramatic change in the strength of the Ca II emission lines is illustrated in Figure 3.2, where the triplet is clearly seen in the second SDSS spectrum (MJD = 54557), and subsequently fades during our follow-up spectroscopy. To quantify the variable nature of the gas we measured the equivalent widths of the emission lines. As the 8542 Å and 8662 Å components overlap in some of the spectra, we computed the combined equivalent width of the entire triplet, using the wavelength range 8460–8700Å. The resulting values are sensitive to the method used to fit the underlying continuum, leading to systematic uncertainties that dominate the error budget in the case of weak or non-existing line emission. The equivalent widths reported in Table 3.2, and shown in Figure 3.3, confirm the appearance of strong Ca II emission lines in 2008, which subsequently faded by a factor $\simeq 2.5$ within less than a year. The decline in the strengths of the lines then slowed down, and our last spectrum obtained in April 2014 is consistent with the complete disappearance of the lines. Unfortunately, the onset of the Ca II emission is not well-documented. While our analysis formally detects the Ca II triplet in the 2006 spectrum, the corresponding SDSS spectrum is overall of relatively poor quality, and more specifically the wavelength range relevant for the equivalent measurement is affected by residuals from the sky line subtraction. We are therefore unable to unambiguously say whether gaseous emission was present already in 2006, or if it appeared between 2006–2008.

Assuming that the dispersion of the gaseous disc component by 2014 was due to viscous angular momentum exchange suggests a viscous timescale $t_{\nu} \approx 8$ yr. Using equation 2

[4] `http://www.astro.umontreal.ca/ bergeron/CoolingModels`, based on Holberg & Bergeron (2006); Kowalski & Saumon (2006); Tremblay et al. (2011a).

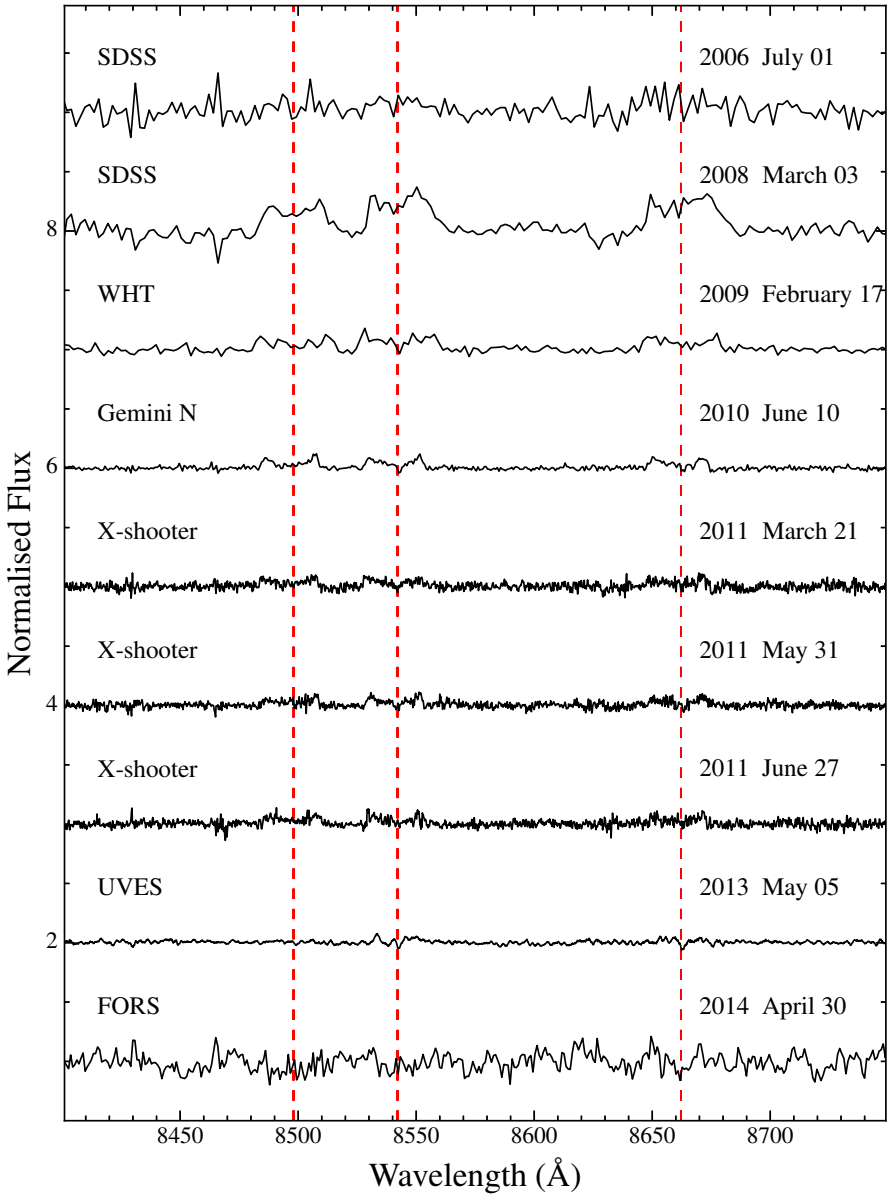

Figure 3.2: Normalised time-series spectroscopy of SDSS J1617+1620 showing the change in strength of the Ca II 8600Å emission line triplet between 2006–2014. The telescope/instrument used to make the observation is indicated on the left above each spectrum, with the date of the observation on the right. The red dashed lines show the rest wavelengths of the Ca II lines. On earlier dates the lines clearly show the double-peaked morphology characteristic of emission from a gaseous disc around the white dwarf (Horne & Marsh, 1986). However by the time that the UVES spectrum was obtained in March 2013 the lines, and hence the gaseous component of the debris disc, had disappeared (Figure 3.3).

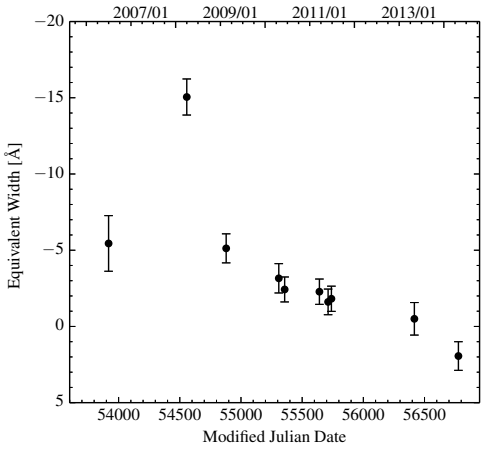

Figure 3.3: Change in the strength of the Ca II triplet seen in the spectra of SDSS J1617+1620 over the period 2006–2014 (Figure 3.2). The equivalent widths of the emission lines in each spectrum were calculated over the wavelength range 8460–8700Å. The strength of the emission line increases by a factor~3 between the first and second observations, before dropping down to zero by 2013. This represents a dramatic increase then loss of emission from gaseous debris in a disc around SDSS J1617+1620.

of Metzger et al. (2012) yields a viscosity parameter α ~0.25, within the range estimated by King et al. (2007) for an ionised thin disc.

The Ca II lines show a mildly double-peaked morphology (Figure 3.2), which arises from the Doppler shifts induced by the Keplerian velocity of the material in the disc (Horne & Marsh, 1986, Chapter 2). The total width and peak separation of the Ca II lines can be used to estimate the inner and outer radii of the disc respectively, and we find $R_{\rm in} \sin^2 i \approx 0.5\,{\rm R}_\odot$ and $R_{\rm out} \sin^2 i \approx 1.2\,{\rm R}_\odot$, where i is the unknown inclination of the disc. These values are similar to the inner and outer radius estimated for SDSS J122859.93+104032.9 and SDSS J084539.17+225728.0 (Gänsicke et al., 2006, 2008), i.e. the outer radius is compatible with the tidal disruption radius of a rocky asteroid (Davidsson, 1999), and the inner radius is near the sublimation radius (von Hippel et al., 2007). Note that, whilst the inner radius can be constrained by calculating the Doppler shift at the Full Width-Zero Intensity of the emission lines, the point which represents the outer edge is somewhat more arbitrary. In this case we chose to measure the peak separation of the lines to provide a lower limit.

Inspecting our WHT, Gemini, and VLT/X-shooter spectra, there is a slight hint that the width of the Ca II lines decreases with time, which would imply the inner radius of the gas disc moving further out. However the emission lines in the later observations are too weak to make a firm conclusion.

Table 3.2: Equivalent widths of the absorption and emission lines in the times-series spectra of SDSS J1617+1620. Note the relatve consistency of the Ca K 3934 Å and Mg II 4481 Å absorption lines compared to the hugely variable Ca II 8600Å triplet. No measurement was made of the absorption lines in four cases: The SDSS spectra are of insufficient quality for an accurate measurement, and the Gemini and FORS observations did not cover the corresponding wavelength range.

	Equivalent Width [Å]		
Date	Ca II 3934 Å	Mg II 4481 Å	Ca II 8600 Å Triplet
2006 July 01	-	-	-6.4±1.8
2008 March 03	-	-	-16.1±1.2
2009 February 17	0.20±0.02	0.34±0.02	-6.1±1.0
2010 April 23	0.16±0.03	0.36±0.05	-4.2±1.0
2010 June 10	-	-	-3.4±0.8
2011 March 21	0.21±0.01	0.30±0.02	-3.3±0.8
2011 May 31	0.20±0.01	0.28±0.01	2.-6±0.8
2011 June 27	0.20±0.01	0.26±0.01	-2.8±0.8
2013 May 05	0.23±0.01	0.26±0.01	-1.5±1.1
2014 April 30	-	-	0.9±0.9

3.5 Accretion of Planetary Material

In addition to the Ca II 8600 Å emission line triplet we detect photospheric absorption Ca K 3934 Å and Mg II 4481 Å lines (Figure 3.4). The detection of metal pollution provides an opportunity to investigate the chemical diversity of extrasolar planetary systems (e.g. Zuckerman et al., 2007; Klein et al., 2011; Gänsicke et al., 2012; Xu et al., 2014). The relevant procedures and detailed physics have been extensively described by Gänsicke et al. (2012) and Koester et al. (2014a), as well as in Chapter 2 and we provide here only a brief summary.

A key assumption in the interpretation of the photospheric metal abundances is a steady state between accretion and diffusion (Koester, 2009), in which case the diffusion flux is constant throughout the atmosphere, and equal to the accretion rate from the debris disc. The relativity low effective temperature of SDSS J1617+1620 implies that the diffusion of metals within the atmosphere should not be affected by radiative levitation (Chayer et al., 1995a). While the temperature is sufficiently high that no deep convection zone develops, some convection zones are present at Rosseland optical depths $0.04 \lesssim \tau_{\rm R} \lesssim 3.2$ and $300 \lesssim \tau_{\rm R} \lesssim 1936$. In between these zones the atmosphere is radiative. Regardless of the details of the atmospheric structure, the diffusion timescales are very short ($\tau_{\rm diff} \approx 0.5$ yr, Table 3.3), meaning that SDSS J1617+1620 must be currently accreting from an external source, almost certainly the circumstellar gas and dust. We have computed the correspond-

ing diffusion fluxes under two assumptions: 1. Treating the entire atmosphere as convective and 2. Evaluating the diffusion time scales at $\tau_R = 3.2$, the bottom of the shallow convection zone near the surface.

Table 3.3 reports the average accretion fluxes of Mg and Ca, and an upper limit for Si, obtained from the analysis our WHT, X-Shooter and UVES spectra (the quality of the SDSS spectra is too low, and the Gemini and FORS spectra do not cover the relevant wavelength range). Scaling for the relative abundance of Mg and Ca in the bulk Earth (Allègre et al., 2001), we estimate a total metal accretion flux onto the white dwarf of $\approx (6.4 \pm 1.8\text{–}7.8 \pm 3.3) \times 10^8\,\mathrm{g\,s^{-1}}$, consistent with the accretion rates measured in other dusty DA white dwarfs (Vennes et al., 2010, 2011; Melis et al., 2011; Gänsicke et al., 2012).

We find that the planetary debris around SDSS J1617+1620 has log[Ca/Mg] = −1.4 to −1.6, (by number, depending on the treatment of convection), which is somewhat low compared to the values found for the the bulk Earth (−1.17, McDonough 2000) C I chondrites (−1.24, Lodders 2003), and the Sun (−1.24, Lodders 2003). A depletion relative to other elements is also seen in GALEX J193156.8+011745 (Vennes et al., 2010, 2011; Melis et al., 2011; Gänsicke et al., 2012), and was interpreted by Melis et al. (2011) as potential evidence for the accretion of a differentiated body that had its crust and part of its mantle stripped. Conclusions regarding the nature and origin of the debris around SDSS J1617+1620 remain limited as only two photospheric elements are so far detected. Progress will require deep optical and ultraviolet spectra probing for the abundances of C, O, Si, Al, Ti, and Fe.

A final note concerns the temporal evolution of the photospheric absorption lines of Mg and Ca. While the equivalent widths of the Ca K line are constant within the uncertainties (Table 3.2), the Mg II 4481 Å lines shows a notionally significant change, being strongest in the first WHT observation during the early decline of the Ca II emission lines. Rafikov (2011) and Metzger et al. (2012) showed that the generation of gas can lead to a significant increase in the accretion rate onto the white dwarf. While the observations do not exclude small changes in the accretion of Mg (which, if real, would imply a chemical differentiation within the debris), they rule out a large variation of the total accretion rate.

3.6 Discussion

The formation mechanism of gaseous components to debris discs around metal-polluted white dwarfs is uncertain. Gaseous emission is only observed around a small fraction of the metal-polluted white dwarfs, and in all cases where Ca II emission lines are observed circumstellar dust is also detected in the form of a noticeable infrared excess (Brinkworth et al., 2009; Melis et al., 2010, 2012; Brinkworth et al., 2012; Farihi et al., 2012). However,

Table 3.3: Diffusion timescales and average accretion fluxes, computed under the assumption of a fully convective atmosphere or using the diffusion time scales at the bottom of the shallow convection zone near the surface.

Element	fully convective		convective at $\tau_R = 3.2$	
	$\log \tau_{\rm diff}$ (yrs)	$\dot{m}$ (g s^{-1})	$\log \tau_{\rm diff}$ (yrs)	$\dot{m}$ (g s^{-1})
12 Mg	−0.46	1.7×10^8	−2.2	7.3×10^7
14 Si	−0.36	$\leq 2.5 \times 10^8$	−2.5	$\leq 2.9 \times 10^8$
20 Ca	−0.37	7.2×10^6	−2.3	5.0×10^6

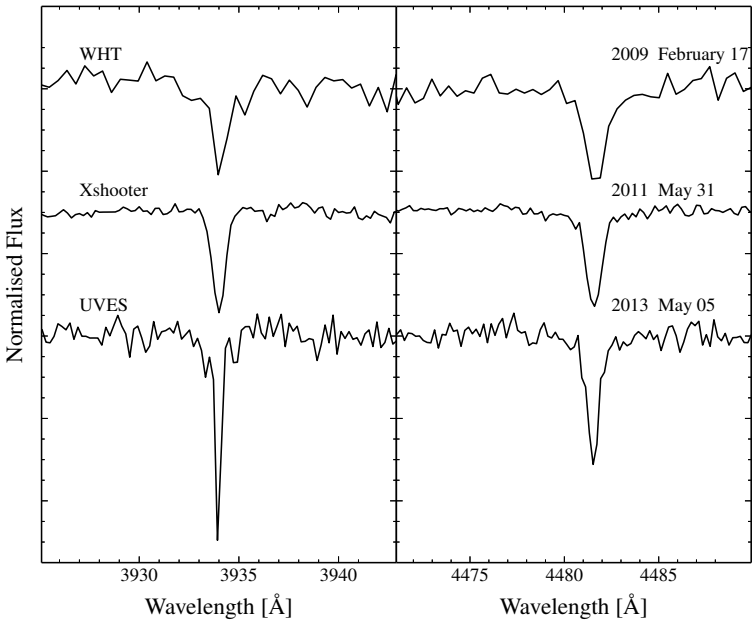

Figure 3.4: Photospheric absorption lines of Ca K 3934 Å (left) and Mg II 4481 Å (right), illustrating the different spectral resolutions of the instruments used for the follow-up spectroscopy. The equivalent widths measured from all our spectra are given in Table 3.2 and average accretion fluxes are given in Table 3.3. The apparent greater depth of the UVES observation of the Ca K line is an effect of the higher spectral resolution and does not represent an increase in equivalent width.

many dusty and strongly metal-polluted white dwarfs do not show any emission lines from circumstellar gas (e.g. Gänsicke et al., 2007; Vennes et al., 2010; Klein et al., 2011; Farihi et al., 2012), so their formation cannot be universal. Gas is found around white dwarfs with temperatures ranging from $\simeq$ 13 000 K to $\simeq$ 22 000 K (Gänsicke et al., 2006, 2007, 2008; Farihi et al., 2012; Melis et al., 2012; Dufour et al., 2012), similar to the range where dusty discs are found (Farihi et al., 2009).

The Ca II emission lines can be modelled by optically thin H and He-deficient gas with a temperature near 6000 K, but the heating mechanism is unclear: Hartmann et al. (2011) assume an active disc, i.e. heated by the inwards flow of material, but require an unrealistically high accretion rate of 10^{17-18} g s^{-1}, which is many orders of magnitude higher than the accretion rates onto the white dwarf derived from the photospheric abundances. Kinnear (2011) and Melis et al. (2010) showed that irradiation from the white dwarf is sufficient to keep circumstellar metal gas at many 1000 K, and that cooling occurs primarily through optically thick lines. Kinnear (2011) could quantitatively reproduce the observed line fluxes with a photoionisation model.

The high temperature necessary to explain the Ca II emission lines, together with the radial extent of the gaseous disc component ($\sim 0.5 - 1.5\,R_\odot$) and the absence of gas at many dusty white dwarfs rules out production of the gas by sublimation of the dust within the radiation field of the white dwarf. In fact Gänsicke et al. (2006, 2007) and Brinkworth et al. (2012) showed that the location of the inner edges of the gaseous debris derived from observations are broadly consistent with the sublimation radius, i.e. the radial distribution of gas and dust largely overlap.

We speculate on two possible explanations for the transient formation of the gaseous emission. One scenario is the impact of a small asteroid onto a more massive, pre-existing debris disc (Jura, 2008). The rocky nature of this body is implied by the absence of Balmer emission lines from the disc. Entering the tidal disruption radius, the incoming asteroid will start to break up, and vaporise upon the high-velocity impact onto the disc. The gas generated in that way will subsequently spread radially due to viscous angular momentum exchange, and heating by the white dwarf will result in the observed Ca II emission. The gas will eventually accrete onto the white dwarf (with a small amount moving outwards to carry away angular momentum), and the decreasing density will result in a weakening of the emission lines. In summary, such a "secondary impact" event would be produce a single event of transient Ca II emission.

A slight twist to the above scenario is that the dust disc at SDSS J1617+1620 is young, and we have witnessed the impact of material in a debris tail left-over from the original disruption. The detailed evolution of the tidal disruption of asteroids has not yet been fully explored. Debes et al. (2012) simulated the disruption of a rubble pile asteroid, and

found that an elongated debris train is formed. Veras et al. (2014b) followed the evolution of disrupted rubble piles over many orbital cycles, and demonstrated that, in the absence of additional forces beyond gravity, a highly collisionless eccentric ring of debris is formed. Additional forces, e.g. from sublimation or tidal interactions, are probably required to fan out the debris train, eventually circularising material in a close-in circumstellar disc. This process is likely to extend over many orbital cycles, which, as the original semi-major axis of the asteroid should have been $> 1 - 2$ au (i.e. beyond the region cleared out as the white dwarf progenitor moved along the giant branches), could imply timescales of many tens to even thousands of years. During that period, repeated impacts of leftover debris are expected, and one would expect another flare-up of gas emission from SDSS J1617+1620 over the next years to decade.

The serendipitous discovery of the transient Ca II emission in SDSS J1617+1620 is a strong motivation for a more systematic monitoring of large numbers of white dwarfs to detect tidal disruption events of planetary bodies. The spectroscopic observations that led to the discovery of the gas disc in SDSS J1617+1620 are moderately expensive in terms of telescope time and aperture. The observed changes in the Ca II line fluxes correspond to a 2% variability of SDSS J1617+1620 in the *i*-band. Such events are hence close to the detection threshold of current ground-based transient surveys (Ivezić et al., 2007; Ofek et al., 2012), but should be easily detected in the era of Gaia and LSST (Carrasco et al., 2014; LSST Science Collaboration et al., 2009).

3.7 Conclusion

We have observed unambiguous evidence for a variable gaseous component of the debris disc around the white dwarf SDSS J1617+1620, demonstrating that observations of dusty and gaseous discs around metal-polluted white dwarfs can provide further insight into the dynamics of such systems. This will also allow us explore the nature and composition of the accreted material in greater detail and better understand the post-main sequence evolution of extrasolar planetary systems. Continued observations of SDSS J1617+1620 and other white dwarfs with gaseous discs will be required to further investigate the highly dynamical nature of evolved planetary systems.

Chapter 4

The chemical composition of a disrupted extrasolar planetesimal

"It's the end of the world as we know it (and I feel fine)"

R.E.M., Document

Based on Wilson et al. (2015). Boris Gänsicke contributed to the analysis and provided observational data, Detlev Koester provided the white dwarf model atmospheres and Odette Toloza extracted the time-tag lightcurve. Additional observations were provided and/or carried out by Anna Pala, Elmé Breedt and Steven Parsons.

In most metal polluted white dwarfs only one or two elements, usually Ca and/or Mg, has been detected. However high–resolution spectroscopy of an increasing number of systems has revealed pollution by large numbers of metals, with a record of 16 species detected in the case of GD 362 (Xu et al., 2013). Around a dozen white dwarfs show photospheric O, Mg, Si and Fe (Gänsicke et al., 2012; Dufour et al., 2012; Klein et al., 2011; Jura et al., 2012; Farihi et al., 2013a; Xu et al., 2014; Raddi et al., 2015). These four elements make up >90% of the bulk Earth (Allègre et al., 2001).

Consequently these systems provide a unique opportunity to study the bulk chemical composition of extrasolar planetary systems. Thus far, two main conclusions have been reached: 1. To zeroth order the chemical composition of the accreted debris is similar to that of the terrestrial planets in the Solar System (Zuckerman et al., 2007; Jura & Young, 2014), with a distinct lack of volatile elements (Jura, 2006; Farihi et al., 2009); 2. Within this overall similarity there is a large amount of diversity, with some systems showing evidence of differentiation (Gänsicke et al., 2012), post-nebula processing (Xu et al., 2013) and water-rich asteroids (Farihi et al., 2013a; Raddi et al., 2015).

We present ultraviolet and times-series optical spectra of the metal-polluted helium atmosphere (DB) white dwarf SDSS J084539.17+225728.0 (henceforth SDSS J0845+2257). This object was originally classified as a sdO subdwarf, Ton 345 (Green et al., 1986). As part of a search for Ca II 8600 Å emission lines among white dwarfs with SDSS spectra, Gänsicke et al. (2008) found that SDSS J0845+2257 was in fact a DB white dwarf with a gaseous disc. Follow-up observations obtained with the William Hershel Telescope (WHT) revealed a significant change in the shape and strength of the Ca II 8600 Å emission line profile, along with strong photospheric absorption lines from Ca, Si and Mg.

Jura et al. (2015) presented a Keck/HIRES study detecting 11 metals in the atmosphere of SDSS J0845+2257. We extend these observations into the ultraviolet and carry out an independent detailed study of the accreted material. We also present updated time-series observations of variable emission from the gaseous disc around SDSS J0845+2257 and an analysis of the *HST*/COS high-speed ultraviolet photometry.

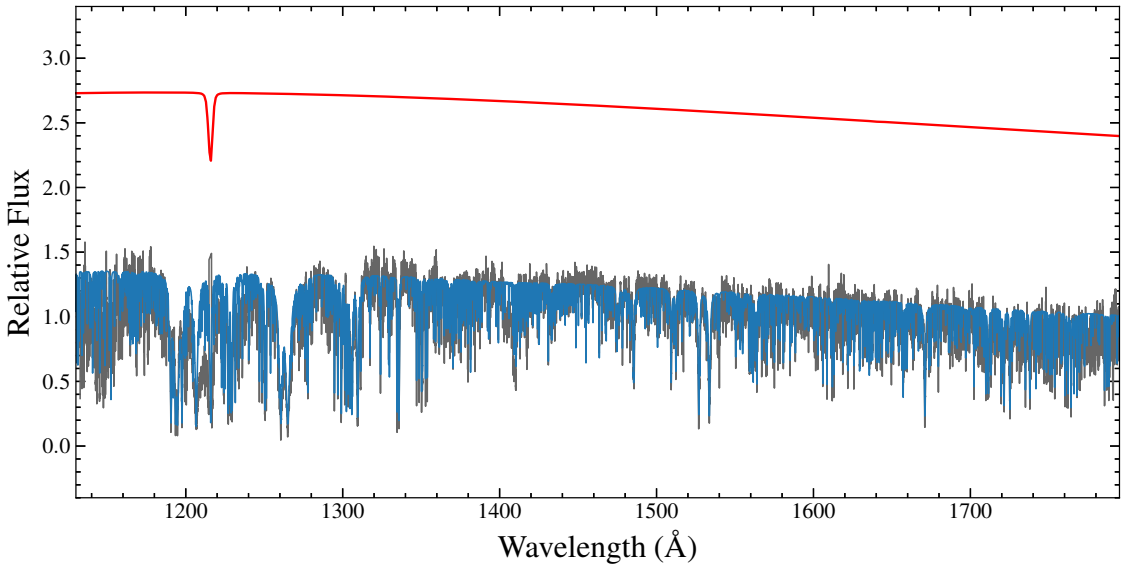

Figure 4.1: *HST*/COS FUV spectrum of SDSS J0845+2257 obtained on 2010 April 01 (grey), with the model fit used to determine the abundances of the accreted metals (blue). Plotted in red is a model spectrum for a white dwarf with the same atmospheric parameters, but no metals. The extremely large number of metal absorption lines in the spectrum of SDSS J0845+2257 is successfully reproduced by the model fit, with the exception of the two sections shown in Figure 4.4.

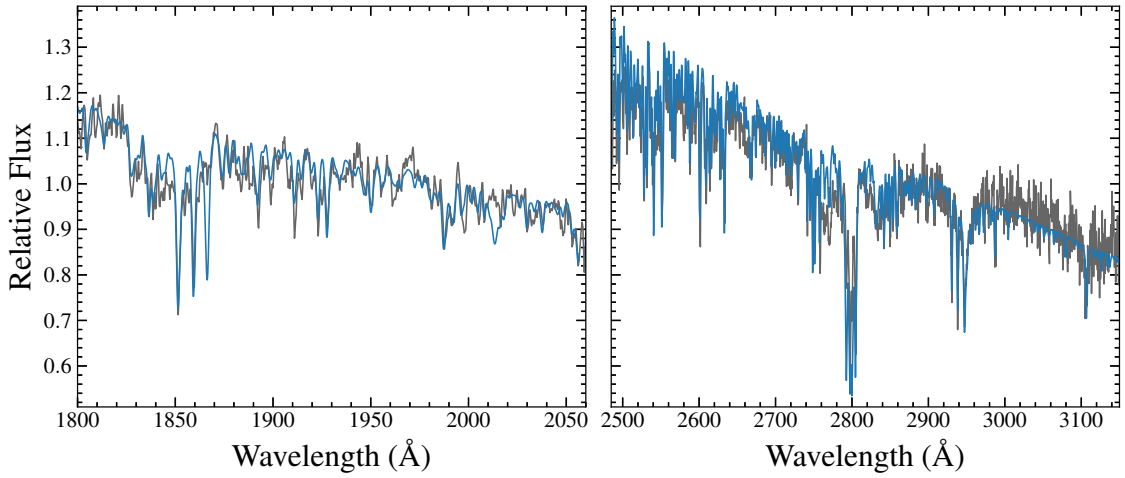

Figure 4.2: *HST*/COS NUV spectrum of SDSS J0845+2257 obtained on 2010 March 31 (grey), with the model fit used to determine the abundances of the accreted metals (blue). The model under-predicts the Mg II 2790Å triplet, possibly due to emission from the gaseous debris disc (Section 4.4).

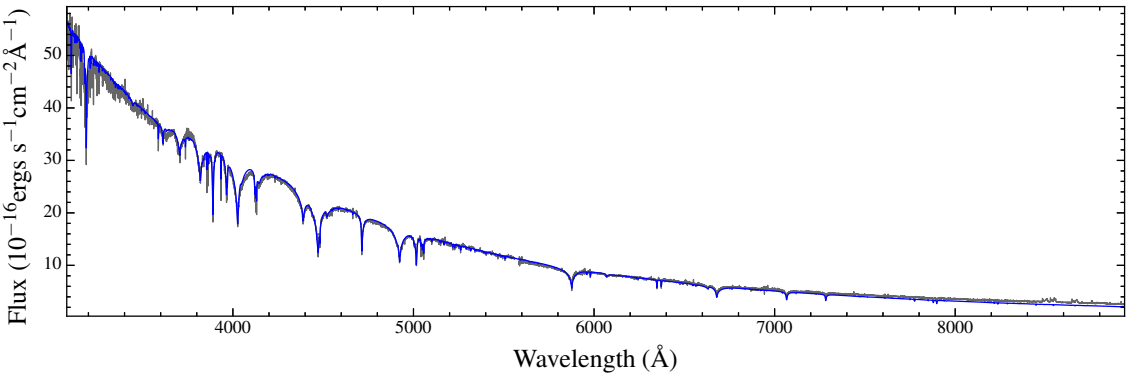

Figure 4.3: Full optical spectrum of SDSS J0845+2257 from the UVB and VIS arms of X-shooter (grey) together with the model fit (blue) used to calculate the atmospheric parameters and the metal abundances. A telluric correction was applied using the X-shooter spectral library (Chen et al., 2014). The model is over-plotted using just one scaling factor for the entire spectrum, demonstrating the excellent flux calibration of the X-shooter data.

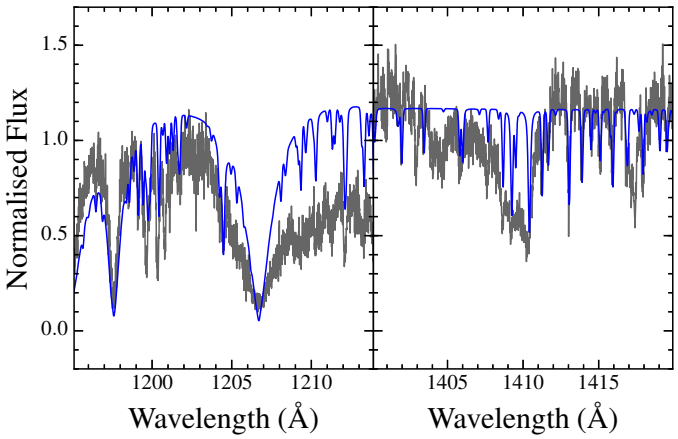

Figure 4.4: The model fit to the FUV spectrum under-predicts the red wing of the 1206 Å Si III resonance line and what appear to be Si lines around 1400 Å. The reason for the poor fit in these areas is unknown, but a similar feature is seen in GALEX 1931+0117 (see fig. 4 in Gänsicke et al., 2012). One possible cause is absorption from circumstellar gas, similar to that unambiguously detected at WD 1145+017 (Xu et al., 2016).

Table 4.1: Log of observations of SDSS J0845+2257.

Date	Telescope/ Instrument	Wavelength Range (Å)	Spectral Resolution (Å)	Total Exposure Time (s)
2004 December 19	SDSS	3794–9199	0.9–2.1	3300
2008 January 02	WHT/ISIS	3577–8840	1.0–2.0	2400
2008 Apri1 03–5	VLT/UVES	3280–9460	0.02	17820
2009 January 08	VLT/UVES	3280–9460	0.02	11880
2009 April 09–11	VLT/UVES	3280–9460	0.02	17820
2010 March 31	*HST*/COS	2470–3150	0.01	7727
2010 April 01	*HST*/COS	1600–3150	0.39	14397
2010 April 02	Gemini South/GMOS	7540–9665	2.0	4980
2011 January 29	VLT/X-shooter	2990–24790	0.2–0.6	6990
2014 October 20	VLT/X-shooter	2990–24790	0.2–0.6	3731

4.1 Observations

Since the publication of Gänsicke et al. (2008) we have obtained deep spectroscopic observations of SDSS J0845+2257 in the ultraviolet with the *Hubble Space Telescope* (*HST*) and in the optical with the ESO Very Large Telescope (VLT) and Gemini South. Table 4.1 provides a log of our observations.

HST observed SDSS J0845+2257 on 2010 March 31 and 2010 April 1 with the Cosmic Origins Spectrograph (COS, Green et al., 2012). Eight orbits were awarded under proposal ID 11561 for a total exposure time of 2735 s, 4994 s and 14397 s with the G130M, G160M and G230L gratings respectively. The spectra were processed with CALCOS 2.12. Both the FUV (1120–1800 Å, Figure 4.1) and NUV (1600–2060 Å, 2470–3150 Å, Figure 4.2) spectra show a host of metal absorption lines, with only small amounts of continuum remaining.

Optical observations of SDSS J0845+2257 were obtained at the VLT on 2008 April 3–5, 2009 January 8 and 2009 April 9–11 with the Ultraviolet and Visual Echelle Spectrograph (UVES, Dekker et al. 2000) and again on 2011 January 29 and 2014 October 20 with X-shooter (Vernet et al., 2011). Total exposure times were 47520 s with UVES and 10721 s with X-shooter. These observations were reduced using the standard procedures within the REFLEX[1] reduction tool developed by ESO. A heliocentric correction was applied to the REFLEX outputs, and multiple exposures from the same night were combined. The optical spectra show a large number of absorption lines, indicative of pollution from a variety of metals. The 8600 Å Ca II emission line triplet is also clearly visible in all of the observations (see Section 4.4) .

[1]The REFLEX software and documentation can be obtained from `http://www.eso.org/sci/software/reflex/`

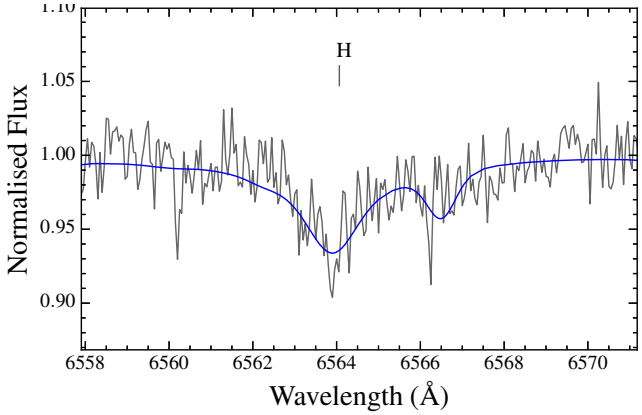

Figure 4.5: Section of our UVES spectrum showing a weak Hα absorption line. Fitting an atmospheric model (blue) to the spectrum results in log (H/He)=−5.10 ± 0.50.

On 2010 April 2 we obtained six spectra of SDSS J0845+2257 using the Gemini Multi-object Spectrograph on Gemini South (GMOS, Hook et al., 2004). The observations were made in service mode, using the R831 grating and a 1″ slit, which gave a wavelength range of 7540–9665 Å at a resolution of 2.0 Å. We requested the acquisition to be done in the *i* band to ensure that the target was properly centred on the slit in the region of the Ca II lines. We reduced and extracted the spectra using the STARLINK software packages KAPPA and PAMELA, and then applied the wavelength and flux calibration using MOLLY[2]. The wavelength calibration was derived from a CuAr arc exposure taken in the morning following the observations and adjusted according to the known wavelengths of strong night sky emission lines. The flux calibration was calculated using an observation of the spectroscopic standard star LTT3218. Finally, we combined the six individual exposures to give a single, high signal-to-noise spectrum with a combined exposure time of 4980s. The strength of the 8600 Å Ca II triplet in this spectrum is comparable to the other optical observations.

4.2 White dwarf parameters

The spectroscopic determination of atmospheric parameters for hot DB white dwarfs is extremely difficult, because the spectra hardly change between $T_{\rm eff}$ = 20000 − 30000 K. Using a fit to the SDSS photometry with a fixed $\log g$ = 8.00, we obtain $T_{\rm eff}$ = 19850 ± 600 K for a pure He grid, $T_{\rm eff}$ = 19890 ± 620 K for a grid with log (H/He)= −5.0, and $T_{\rm eff}$ = 19880 ± 600 K for a grid with our final metal abundances. The increase of the free electron density, which is the major effect from the inclusion of metals in cooler DB models, has no significant effect at these temperatures. There is, however, a noticeable blanketing

[2]MOLLY was written by T. R. Marsh and is available from `http://www.warwick.ac.uk/go/trmarsh/software/`.

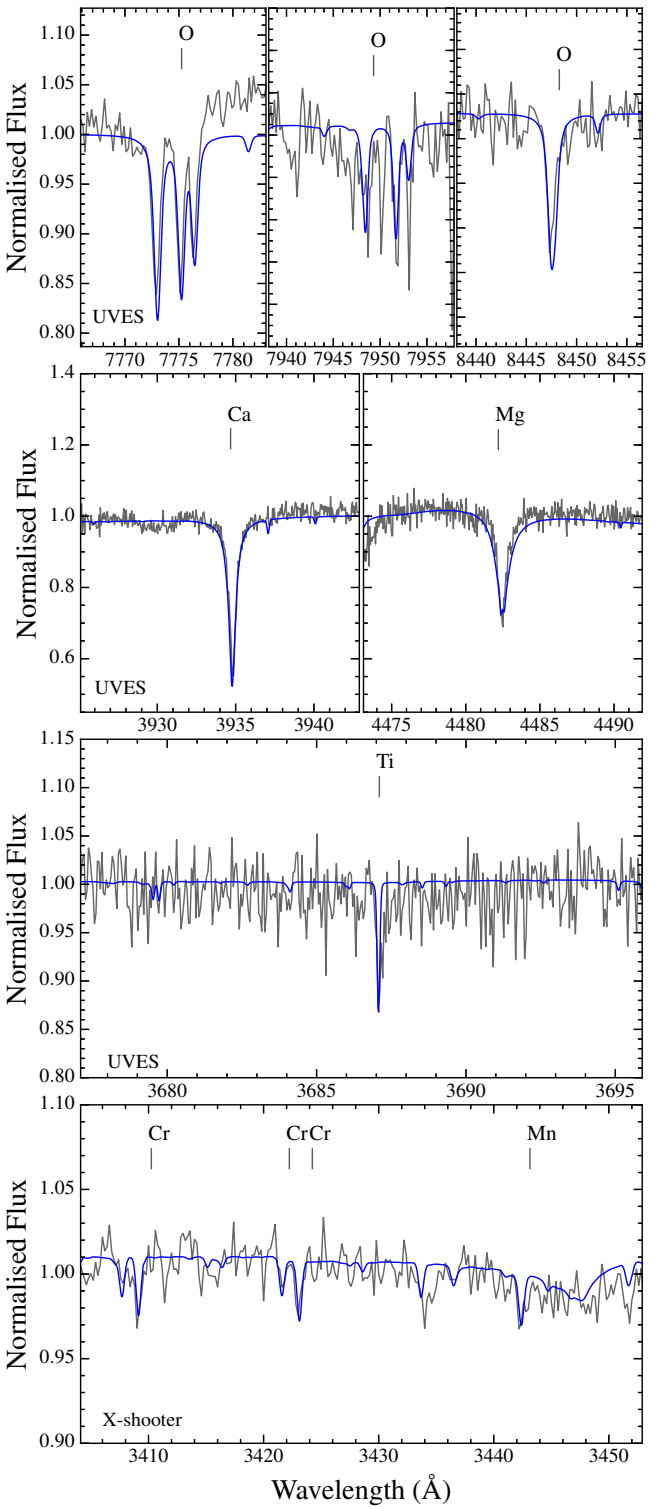

Figure 4.6: Normalised sections of X-Shooter and UVES spectra showing absorption lines from O, Ca, Mg, Ti, Cr and Mn, with the model atmosphere fit used to calculate the abundances over-plotted in blue. The section shown in the top-middle panel is affected by telluric lines, which are not reproduced by our model.

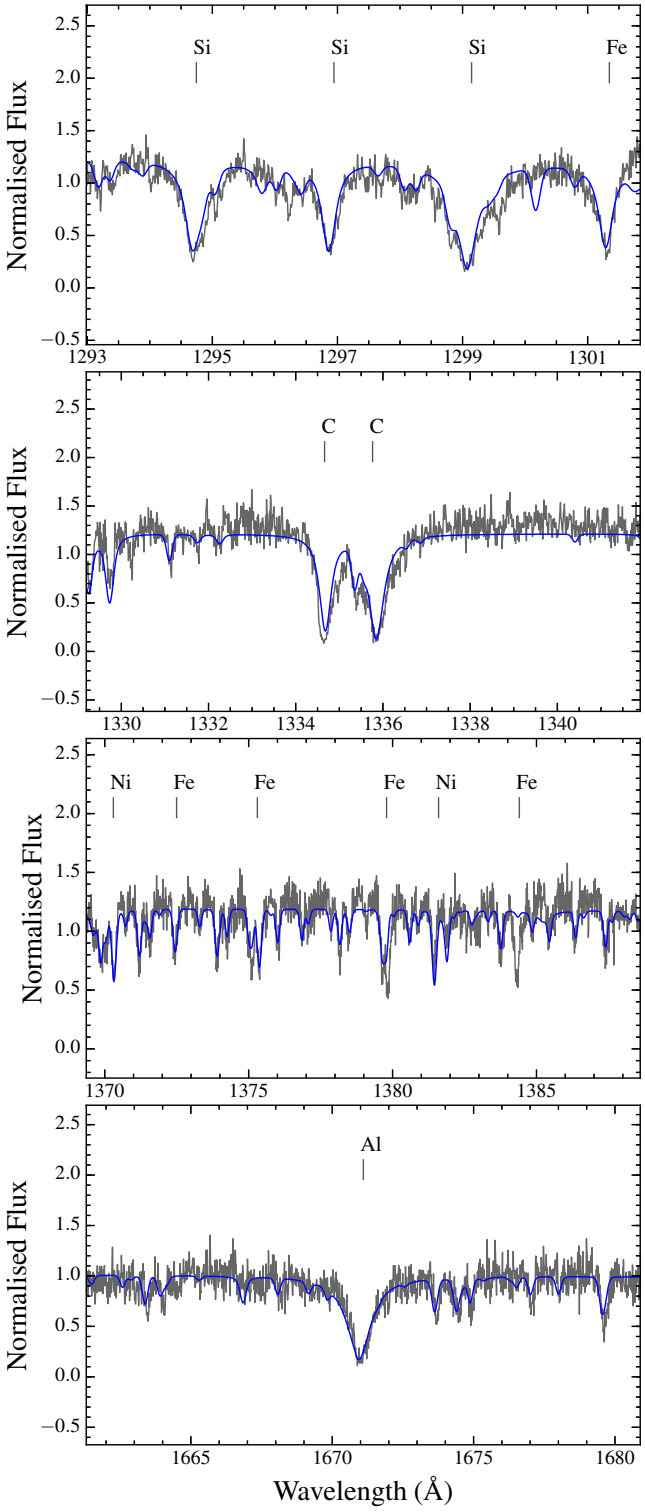

Figure 4.7: Sections of the COS FUV spectrum showing absorption lines from Si, C, Ni, Fe and Al, with the model atmosphere fit used to calculate the abundances over-plotted in blue.

effect from the strong metal lines in the ultraviolet. This increases the overall flux in the optical range, but with the same factor in all SDSS band passes. It therefore has no effect on the atmospheric parameter determination.

A possible difficulty when using the photometry for faint and distant objects is the interstellar reddening. The maximum reddening in the direction of SDSS J0845+2257 is E(B-V) = 0.0268 (Schlafly & Finkbeiner, 2011). If we apply this value and repeat the fitting with the dereddened photometry, the result is a much higher temperature of $T_{\rm eff}$ = 24320 ± 920 K. From the solid angle obtained through this fit, and assuming a radius of the white dwarf which corresponds to $\log g = 8.0$, we can obtain the distance to the white dwarf and estimate the true reddening. We find a distance of 117 pc and a vertical distance above the galactic plane of 67 pc. Using the algorithm of Tremblay et al. (2011a, see also Genest-Beaulieu & Bergeron 2014), we estimate a negligible reddening of $E(B-V) = 0.001$, and thus the lower $T_{\rm eff}$ is secure.

The atmospheric parameters from the photometry are confirmed by a fit to the SDSS spectrum, which results in $T_{\rm eff}$ = 19800 ± 70 K, $\log g$ = 8.16 ± 0.02 for the pure He grid, and $T_{\rm eff}$ = 19780 ± 70 K, $\log g$ = 8.18 ± 0.02 for the grid with log (H/He) = −5.0. A final test is offered by the absolute calibration of the *HST* spectra. Using the solid angle from the photometry, the effective temperature is confined to $T_{\rm eff}$ = 19750 ± 250 K by the comparison of the predicted ultraviolet fluxes with the observations. Our final compromise for the atmospheric parameters is the spectroscopic fit with the log (H/He) = −5 grid, with enlarged errors:

$$T_{\rm eff} = 19780 \pm 250\,{\rm K} \qquad \log g = 8.18 \pm 0.20$$

The hydrogen abundance is consistent with a fit to the Hα line found in the UVES spectrum (Figure 4.5).

Jura et al. (2015) rely entirely on a fit to the SDSS photometry, obtaining $T_{\rm eff}$ = 19535 ± 700 K for a pure He grid and $T_{\rm eff}$ = 18700 ± 700 K for a grid with the observed metal abundances. The surface gravity cannot be obtained from the photometry so they fixed $\log g = 8.00$. We have computed a model adopting the parameters of Jura et al. (2015) and multiplied it with the solid angle obtained from their photometric fit. Their lower $T_{\rm eff}$ under-predicts the COS ultraviolet fluxes by 15–23 percent. Whilst a temperature difference of 1000 K would not normally have a large effect on the metal abundances, in this case all elements heavier than oxygen are in a transition from first to second ionization stage so the predicted lines in our (hotter) model are significantly weaker. We thus obtain larger abundances for all elements, with the exception of carbon. Our carbon abundance is based on the COS ultraviolet spectroscopy, which contains more and stronger carbon lines than the optical data analysed by Jura et al. (2015). An independent model atmosphere analysis of the COS ultraviolet spectra of SDSS J0845+2257 carried out by P. Dufour (private com-

Table 4.2: Measured atmospheric abundances, computed diffusion time-scales and inferred metal accretion rates in the atmosphere of SDSS J0845+2257.

Element	$\log n(\mathrm{Z})/n(\mathrm{He})$	$\tau_{\mathrm{diff}}(10^4\mathrm{yr})$	$\dot{M}$ (g s^{-1})
1 H	-5.10 ± 0.50	n/a	n/a
6 C	-4.90 ± 0.20	1.5	4.1×10^8
7 N	≤ -6.30	1.5	$\leq 1.9 \times 10^7$
8 O	-4.25 ± 0.20	0.97	3.8×10^9
12 Mg	-4.70 ± 0.15	1.2	1.6×10^9
13 Al	-5.70 ± 0.15	1.2	1.9×10^8
14 Si	-4.80 ± 0.30	1.2	1.5×10^9
16 S	≤ -5.40	1.2	$\leq 4.3 \times 10^8$
20 Ca	-5.95 ± 0.10	0.97	1.9×10^8
21 Sc	≤ -7.70	0.65	$\leq 5.7 \times 10^6$
22 Ti	≤ -7.15	0.59	$\leq 2.4 \times 10^7$
24 Cr	-6.40 ± 0.30	0.53	1.6×10^8
25 Mn	-7.00 ± 0.40	0.49	4.6×10^7
26 Fe	-4.60 ± 0.20	0.87	6.6×10^9
28 Ni	-5.65 ± 0.30	0.44	1.2×10^9
Total			1.6×10^{10}

munication), adopting our atmospheric parameters, confirms the low photospheric carbon abundance.

Using our results for T_{eff} and $\log g$, and the helium atmosphere models of Bergeron and collaborators[3], we find a cooling age $T_{\mathrm{cool}} \approx 100\,\mathrm{Myr}$, white dwarf mass $M_{\mathrm{wd}} = 0.679\,\mathrm{M}_{\odot}$ and radius $R_{\mathrm{wd}} = 0.011\,\mathrm{R}_{\odot}$. Starting from a Rossland optical depth $\tau_{\mathrm{r}} = 100$ and integrating the envelope equations downwards using the equation of state of Saumon et al. (1995), we find a convection zone mass of $\log(M_{\mathrm{cvz}}/M_{\mathrm{wd}}) = -8.4$. Using the initial-to-final mass relationships of Gesicki et al. (2014), Casewell et al. (2009) and Catalán et al. (2008) we find a progenitor mass of $\sim 2.7\,\mathrm{M}_{\odot}$, similar to most metal-polluted white dwarfs (Jura & Xu, 2012; Koester et al., 2014a) and equivalent to an A-type progenitor star.

4.3 Accretion of planetary material

The ultraviolet and optical spectra (Figures 4.1, 4.2 and 4.3) of SDSS J0845+2257 show metal absorption lines from a variety of elements, from which we can confidently measure the atmospheric abundances for hydrogen and 10 metals and place an upper limit on 4 further metals.

[3] `http://www.astro.umontreal.ca/~bergeron/CoolingModels`, based on Holberg & Bergeron (2006), Kowalski & Saumon (2006), Tremblay et al. (2011a) and Bergeron et al. (2011).

Table 4.3: Mass fractions of the accreted debris in the convection zone of SDSS J0845+2257 and in the bulk Earth (Allègre et al., 2001). In the early-phase/instantaneous approximation the mass fractions are calculated using the atmospheric abundances, whilst in steady-state the inferred accretion rates are used. The differences between the two approximations are small for most elements.

Element	Percentage by mass		
	SDSS J0845+2257		Bulk Earth
	Early-Phase	Steady-State	
6 C	4.0 ± 1.8	2.5 ± 1.2	0.17
8 O	23.8 ± 11.0	23.4 ± 10.8	32.4
12 Mg	12.7 ± 4.4	9.9 ± 3.4	15.8
13 Al	1.4 ± 0.5	1.2 ± 0.4	1.5
14 Si	11.8 ± 8.1	9.3 ± 6.4	17.1
20 Ca	1.2 ± 0.3	1.2 ± 0.3	1.62
24 Cr	0.55 ± 0.38	0.99 ± 0.68	0.42
25 Mn	0.15 ± 0.13	0.28 ± 0.26	0.14
26 Fe	37.3 ± 17.1	40.8 ± 18.8	28.8
28 Ni	3.4 ± 2.4	7.5 ± 5.2	1.69
Other	3.7	2.9	1.08

The spectra show many dozens to hundreds of lines of Mg, Si, Ca and Fe, so the measured abundances for those elements are fairly secure (although note the recurrant issue in the fits to two areas of Si lines shown in Figure 4.4). The Ni abundance is confirmed by the clear and moderately strong lines at 1317 Å and 1370 Å. Our carbon abundance is based on more than 15 strong C I and C II lines between 1270 Å and 1470 Å and thus also fairly robust. The O abundance relies on the 7777 Å, 7949 Å and 8448 Å lines shown in Figure 4.6. As with Dufour et al. (2012), we find the abundance obtained using the 7949 Å absorption line to be highly discrepant with the other two lines. As the available atomic data for this line is limited, we have chosen to neglect this point, with the final abundance and error calculated from the remaining two lines. The 1152 Å and 1302 Å lines detected in the ultraviolet spectra allow a less precise measurement which is compatible with this result.

One of the four metals for which we only present upper limits, Ti, is actually detected in our spectra. However there is disagreement between the abundance measurements from lines at 3686 Å and 3762 Å, which fit the quoted abundance value, and the 3760 Å line, which is weaker than predicted by the model. Another line predicted by the model atmosphere, 3901 Å, is not observed. For these reasons we only feel confident to present an upper limit for the abundance of Ti.

To study the composition of the progenitor object we must compute the relative

abundance ratios of the elements being accreted into the white dwarf atmosphere. These are not necesserily identical to the ratios of the photospheric metal abundances derived above, as individual metals sink out of the He envelope on different diffusion time-scales. The diffusion time-scales are a function of the depth of the convection zone and the diffusion velocity of each element, both of which vary with $T_{\rm eff}$ (Koester, 2009).

SDSS J0845+2257 has a shallow ($\log (M_{\rm cvz}/M_{\rm wd}) = -8.4$) convection zone and we assume that the accreted metals are homogeneously mixed, such that the relative ratios of elements near the bottom of the convection zone are the same in the photosphere. We calculate individual diffusion time-scales for each element (column 3 of Table 4.2) using the techniques described in Koester (2009)[4], taking the total mass of helium in the convection zone to be $M({\rm He})_{\rm cvz} = 2.605 \times 10^{-9} {\rm M}_{\odot}$. The accretion rates of each element onto the white dwarf are then proportional to the ratio of the the photospheric metal abundance to the diffusion time-scale, leading to the results in column 4 of Table 4.2.

The accretion/diffusion computations of Koester (2009) assume that accretion has been ongoing for $\gtrsim$5 diffusion time-scales, reaching a steady-state between material diffusing out of the convection zone and accreting onto the white dwarf. This assumption is likely valid as a dusty debris disc is detected (Brinkworth et al., 2012), which is almost certainly the source of the metals. Girven et al. (2012) showed that such discs have an estimated lifetime of several 10^5 yr. As the diffusion time-scales are only of order 10^4 yr it is reasonable to assume that a steady-state has been reached.

However, we cannot exclude the possibilities that the debris disc formed recently and that accretion and diffusion have not reached a steady-state (the early-phase), or that the accretion rate may not be constant over sufficiently long time-scales. The presence of a gaseous component to the debris disc (Section 4.4) has been suggested to be the result of dynamical activity in the disc (Veras et al., 2014b), which may affect the accretion rate. As the lifetime of the gaseous component is likely to be short relative to the diffusion time-scale (Chapter 3), its presence may be a sign of recent changes in the accretion rate. In this case, known as the instantaneous assumption, the relative chemical abundances in the accreted material will match the photospheric abundances. Jura et al. (2015) based their analysis of the debris composition on the instantaneous assumption, as at the $T_{\rm eff} = 18700\,{\rm K}$ used in their analysis the diffusion time-scales are much longer, making it much less likely for the accretion to have reached a steady-state.

Table 4.3 shows the relative mass fractions of the elements under both the steady-state and early-phase/instantaneous scenarios. We find that the choice of accretion scenario has only a small effect on the elemental mass fractions, with the possible exceptions of

[4]See updated values at `http://www1.astrophysik.uni-kiel.de/koester/astrophysics/astrophysics.html`.

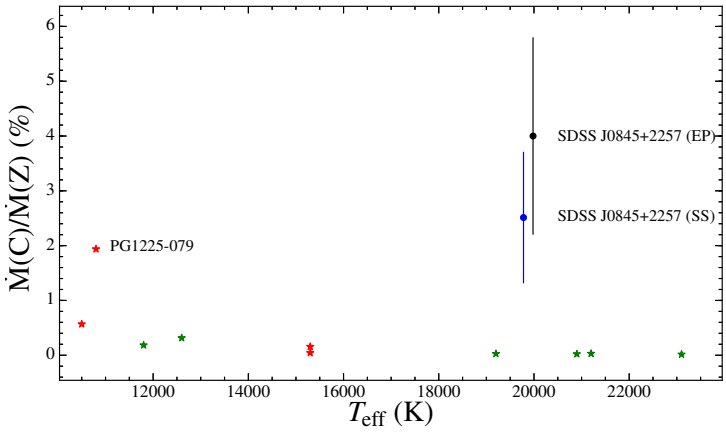

Figure 4.8: Mass fraction of carbon in the accreted material analysed in the most heavily polluted white dwarfs (Zuckerman et al., 2011; Klein et al., 2011; Dufour et al., 2012; Gänsicke et al., 2012; Farihi et al., 2013a; Xu et al., 2013, 2014). Both the early-phase (black) and steady-state (blue) results for SDSS J0845+2257 are shown, with the marker for the early-phase offset by +200 K for clarity. Whilst the carbon fraction is low and roughly constant for both DA (green star symbols) and DB (red star symbols) white dwarfs regardless of $T_{\rm eff}$, there are two clear outliers: PG 1225-079 (Xu et al., 2013) and SDSS J0845+2257.

C and Ni. Our discussion below of the debris composition is based on the steady-state assumption, but we note where the differences between steady-state and early-phase accretion are significant.

4.3.1 Total accretion rate and mass of the parent body

At $1.6 \times 10^{10}\,\mathrm{g\,s^{-1}}$, SDSS J0845+2257 has one of the highest inferred accretion rates detected at a metal-polluted white dwarf, with the observed elements representing the bulk of those making up the Earth (Table 4.3). Any additional undetected elements make up only trace amounts, so we can therefore draw reliable conclusions about the bulk abundances of the accreted material.

The total mass of metals calculated to be in the convection zone is 4.9×10^{21} g, setting a lower limit on the mass of the accreted object (or objects). Assuming a rock-like density of $\rho \approx 2$–$4\,\mathrm{gcm^{-3}}$, the mass is equivalent to a spherical object with a ∼130–170 km diameter. However, detection of circumstellar gas (Gänsicke et al., 2008) and dust (Brinkworth et al., 2012) implies that accretion is still ongoing. If a large proportion of the debris is still in the disc, and/or has already sunk out of the convection zone of the white dwarf, then the total mass of the progenitor object may have been significantly higher than that currently present in the convection zone.

4.3.2 Carbon

Figure 4.8 shows that the mass fraction of carbon in the accreted material for nearly all of the most heavily polluted white dwarfs is $\lesssim 0.5$ percent, regardless of temperature, for both hydrogen (DA) and helium (DB) atmospheres. However two DB white dwarfs, PG 1225-079 (Xu et al., 2013) and SDSS J0845+2257, have much higher carbon abundances. In PG 1225-079, which has a carbon mass fraction of 1.9 percent, Xu et al. (2013) found no exact match of any solar system object and suggested that the accretion may have been caused by two or more objects with different compositions. Jura et al. (2015) found a carbon mass fraction of 15 percent in SDSS J0845+2257, which, assuming that all of the carbon was accreted, is consistent with that of Interplanetary Dust Particles (IDPs). As IDPs are too small to make up the high inferred accretion rate, Jura et al. (2015) suggested that the disrupted rocky body was a Kuiper-belt analogue which lost its water content during the post main-sequence evolution of the system. Although our diffusion calculations still return an unusually high carbon abundance (2.5 percent in steady-state, 4.0 percent in early-phase), it is significantly lower than that found by Jura et al. (2015) and thus does not match the abundances found in IDPs. The large discrepancy between the carbon mass fractions derived from the two studies arises from the combination of a lower photospheric abundance of carbon determined from our COS ultraviolet spectroscopy (Section 4.2) and a systematically higher abundance of heavier elements. However, although the detailed results of the two studies differ, the fundamental conclusion of an unusually large abundance of carbon in the of photosphere of SDSS J0845+2257, when compared to other debris-polluted white dwarfs, remains. We consider several alternative possible explanations for the excess carbon.

Firstly, Veras et al. (2014c) speculated that a small fraction of the debris at white dwarfs could be made up of exo-Oort cloud comets, which do have a substantial carbon fraction (Jessberger et al., 1988). However, comets have a much higher water content than that observed here (Section 4.3.3) and cannot supply enough mass to explain the high rate and total amount of accreted metals.

Another scenario that could explain the high carbon abundance in SDSS J0845+2257 is based on results from terrestrial seismology, which have shown that a portion of the Earth's core must be made up of less dense material than the majority Fe and Ni (Allègre et al., 1995). Carbon has been suggested as a possible candidate for this material (Poirier, 1994; Zhang & Yin, 2012). The enhanced levels of known core elements (Table 4.3, Section 4.3.5) at SDSS J0845+2257 could therefore explain the increased carbon abundance. However, the similarly enhanced level of core material detected in PG 0843+516 (Gänsicke et al., 2012) was not accompanied by an increase in the carbon mass fraction.

An alternative explanation is that the carbon has not been accreted from planetary

debris, but is instead primordial to the white dwarf. A number of DB white dwarfs have been observed with atmospheric pollution from carbon, but no other metals (Provencal et al., 2000; Koester et al., 2014b). These white dwarfs span a range of $T_{\rm eff}$ and no single explanation (in the absence of accretion) can currently explain the high carbon abundances. At temperatures $\lesssim$ 16000 K convection can dredge up carbon from the core into the helium layer (Koester et al., 1982), although some DBs have been observed with carbon abundances much lower than predicted by this model (Desharnais et al., 2008). We note that the maximum contamination by dredge-up is thought to occur near 12000 K (Pelletier et al., 1986), providing an entirely plausible source for the carbon detected in PG 1225-079, which has $T_{\rm eff}$ = 10800 K (Xu et al., 2013). The carbon in hotter (>20000 K) white dwarfs, which cannot be explained by the classical dredge up model, has been postulated to be raised by a weak stellar wind (Fontaine & Brassard, 2005), but there is currently no working model for the necessary wind acceleration. Both the dredge-up and stellar wind models predict a very low carbon abundance in the temperature range ~17000–20000 K.

However, the efficiency of photospheric carbon pollution by dredge-up depends not only on the depth of the convection zone, but also on the total mass of the helium layer (Weidemann & Koester, 1995). The bulk of the DQ white dwarfs can be modelled with helium envelopes of $\simeq 10^{-3} - 10^{-2}\,M_{\odot}$ (e.g. Fontaine & Brassard, 2005), which is in agreement with the helium masses predicted by stellar evolution models (e.g. Lawlor & MacDonald, 2006). However, a number of DB white dwarfs (Koester et al., 2014b), cooler DQ (Dufour et al., 2005; Koester & Knist, 2006), as well as the recently discovered hot DQ white dwarfs (Dufour et al., 2007, 2008) have higher carbon abundances than predicted by the canonical dredge-up scenario, which can be explained with thinner helium layers (Althaus et al., 2009; Koester et al., 2014b). Assuming that the unusually high carbon abundances in SDSS J0845+2257 are a result of dredge-up would require a thin (log ($M_{\rm He}/M_{\rm wd}$)~ -4.6) helium layer. In the light of the ongoing discussion of carbon abundances in helium atmosphere white dwarfs, and in the absence of a robust sample of helium layer measurements for white dwarfs, we conclude that dredge-up is a plausible origin of the photospheric carbon in SDSS J0845+2257.

An independent evaluation of the origin of the atmospheric carbon may be provided by the models of Hartmann et al. (2014), which predict that even a relativity small mass fraction of carbon ($>10^{-4}$) in the circumstellar debris should lead to emission from gaseous C II at 8683 Å and 8697 Å. Given that we do detect emission from gaseous Ca II (Section 4.4), the non-detection of C II could be further evidence that the carbon is primordial to the white dwarf. Hartmann et al. (2011) applied the same model to the gaseous disc around SDSS J1228+1040, again finding that the absence of C II 8683 Å and 8697 Å emission features in spectra obtained by Gänsicke et al. (2006) requires a low ($\lesssim$0.5 percent) carbon

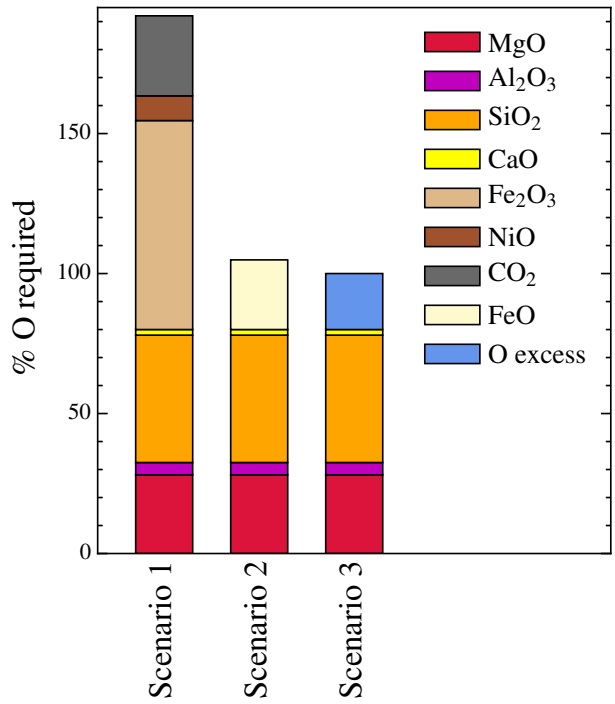

Figure 4.9: Oxygen budgets of the debris at SDSS J0845+2257, with three scenarios for different contributions of oxygen carriers: 1. All Fe as Fe_2O_3, CO_2 and NiO present; 2. 50 % of Fe as FeO; 3. All Fe is metallic, making no contribution to the O budget. The third model is the only one to produce a marginal oxygen excess, suggesting that very little water was present in the parent body.

mass fraction in the gas. Gänsicke et al. (2012) showed that SDSS J1228+1040 has an extremely low photospheric carbon abundance, unambiguously demonstrating that the debris disc in this system is indeed strongly carbon-depleted.

4.3.3 Oxygen

Measurements of the oxygen abundance in the accreting white dwarf GD 61 by Farihi et al. (2013a) suggested that a large fraction of the debris was made of water. To estimate the water content in the debris around SDSS J0845+2257 we follow the procedure of Farihi et al. (2013a), assessing first oxygen carriers other than water. We assume that all of the accreting Mg, Al, Si, and Ca is bound into MgO, Al_2O_3, SiO_2 and CaO. If the debris is a fragment of a differentiated object then the Fe and Ni content may be split into oxides from the mantle and metallic Fe and Ni from the core, so we present three scenarios for the remaining elements (Figure 4.9) 1. A conservative scenario where all of the Fe is bound into Fe_2O_3, Ni into NiO and C into CO_2; 2. An intermediate scenario where C is primordial (see

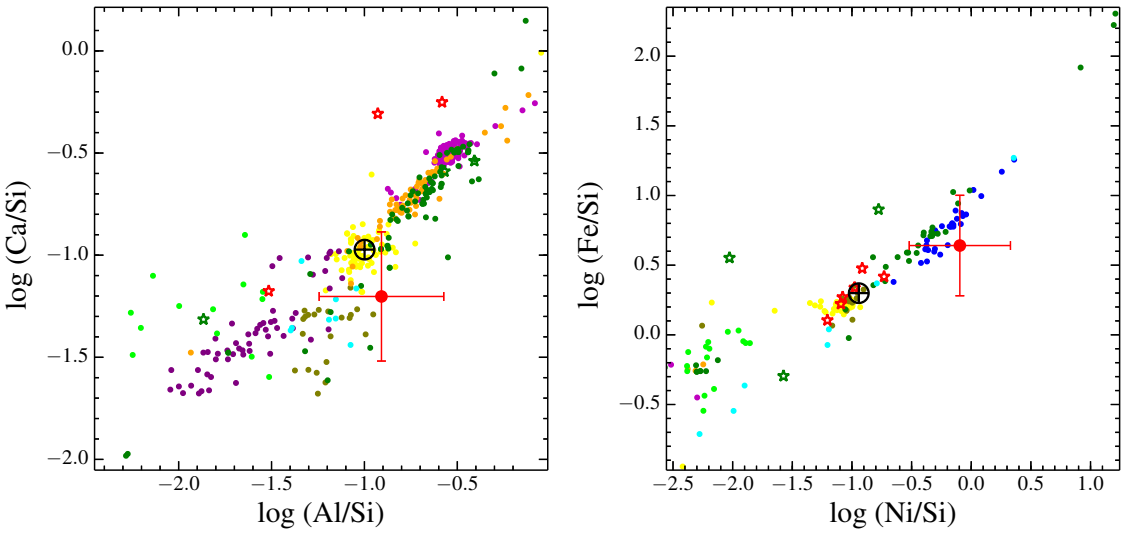

Figure 4.10: Comparison of the abundance of Al and Ca (left) and Fe and Ni (right) in SDSS J0845+2257 (red marker) with the bulk Earth (⊕) (McDonough, 2000) and the allasite (blue), mesosiderite (dark green), IAB (cyan), urelite (light green), ordinary chrondrite and carbonaceous chrondrite (yellow), enstatite chrondrite (green-brown), Howardite (orange), Eucrite (magenta) and Diogenite (purple) meteorites (Nittler et al., 2004). The most heavily metal-polluted white dwarfs are plotted as green (DAZ) and red (DBZ) stars (Zuckerman et al., 2011; Klein et al., 2011; Dufour et al., 2012; Gänsicke et al., 2012; Xu et al., 2014, 2013; Farihi et al., 2013a; Xu et al., 2014). All abundances are normalised to Si.

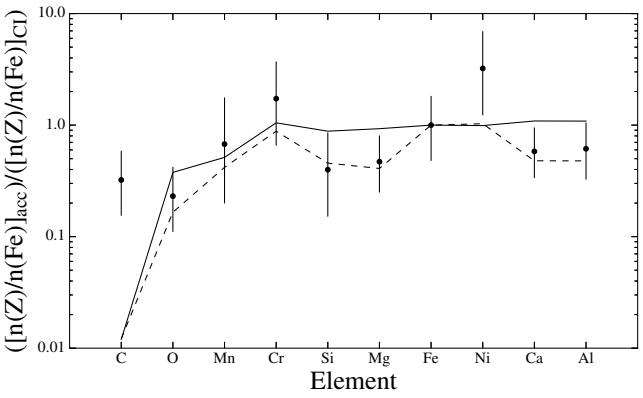

Figure 4.11: Elemental abundances of the accretion onto SDSS J0845+2257 relative to the abundance in CI chondrites, both normalised to Fe (black dots). The condensation temperature of the elements increases to the right. The solid line shows the abundances of the bulk Earth, whilst the dotted line shows a 'wind stripped' model (Melis et al., 2011) in which approximately 15 percent of the silicate Earth has been removed.

Section4.3.2), the contribution from Ni is negligible and half the Fe is present as FeO; 3. A mantle depleted scenario, discussed further in Section 4.3.5, where there is no contribution from Fe, Ni or C. Only the third of these scenarios produces an oxygen excess, indicating that the accreted material was likely dry regardless of the relative contributions from mantle and core material, as well as from carbon. This result is consistent with the low H abundance detected in the atmosphere (Table 4.2), and is not significantly altered under the assumption of early-phase or instantaneous accretion. Scenario 1 shows that there is insufficient oxygen to account for all of the potential carriers, an indicator that a large fraction of the Fe in the progenitor object was indeed metallic.

4.3.4 Refractory lithophiles

Figure 4.10 compares the abundance of Ca and Al with respect to Si. These elements are two of the main refractory lithophiles: elements which sublimate only at very high temperatures and are therefore found mainly in the mantle and crust of differentiated objects (Grossman, 1972). The ratio of these two elements is nearly constant in most solar system bodies, such that there is a linear correlation between Ca/Si and Al/Si. The Ca and Al accreting onto SDSS J0845+2257, as well as onto the other heavily polluted white dwarfs, also falls onto or near this line. This indicates that similar geochemical processes are taking place in these systems, and strengthens the case that analysing the accreted debris in the white dwarf photosphere provides a reliable representation of the chemical composition of a terrestrial object at SDSS J0845+2257.

4.3.5 Iron and nickel

Table 4.3 shows that the dominant element in the debris at SDSS J0845+2257 is Fe, with a mass fraction of 40.8 percent, substantially higher than in the Earth. Ni, which is the other major component in the Earth's core (McDonough, 2000), is also enhanced relative to the Earth. Figure 4.10 shows the linear relationship between Fe/Si and Ni/Si found in the solar system bodies. Whilst the heavily polluted DB white dwarfs also fall on this line, the DA white dwarfs are less confined. SDSS J0845+2257 is close to the trend but has a higher Ni/Fe ratio (≈ 0.2) than the Earth (0.06). In the early-phase model the Ni/Fe ratio drops to ≈ 0.09.

The high Fe and Ni abundances suggest that the progenitor of the debris at SDSS J0845+2257 may have been a fragment of a larger, differentiated planetesimal with a relatively large core. This could be evidence that some of the processes thought to be responsible for Mercury's large core, such as partial volatilization (Cameron, 1985) or iron/silicate fractionation (Weidenschilling, 1978), also occur in extrasolar planetary systems. However, it is likely that any planet close enough to its star for these processes to occur would have been engulfed during the red giant phase, unless it migrated outwards after formation.

Melis et al. (2011) proposed an alternative model in which a planetesimal is eroded by the intense stellar wind during the asymptotic giant branch (AGB). Figure 4.11 shows this model applied to SDSS J0845+2257. Following the technique detailed in Melis et al. (2011), we show the abundances of the material accreted onto the white dwarf (Table 4.2) relative to the abundances in the CI chondrites (Lodders, 2003), both of which are normalised to Fe. Combining the abundances for the core and silicate Earth from McDonough (2000) we normalise the abundances in the bulk Earth in the same way (solid black line). We then remove ~15% of the silicate material (dotted line in Figure 4.11), simulating the erosion of the mantle of a terrestrial object by stellar wind. We neglect any contribution from the crust, as it makes up only ≈0.5 percent of the silicate Earth (Allègre et al., 1995). As can be seen in Figure 4.11 the dominant elements of both Earth and SDSS J0845+2257 (e.g. Si, O, Mg, Ca, Al) appear to support this model, whilst the trace elements (Mn, Cr) are consistent with both scenarios. The high abundances of C (if accreted, see Section 4.3.2) and Ni remain unexplained, although Ni does become consistent with the model under the early-phase assumption. We note that, whilst Jura (2008) explored the effects of stellar winds on small asteroids, no detailed modelling has been done for the stripping of larger objects and it is unclear if the stellar wind during the AGB can provide the level of erosion suggested here and in Melis et al. (2011).

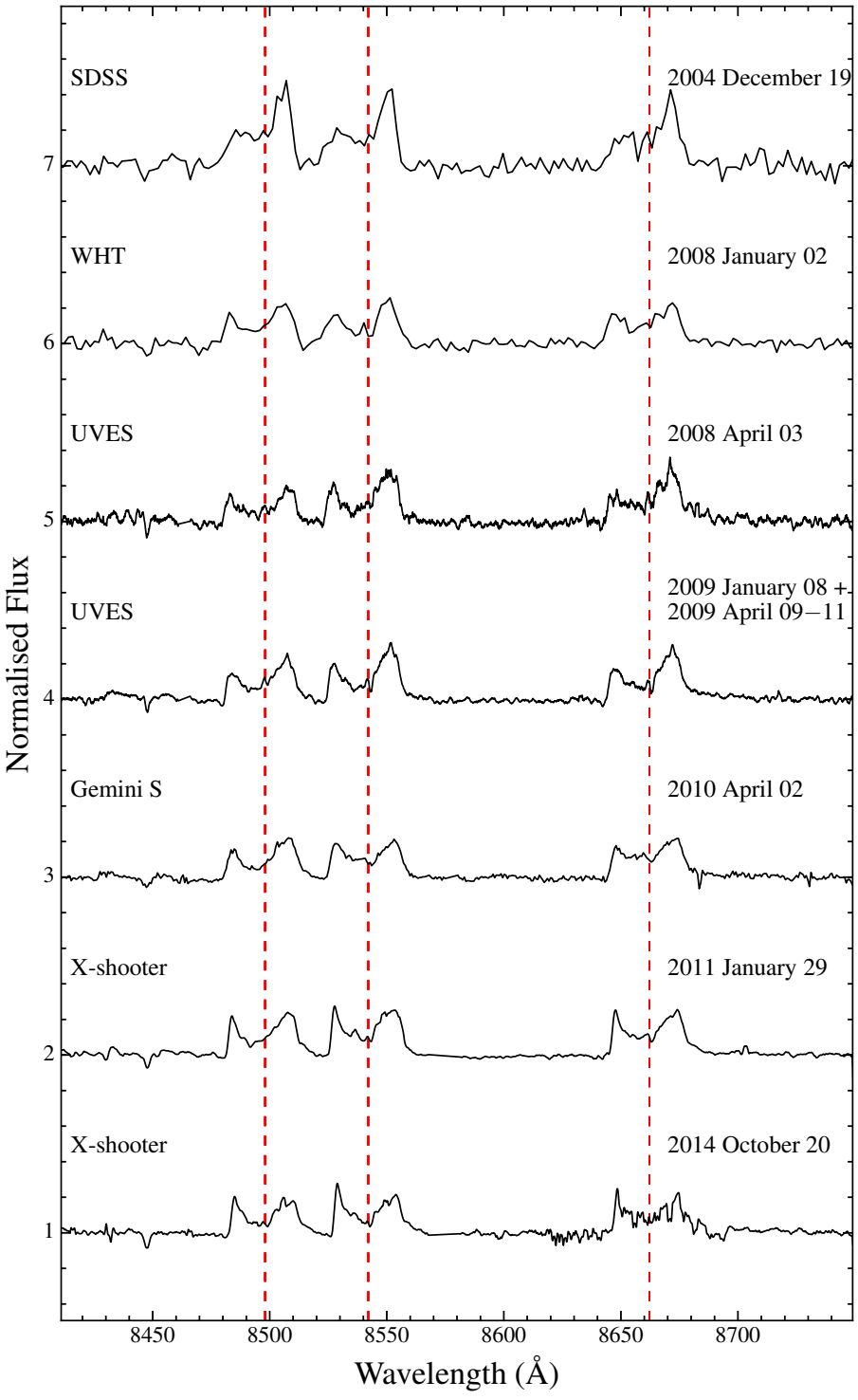

Figure 4.12: Time-series spectra of the Ca II 8600 Å emission line triplet, plotted on the same scale with each successive spectrum offset by 1. The red dashed lines show the rest wavelength positions of the Ca II triplet. The SDSS data from 2004 show a pronounced asymmetry between the two peaks, with the red peak significantly greater in strength. This difference has since vanished, although in the most recent two spectra the blue peak appears marginally stronger.

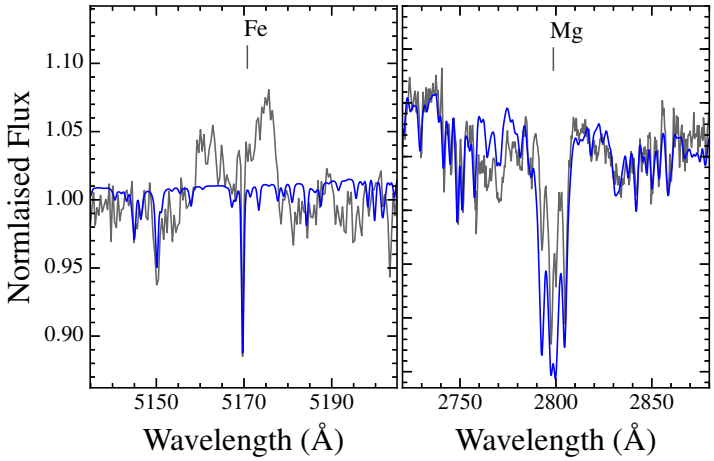

Figure 4.13: Left: Example of weak double-peaked emission from Fe II. Right: The emission from Mg II predicted by Hartmann et al. (2014) is not detected, but could be masked by the photospheric absorption lines. The model atmosphere fit (blue) over-predicts the strength of the Mg II absorption, which could be due to some flux contribution by emission from the gaseous disc.

Table 4.4: Change in the equivalent width of the Ca II 8600 Å emission line triplet. The strength of the triplet dropped in the period 2004–2008, but has remained stable to within $1\,\sigma$ since.

Date	Ca II 8600 Å Equivalent Width (Å)
2004 December 19	-16.9±2.2
2008 January 02	-10.3±1.3
2008 Apri1 03	-10.8±1.4
2009 April 10	-11.4±1.4
2010 April 02	-10.5±1.3
2011 January 29	-12.8±1.5
2014 October 20	-8.6±1.1

4.4 Variability of the Ca II triplet

Like SDSS J1617+1620 (Chapter 3), SDSS J0845+2257 is part of a rare subset of metal-polluted white dwarfs that show double-peaked emission in the 8600Å Ca II triplet, indicative of a gaseous component to the debris disc.

Time-series observations of the 8600 Å Ca II triplet are shown in Figure 4.12. The double-peaked morphology arises from the Doppler shifts induced by the Keplerian velocity of the material in the disc (Horne & Marsh, 1986), a consequence of which is that the inner and outer radii of the disc can be estimated from the total width and peak separation of the Ca II lines respectively. We find $R_{\rm in} \sin^2 i \approx 0.3\,{\rm R}_{\odot}$ and $R_{\rm out} \sin^2 i \approx 0.8\,{\rm R}_{\odot}$, (where i is the unknown inclination of the disc), consistent with the measurements of Gänsicke et al. (2008). Modelling the observed infrared excess, Brinkworth et al. (2012) estimated the extent of the dusty disc to extend from $R_{\rm in} \approx 0.17\,{\rm R}_{\odot}$ to $R_{\rm out} \approx 99.7\,{\rm R}_{\odot}$, although the outer radius of the disc is unconstrained due to the lack of observations at longer wavelengths. The overlap of these values strongly suggests that the gaseous and dusty components are co-orbital. Hartmann et al. (2014) attempted to better constrain the parameters of the gaseous disc component using a non-LTE spectral model, but were unable to obtain a satisfactory fit to the emission lines.

The debris discs have provided some of the clearest evidence for variability in evolved planetary systems, in particular the rapid appearance and loss of the gaseous disc around SDSS J1617+1620 (Chapter 3) and the drop in infrared luminosity from the dust at WD J0959–0200 (Xu & Jura, 2014). Similar, although less pronounced, changes are observed in the 8600 Å Ca II emission line triplet of SDSS J0845+2257. Table 4.4 lists the change in equivalent widths of the Ca II emission lines over time. The equivalent width was calculated over all three double peaked lines to avoid systematic uncertainties caused by the overlap between the 8495 Å and 8542 Å components. The main source of uncertainty in the measurement is the polynomial fit used to normalise the spectrum. To account for this the fit was varied slightly and the resulting scatter in the equivalent width measurements incorporated into the stated error. The data demonstrate a $\approx$1/3 drop in the equivalent width of the emission lines between 2004 and 2008, but the strength of the lines has remained constant to within $1\,\sigma$ since then. In addition, the time-series spectra (Figure 4.12) show pronounced changes in the morphology of the lines. In the 2004 SDSS observation in the red-shifted peaks were substantially stronger, but in more recent observations they have decreased in strength. Conversely the blue-shifted peaks have grown, to the extent that they have become slightly stronger than the red peaks in the latest observations. Due to the relatively low cadence of the time-series observations compared with SDSS J1617+1620 we can only speculate about the cause of this variability, e.g the interaction with a debris stream formed

by a tidally disrupted planetesimal (see for example Debes et al., 2012; Veras et al., 2014b).

In addition to the Ca II emission line triplet, some of our spectra show double-peaked emission around the Fe II 5170Å line (Figure 4.13, left panel). The Fe II emission is weaker and less variable than the emission from Ca II, with an average equivalent width of -0.8±0.5 Å. Hartmann et al. (2011) predicted emission from the gaseous disc from 2797Å Mg II, and detected it in the *HST* spectrum of SDSS J1228+1040. We do not detect emission from Mg II in SDSS J0845+2257 (Figure 4.13), although the observed Mg II absorption line triplet is weaker than predicted by the model atmosphere fit, possibly due to a small flux contribution from a disc emission line.

4.5 Short term variability

To probe for any variability in the flux from SDSS J0845+2257 caused by ongoing metal accretion, we used the time-tag *HST*/COS photon event files to construct a lightcurve. To perform the background subtraction for each of the six individual G130M/G160M observations we defined two regions on the COS detector, one below and one above the spectrum. The 1200 Å Ni I, 1216 Å Lyman α and 1302 Å O I airglow emission lines were masked and the edges of the detector segments excluded to reduce the instrumental noise.The box for the extraction of the spectrum was defined so that all counts of the target were included, while minimising the amount of background contribution. Figure 4.14 shows a background-subtracted, normalised lightcurve binned to 5 seconds.

Setting a null hypothesis that each lightcurve chunk is constant at the mean value, we find that a constant lightcurve has an 8–90 percent probability of having the observed distribution, meaning that we can not reject the hypothesis that the lightcurve is constant. The large range in probability is caused by the different total exposure times of the individual lightcurve chunks.

To confirm this result and investigate any contribution to the variability from the background we repeated the process, this time with a wider box for extracting the spectrum to incorporate more background counts, as well as an identical test across the whole lightcurve. The difference in the results is not significant, so we conclude that the *HST*/COS data does not show significant variability on time-scales of 32 ms to $\simeq$ 30 minutes.

No transits by planets or planetesimals are detected. This non-detection is unsurprising due to the short duration of the observations and the fact that close-in planets around white dwarfs are probably rare (Veras & Gänsicke, 2015).

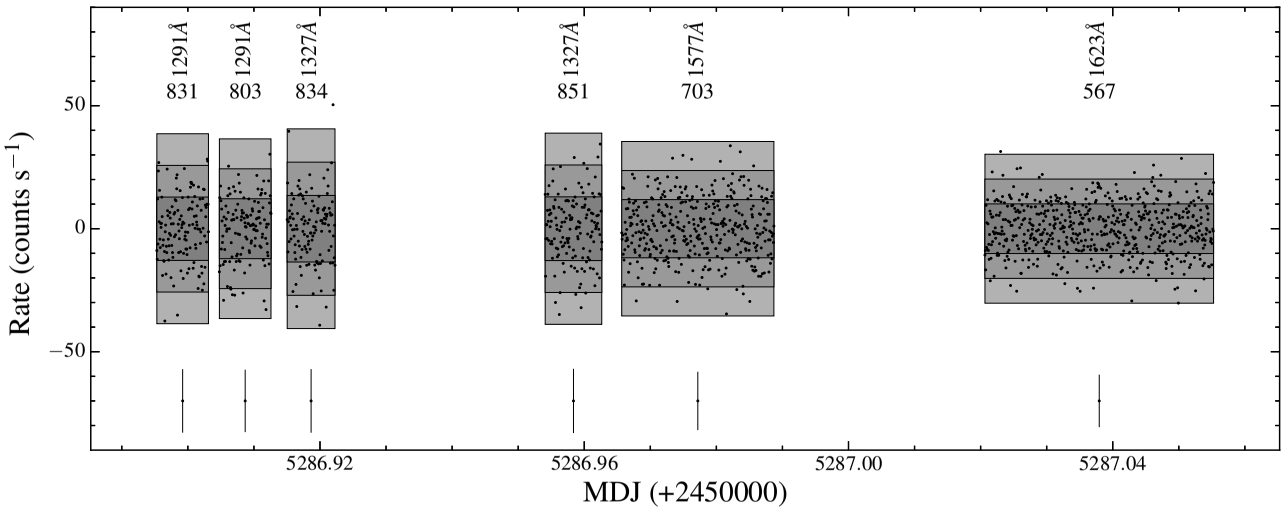

Figure 4.14: Background-subtracted, normalised lightcurves of SDSS J0845+2257, extracted from the *HST*/COS time-tag data. Dark grey, grey and light grey areas represent 1-σ , 2-σ and 3-σ standard deviations from the mean respectively, assuming a normal distribution for the count rate in each observation. The vertical and horizontal numbers above each spectrum are the central wavelength and mean count rate, respectively. An error bar showing the typical photon noise is shown beneath each spectrum.

4.6 Conclusion

We have carried out a detailed spectroscopic study, over a wide wavelength range, of the metal-polluted white dwarf SDSS J0845+2257. The star is accreting debris at a rate of $1.6 \times 10^{10}\,\mathrm{g\,s^{-1}}$ and the mass of metals in the convection zone implies a parent body $\gtrsim$ 100 km in diameter. Measurements of ten metals have shown that the disrupted planetesimal was similar to the Earth in composition, with a differentiated chemistry dominated by O, Mg, Si and Fe. The relativity high levels of Fe and Ni suggests that the planetesimal may have had a portion of its mantle stripped during the AGB phase, leaving a composition dominated by core material. An unusually large amount of carbon is present, although this could be primordial to the white dwarf. The white dwarf is also orbited by a debris disc with a mildly variable gaseous component.

Chapter 5

Carbon to oxygen ratios in extrasolar planetesimals

"Some humans would do anything to see if it was possible to do it. If you put a large switch in some cave somewhere, with a sign on it saying 'End-of-the-World Switch. PLEASE DO NOT TOUCH', the paint wouldn't even have time to dry."

Terry Pratchett, Thief of Time

Based on Wilson et al. (2016). Boris Gänsicke contributed to the analysis and provided observational data, Jay Farihi assisted with the analysis and Detlev Koester provided white dwarf model atmospheres.

The ongoing search for extrasolar planets has been spectacularly successful, with over 3000 candidate and confirmed planets discovered to date[1], including many small objects suspected of being rocky. For a subset of these smallest detected exoplanets, both precision radial velocity measurements and transit photometry have been obtained. This provides a measurement of their masses and radii, and therefore their bulk densities. Intriguingly, these densities have a wide spread, and do not follow a simple mass-radius relationship (Weiss & Marcy, 2014; Dressing et al., 2015). This may imply that some small exoplanets have compositions distinct from the rocky (and icy) planets and moons of the Solar System, which are all, to first order, a combination of H_2O, $MgSiO_3$ and Fe (Allègre et al., 2001). Modelling exoplanets with a greater variety of bulk chemistries may account for the differences in bulk densities. However, it is impossible to unambiguously infer the internal composition of a planet from its density alone. Seager et al. (2007) and Sohl et al. (2012) computed mass-radius relationships for different planetary compositions, finding a significant degeneracy between different densities, interior structures and compositions.

It has been hypothesized that enhanced C/O levels (relative to the Solar value) in a protoplanetary disc could change the condensation sequence of planetary solids, preferentially forming carbon compounds (Kuchner & Seager, 2005; Moriarty et al., 2014). Under conditions where carbon is the most abundant metal, "carbon planets" may form. The alternative condensation sequence begins with the formation of CO, incorporating all of the available oxygen and restricting the formation of silicates. Excess carbon then forms SiC and graphite, for example. An Earth-sized carbon planet would likely form with an Fe-rich core, surrounded by a mantle of graphite, carbides and, at higher pressures, diamond. Bond et al. (2010) showed that this carbon-based chemistry could become important in protoplanetary discs with C/O $\gtrsim$ 0.8. Carbon could contribute more than half the mass of solid exoplanets formed in such an environment, with only trace oxygen present.

Observational identification of carbon planets is hindered by the inability to measure planetary compositions in-situ, with the exception of the upper atmospheres of a few objects (Deming et al., 2013; Kreidberg et al., 2014). Given the diversity in atmospheric composition between the otherwise chemically similar terrestrial planets in the Solar system, such observations cannot be used to infer the bulk compositions of rocky exoplanets. Neither are the C/O ratios of exoplanet host stars a reliable tracer of disc composition (Teske et al., 2013). Carbon to oxygen ratios in protoplanetary discs computed by Thiabaud et al.

[1] `http://exoplanets.org/`

(2015) show only a weak dependence on the host star abundances. This ratio will also vary within a protoplanetary disc due to regional temperature variations and collisions, amongst other factors (Öberg et al., 2011; Gaidos, 2015).

The only method to reliably determine compositions of exoplanetary bodies is via detection of their debris in the photospheres of white dwarfs (Zuckerman et al., 2007). Recent studies have shown that 25–50 percent of all white dwarfs are polluted by debris from planetesimals (Zuckerman et al., 2003, 2010; Koester et al., 2014a; Barstow et al., 2014), ranging in mass from small asteroids to objects as large as Pluto (Girven et al., 2012; Wyatt et al., 2014). The bulk composition of these exoplanetary bodies can be inferred from the debris detected in the white dwarf photosphere, analogous to how the compositions of Solar System bodies are inferred from meteorites (Lodders & Fegley, 2011). High-resolution spectroscopy of over a dozen metal-polluted white dwarfs has revealed accretion of numerous atomic species, allowing detailed studies of the chemical composition of extrasolar planetesimals (Chapter 4, see also Klein et al., 2011; Gänsicke et al., 2012; Dufour et al., 2012; Jura et al., 2012; Farihi et al., 2013a; Xu et al., 2014; Raddi et al., 2015). Overall, these objects have chemical compositions similar to inner Solar System bodies, dominated by O, Si, Mg and Fe, and volatile depleted (Jura & Young, 2014). However, the detailed compositions can be very diverse, with objects having enhanced levels of core material (Melis et al., 2011; Gänsicke et al., 2012), evidence of post-nebula processing (Xu et al., 2013), and significant mass fractions of water (Farihi et al., 2013a; Raddi et al., 2015).

Thus far, studies of planetesimal compositions at white dwarfs have predominately focused on individual objects. However, the growing sample of abundance studies now allows conclusions to be derived regarding the overall chemical abundances of (solid) exoplanet precursors in a statistically significant sample of systems. Here, we use these data to constrain the occurrence frequency of carbon planets.

5.1 Carbon and oxygen debris abundances at white dwarfs

We present debris abundance measurements for ten white dwarfs observed with the Cosmic Origins Spectrograph on board the *Hubble Space Telescope* (*HST*/COS) as part of Program IDs 12169, 12869, and 12474 (Gänsicke et al., 2012; Koester et al., 2014a). Table 5.1 presents their effective temperatures ($T_{\rm eff}$) and surface gravities ($\log g$), as well as elemental accretion rates. The techniques used to determine these results are described in detail in Koester et al. (2014a), so we only briefly summarise here. Firstly, optical spectra from the SPY survey were refitted with the latest model grid to determine temperatures and surface gravities. If no SPY spectra were available, we used parameters from Gianninas et al. (2011). After correcting for a small systematic difference between the two determinations,

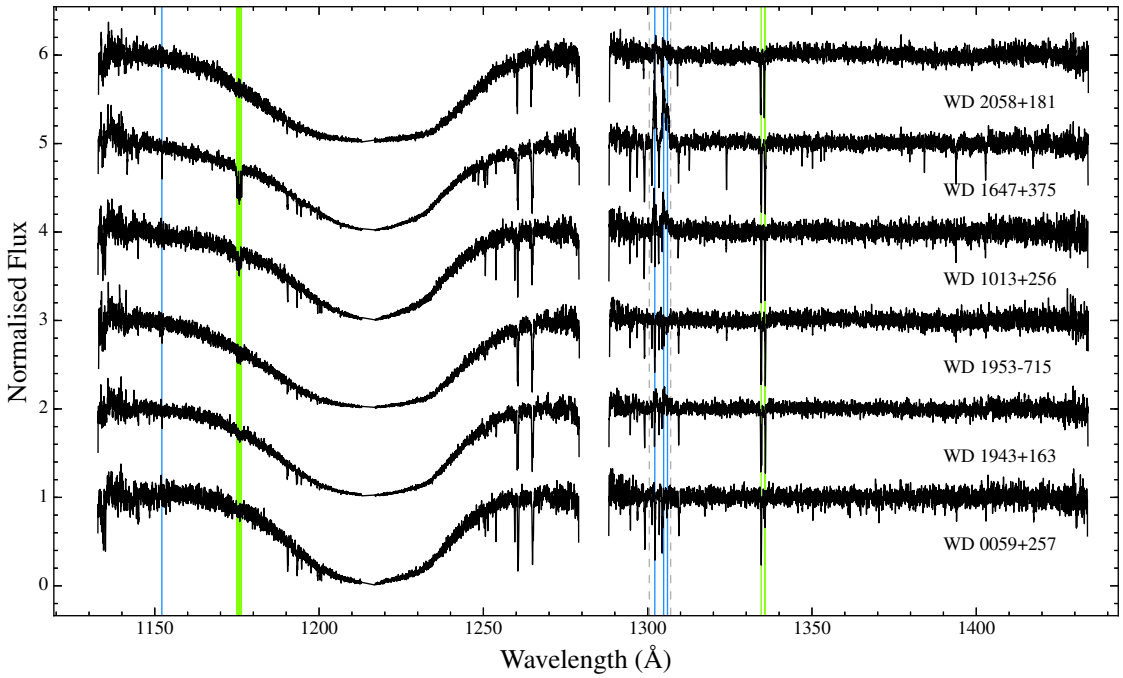

Figure 5.1: *HST*/COS ultraviolet spectra of the first six white dwarfs in Table 5.1. Spectra are smoothed with a 5-point boxcar and normalised, then offset by multiples of 1 for clarity. The spectra are dominated by the broad Lyα line (with the central air glow emission line removed), and absorption lines of several metals are present. The wavelengths of the carbon and oxygen absorption transitions are indicated by the green and blue lines, respectively (Table 5.2). In some of the spectra, the area between the dashed grey lines is affected by geocoronal oxygen emission, which is not corrected for by the COS pipeline.

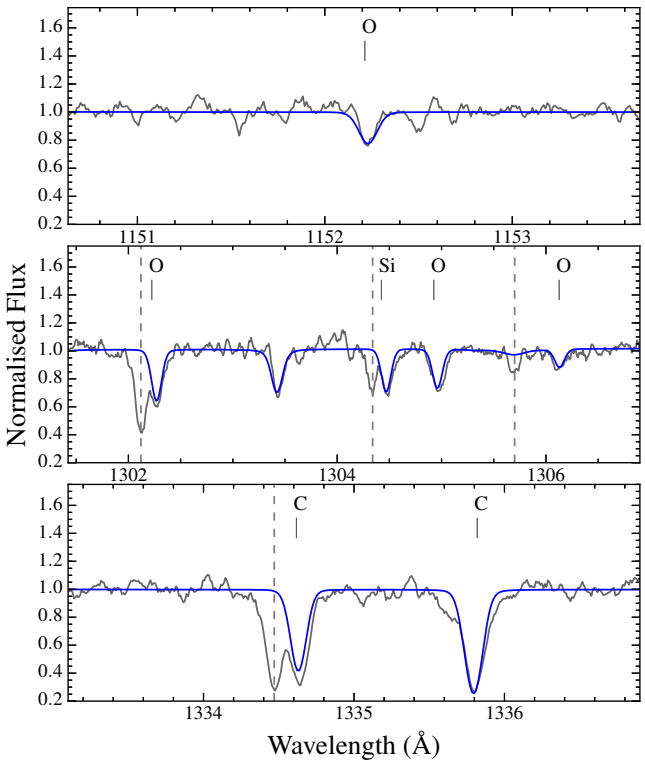

Figure 5.2: Enlarged sections of the spectrum of WD 1953–715 showing photospheric O I 1152.2, 1302.2, 1304.9, 1306.0 Å, Si II 1304.4 Å and C II 1334.5, 1335.6 Å absorption lines. The model atmosphere fit used to calculate the abundances is overlaid in blue. Interstellar components of the O I 1302.2 Å, Si II 1304.4, 1305.6 Å and C II 1334.5 Å absorption lines are marked with dashed grey lines.

Table 5.1: New atmospheric parameters and debris accretion rate measurements for ten white dwarfs identified by Koester et al. (2014a). Spectra of the first six are shown in Figure 5.1. [1]Updated from Gänsicke et al. (2012)

Name	$T_{\rm eff}$ (K)	$\log g$ (cm s^{-2})	$\dot{M}$(C) (g s^{-1})	$\dot{M}$(O) (g s^{-1})
WD 2058+181	17308 ± 235	7.920 ± 0.089	$(2.06 \pm 0.95) \times 10^6$	$(1.03 \pm 0.47) \times 10^7$
WD 1647+375	22803 ± 310	7.902 ± 0.089	$(1.14 \pm 0.52) \times 10^7$	$(2.16 \pm 0.75) \times 10^8$
WD 1013+256	22133 ± 301	8.022 ± 0.089	$(1.92 \pm 0.66) \times 10^6$	$(3.2 \pm 1.6) \times 10^7$
WD 1953–715	18975 ± 258	7.957 ± 0.089	$(1.56 \pm 0.72) \times 10^6$	$(2.8 \pm 1.3) \times 10^7$
WD 1943+163	19451 ± 264	7.896 ± 0.089	$(1.40 \pm 0.64) \times 10^6$	$(1.97 \pm 0.91) \times 10^7$
WD 0059+257	20491 ± 278	8.002 ± 0.089	$\leq 2.9 \times 10^4$	$(3.4 \pm 1.6) \times 10^7$
PG 0843+516[1]	22412 ± 304	7.902 ± 0.089	$(2.42 \pm 1.11) \times 10^5$	$(1.09 \pm 0.50) \times 10^8$
PG 1015+161[1]	18911 ± 257	8.042 ± 0.089	$\leq 6.9 \times 10^4$	$(4.9 \pm 2.3) \times 10^7$
SDSS J1228+1040[1]	20713 ± 281	8.150 ± 0.089	$(1.70 \pm 0.78) \times 10^5$	$(4.4 \pm 2.0) \times 10^8$
GALEX J1931+0117[1]	21457 ± 291	7.900 ± 0.089	$(7.1 \pm 4.9) \times 10^5$	$(9.0 \pm 6.2) \times 10^8$

Table 5.2: List of the absorption lines used for the debris abundance measurements.

Ion	Vacuum rest wavelength (Å)
C II	1334.530, 1335.660, 1335.708
C III	1174.930, 1175.260, 1175.590, 1175.710, 1175.987, 1176.370
O I	1152.150, 1302.170, 1304.860, 1306.030

we fixed the surface gravity to the value obtained from the optical data, and then determined the temperature from a fit to the ultraviolet COS spectra. For this we used the slope between the optical photometry and the absolutely calibrated COS spectra as additional constraint.

The best fit atmospheric parameters were then used to create synthetic spectra containing approximately 14 000 spectral lines from 14 elements.The atmospheric metal abundances were varied until a good fit was obtained between the synthetic spectra and the observed absorption lines. Adjusting the abundances by ± 0.2 dex around the best fit values allowed an estimate of the abundance uncertainties. The uncertainty in the atmospheric parameters has only a small effect on the element abundances (<0.04 dex). Table 5.2 lists the absorption lines used to determine the carbon and oxygen abundances. The oxygen abundances are primarily measured from the O I 1152.15 Å line. The O I lines around 1300 Å are affected by geocoronal emission in several of the spectra, which is not corrected for by the COS pipeline. Where no geocoronal emission is present, these lines are still affected by blending with Si II and interstellar O I lines, but still provide (less accurate) abundance determinations which agree with measurements from the O I 1152.15 Å line.

As the metals diffuse out of the white dwarf atmosphere on different time scales, the element abundances in the white dwarf photosphere do not necessarily match those of the debris material. The diffusion time scales were calculated using the same atmospheric models as for the spectral fitting (Koester, 2009). As the diffusion time scales for these hydrogen atmosphere white dwarfs are of order days to, at most, months, it is reasonable to assume that the white dwarfs are currently accreting, and accretion and diffusion are in equilibrium. The accretion rate is therefore the ratio of the atmospheric abundance to the diffusion time scale. Radiative levitation, which can change the diffusion time scales or even keep an element in the atmosphere without ongoing accretion (Chayer & Dupuis, 2010b), is taken into account when calculating the diffusion time scales, but has a negligible effect on carbon and no effect on oxygen over the temperature range of our sample. Finally, the C/O ratio by number is calculated as the ratio of the accretion rates, weighted by the relative atomic masses.

Analysis of the debris in four of these white dwarfs were presented in Gänsicke et al. (2012), but the abundances used here have been updated with new calculations. Ultraviolet spectra of the remaining six white dwarfs are shown in Figure 5.1, featuring photospheric

absorption lines from a variety of metals, including both carbon and oxygen (Figure 5.2).

In addition to these new measurements, we have assembled all published abundances for carbon and oxygen at white dwarfs both observed with COS and analysed with the same model described above (Wilson et al., 2015; Xu et al., 2014; Farihi et al., 2013a; Xu et al., 2013). These criteria create a homogeneous sample, which avoids systematic uncertainties that may result from comparing different data sources and models. Where more than one measurement is available we use the most recent result, and we adopt the most commonly used white dwarf designations. In total, we discuss C/O measurements for debris in eleven systems and firm upper limits for another five.

Four of the white dwarfs in our sample have helium dominated atmospheres, labelled in Fig 5.3 and Table 5.3. These stars develop deep convective envelopes, which may lead to dredge-up of core-carbon into the atmosphere. Dredge-up typically occurs in cool ($T_{\rm eff} \lesssim 12\,000$ K) white dwarfs, but it has been suggested that a small number of white dwarfs may have helium envelopes thin enough to pollute the atmosphere with core-carbon even at higher temperatures (see Chapter 4 for a full discussion). Thus, although we treat the C/O ratios in helium atmosphere white dwarfs as firm detections, this caveat should be kept in mind when discussing the planetary abundances at individual white dwarfs. The majority of our sample (12 out of 16) have hydrogen atmospheres, which are unaffected by dredge up.

5.2 Discussion

Figure 5.3 and Table 5.3 show the C/O ratios of the planetesimal debris at the 16 systems in our sample as a function of effective temperature (and therefore the age since white dwarf formation). We compare these ratios with those for the CI chondritic meteorites (Lodders & Fegley, 2011), bulk Earth (Allègre et al., 2001; Marty, 2012), Comet Halley (Lodders & Fegley, 1998), and the Solar photosphere (von Steiger & Zurbuchen, 2016). As carbon chemistry is thought to become an important factor in protoplanetary discs with C/O > 0.8 ($\log({\rm C/O}) > -0.097$), we take this as a lower limit for a planetesimal formed in a carbon-rich environment. We note, however, that planets formed in such discs are predicted to potentially have C/O $\gg$ 1.0 (Bond et al., 2010).

We find no planetary debris with C/O > 0.8. The debris at WD 2058+181 has the highest ratio, with $\log({\rm C/O}) = -0.57 \pm 0.28$, still below the Solar value. Applying binomial statistics, we find that planetesimals with C/O > 0.8 occur in < 17 percent of systems at a $2\,\sigma$ confidence level, falling to < 6.5 percent with $1\,\sigma$ confidence. Our upper limit on high planetary C/O is consistent with that found in stellar abundances by Fortney (2012), who showed that the fraction of stars with C/O > 0.8 is no more than 10–15 percent. None of the

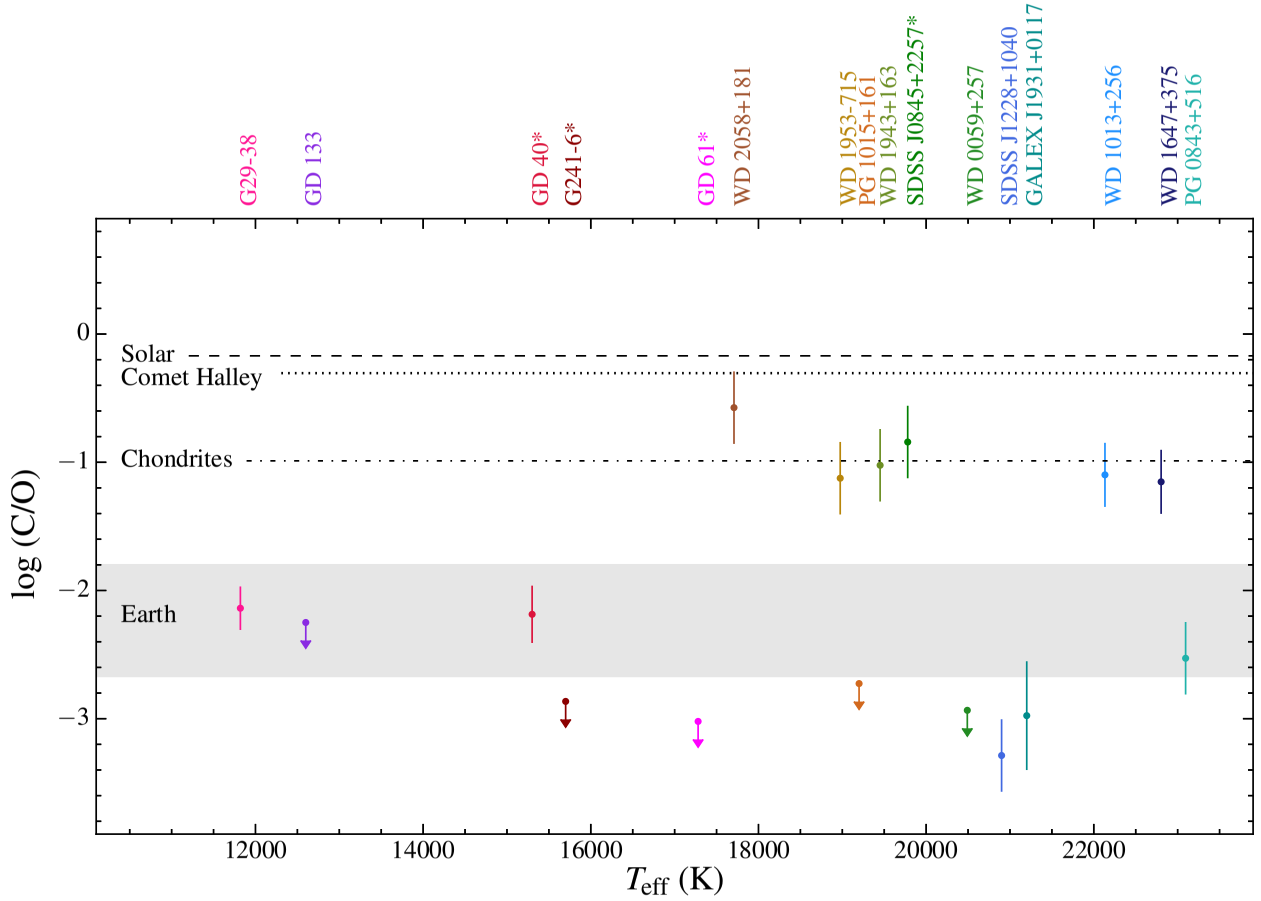

Figure 5.3: C/O number ratios of the planetesimal debris in our sample, plotted against the effective temperature ($T_{\rm eff}$) of the host white dwarfs and compared with various Solar System bodies. The colour scheme is intended to aid identification and has no physical significance. White dwarfs with helium atmospheres, which may be affected by convective carbon dredge-up that could enhance their carbon abundances (Sect. 5.1), are marked with *. Objects with similar temperatures have been offset slightly for clarity. The shaded area shows the range of values present in the literature for Earth's C/O (Section 5.2).

planetesimal debris in the 16 systems has C/O similar to that of Comet Halley ($\log(\mathrm{C/O}) = -0.04$), supporting the conclusions of Veras et al. (2014c) that comets are not a significant population of parent bodies for the debris detected at many white dwarfs. There are no observed trends in C/O with the post-main sequence (cooling) age.

Although none of the systems are carbon-rich, the material does appear to fall into two distinct populations, with an apparent gap between $\log(\mathrm{C/O}) \approx -1$ and $\log(\mathrm{C/O}) \lesssim -2$. Six systems have relatively high C/O ratios, with $\log(<\mathrm{C/O}>) = 0.12 \pm 0.07$ (where the error is the 1σ spread). This is consistent with the CI chondrite meteorites (Lodders & Fegley, 2011), which are thought to be representative of the primordial composition of the rocky Solar System. It is likely that the debris in these systems originated as small asteroids, which had not undergone significant post-nebula differentiation .

The remaining ten systems all have C/O less than or equal to that of the bulk Earth. Comparing the relative abundances of carbon and oxygen in this group with the other elements detected in their debris shows that they have a high oxygen abundance (relative to, for example, Si), rather than being relatively poor in carbon. A speculative explanation for this is that the parent bodies of the debris contained a significant amount of water, similar to Ceres or the large moons of the gas giants. High mass fractions of water have already been detected in debris at GD 61 (Farihi et al., 2013a), which has an upper limit on its C/O ratio placing it in the low C/O group. Addition of water to a planetesimal with an otherwise Earth-like composition would increase the abundance of oxygen, but leave the carbon abundance unchanged, decreasing the C/O ratio. A potential caveat to this argument is the study by Jura & Xu (2012) of hydrogen in helium atmosphere white dwarfs in the 80 pc sample. Their results suggested that water makes up less that one percent of the mass accreting onto the white dwarfs in their sample. However, both the amount and origin of hydrogen in helium atmosphere white dwarfs, and its relevance to debris accretion, are subject to ongoing discussion (Koester & Kepler, 2015; Bergeron et al., 2011).

Additionally, the carbon content of the Earth, and in particular the core, is still subject to discussion. Allègre et al. (2001) find a mass fraction of 0.17–0.36 percent, resulting in a log (C/O) between -1.8 and -2.16. In contrast, Marty (2012) instead calculate a carbon mass fraction of only 0.053 percent. Using the oxygen fraction from Allègre et al. (2001), this lowers the $\log(\mathrm{C/O})$ to -2.7, consistent with the average of the low C/O systems ($\log(<\mathrm{C/O}>) = -2.5 \pm 0.36$). The range of proposed C/O ratios for Earth is shown by the shaded area in Figure 5.3.

By providing a strong lower limit of the occurrence of carbon-rich planetesimals, we show that debris-polluted white dwarfs are likely the most powerful diagnostics of carbon chemistry in extrasolar planetesimals. Increasing the sample size will provide stronger constraints on the existence, or lack thereof, of carbon planets. More generally, abundance

Table 5.3: C/O ratios by number shown in Figure 5.3, in order of increasing C/O. White dwarfs with helium atmospheres are marked with *. References: 1. This work; 2. Xu et al. (2013); 3. Farihi et al. (2013a); 4. Xu et al. (2014); 5. Wilson et al. (2015).

Name	log (C/O)	Ref.
SDSS J1228+1040	-3.3 ± 0.28	1
GD 61*	≤ -3.0	3
GALEX J1931+0117	-3.0 ± 0.42	1
WD 0059+257	≤ -2.9	1
G241-6*	≤ -2.9	2
PG 1015+161	≤ -2.7	1
PG 0843+516	-2.5 ± 0.28	1
GD 13	≤ -2.2	4
GD 40*	-2.2 ± 0.22	2
G29-38	-2.1 ± 0.17	4
WD 1647+375	-1.2 ± 0.25	1
WD 1013+256	-1.1 ± 0.25	1
WD 1953-715	-1.1 ± 0.28	1
WD 1943+163	-1.0 ± 0.28	1
SDSS J0845+2257*	-0.84 ± 0.28	5
WD 2058+181	-0.57 ± 0.28	1

studies of the debris at white dwarfs are sensitive to a wide variety of elements, making them the ideal tool to systematically investigate the full range of non-gaseous planetary chemistry.

Chapter 6

Multi-wavelength observations of the EUV variable metal-rich white dwarf GD 394

"People of Earth, your attention, please. This is Prostetnic Vogon Jeltz of the Galactic Hyperspace Planning Council. As you will no doubt be aware, the plans for development of the outlying regions of the Galaxy require the building of a hyperspatial express route through your star system. And regrettably, your planet is one of those scheduled for demolition. The process will take slightly less than two of your Earth minutes. Thank you."

Douglas Adams, The Hitchhiker's Guide to the Galaxy

Based on a submitted paper on which I am lead author, using data from a Hubble Space Telescope *program of which I am PI, Program ID 13719. Boris Gänsicke and Jay Holburg contributed to the analysis, and Detlev Koester and Simon Preval provided model atmospheres. Additional observations and analysis were provided and/or carried out by Jay Farihi, P. Wilson Cauley, Claudia Belardi, Knox Long, Paul Chote, Mark Hollands, Seth Redfield, Matt Burleigh, Martin Barstow and Sarah Casewell.*

Of the hundreds of known remnant planetary systems at white dwarfs, short time-scale variability has been observed at only a handful. Along with the transits at WD 1145+017 (Vanderburg et al., 2015; Gänsicke et al., 2016; Redfield et al., 2017), examples include the rapid drop in infrared flux from WD J0959–0200 (Xu & Jura, 2014), the growth and subsequent disappearance of gaseous emission from SDSS J1617+1620 over an eight year period (Wilson et al., 2014) and the year-to-year changes in gaseous emission line profiles at several other white dwarfs (Wilson et al., 2015; Manser et al., 2016b,a).

The first[1] metal-rich, single white dwarf where variability was observed was the hot and relatively bright ($V_{\rm mag}$ = 13.09) white dwarf GD 394 (WD 2111+489). Chayer et al. (2000) and Vennes et al. (2006) measured near-Solar abundances of Fe in GD 394's hydrogen atmosphere, along with high Si and P abundances. White dwarfs with $T_{\rm eff}$ $\gtrsim$20000 K may retain some metals in their atmospheres via radiative levitation, where outward-directed photons transfer momentum to metals and counteract the effects of downward diffusion (Chayer & Dupuis, 2010a; Chayer, 2014). However, radiative levitation is predicted to support only small amounts of Fe (Chayer et al., 1995a; Schuh et al., 2002), and cannot explain the Fe abundances of GD 394 (Dupuis et al., 2000). Although the radiative support for Si is stronger, Barstow et al. (1996) showed that the Si abundance of GD 394 similarly exceeds the predictions. The timescales for metals to diffuse out of the photospheres of hot white dwarfs are of order days (Paquette et al., 1986; Koester & Wilken, 2006; Koester, 2009), so for the metal abundances to be higher than those supported by radiative levitation GD 394 must be currently, and continuously, accreting material from an external source.

Most remarkably, Dupuis et al. (2000) detected a 1.15 d periodic modulation in the extreme-ultraviolet (EUV) flux of GD 394, with an amplitude of 25 per cent. The variability was detected in three separate instruments onboard the *Extreme Ultraviolet Explorer* (*EUVE*) in observations spanning 1992–1996, leading Dupuis et al. (2000) to conclude that it was intrinsic to the star. Their preferred explanation for this variability was that the accreting material is being channelled, presumably by a magnetic field, onto a spot, which is rotating in and out of view over the white dwarf rotation period. Any changes in Si

[1] With the exception of pulsating objects, where the variability is inherent to the white dwarf rather than produced by external material.

concentration would affect the atmospheric opacity in the EUV, resulting in the observed variability. This is similar to the explanation for the soft X-ray variable V471 Tau, where material from a K dwarf is magnetically funnelled onto a white dwarf companion (Jensen et al., 1986; Clemens et al., 1992). No subsequent observations of GD 394 have detected variability at other wavelengths.

The observations of GD 394 published so far mostly took place before the development of the research field of remnant planetary systems at white dwarfs, and as such planetesimal debris was not considered as a possible source for the detected metals. Initially radial velocity measurements suggested that the metals were in a cloud around the white dwarf (Shipman et al., 1995), but later, more precise radial velocity measurements were consistent with a photospheric origin of the metals (Barstow et al., 1996; Bannister et al., 2003). Dupuis et al. (2000) favoured accretion either from the Interstellar Medium (ISM), pointing out that there is a high-density ISM clump nearby (Sfeir et al., 1999), or from an undetected companion. Both of these sources can be ruled out: accretion from either source would have a large mass fraction of carbon, which is not detected in GD 394 (Dickinson et al., 2012), and no evidence for a stellar mass companion has been observed either from radial velocity measurements (Saffer et al., 1998) or via searches for an infrared excess (Mullally et al., 2007). As accretion of planetary debris is now thought to be responsible for most, if not all, metal pollution in single white dwarfs, it is likely to also be the source of the metals at GD 394.

Here we test the hypothesis that the EUV variation is caused by an accretion spot in two ways: Firstly, phase-resolved spectroscopy should show changes in metal line strength as the spot moves in and out of view; secondly, flux redistribution from the spot should manifest as optical variability in anti-phase to the EUV variation (Dupuis et al., 2000).

The paper is arranged as follows: In Section 6.1 we describe the observations of GD 394, followed by Section 6.2 where we discuss their implications for the short- and long-term variability of GD 394. In Section 6.3 we use model atmosphere fits to the spectroscopy to measure the atmospheric parameters and metal abundances in the star. Section 6.4 presents EUV models to further test the accretion spot hypothesis, and Section 6.5 updates the search for gaseous emission from a circumstellar disc. Finally we discuss our results in Section 6.6 and conclude in Section 6.7.

6.1 Observations

We have obtained multiple new observations of GD 394, which, combined with archival data, allows us to search for both spectroscopic and photometric variability over a range of wavebands and timescales. Figure 6.1 shows the spectral energy distribution of GD 394. A

Table 6.1: Summary of the spectroscopic observations of GD 394. For the STIS-FUV observations we give the phase position in a 1.15 d period, with the start of the first observation defining phase zero.

Date	Telescope/Instrument	Start Time (UT)	Total Exposure Time (s)	Phase	Wavelength range (Å)
2016 August 13	WHT/ISIS	23 : 24 : 00	1800	-	3056–5409, 5772–9088
2015 November 15	Keck/HIRES	04 : 38 : 13	900	-	3125–5997
2015 August 25	*HST*/STIS	16 : 43 : 59	2595	4.3	1160–1710
2015 August 24	*HST*/STIS	20 : 01 : 05	2595	3.5	1160–1710
2015 August 24	*HST*/STIS	09 : 02 : 39	2595	3.1	1160–1710
2015 August 23	*HST*/STIS	12 : 20 : 34	2595	2.4	1160–1710
2015 August 22	*HST*/STIS	15 : 38 : 36	2595	1.6	1160–1710
2015 August 21	*HST*/STIS	18 : 56 : 37	2595	0.9	1160–1710
2015 August 21	*HST*/STIS	15 : 45 : 25	2595	0.8	1160–1710
2015 August 20	*HST*/STIS	19 : 05 : 13	2595	0.0	1160–1710
2013 December 23	*HST*/STIS	10 : 58 : 53	1500	-	2577–2835
2009 May 23	Keck/HIRES	14 : 40 : 12	1800	-	3125–5997, 4457–7655
2007 August 06	WHT/ISIS	00 : 32 : 00	2882	-	4520–5262, 8260–9014
2002 October 27	*FUSE*	16 : 44 : 22	4403	-	905–1181
2002 September 04	*FUSE*	05 : 18 : 54	7957	-	905–1181
2000 September 09	*FUSE*	19 : 51 : 31	4155	-	905–1181
2000 June 21	*FUSE*	14 : 03 : 44	3327	-	905–1181
2000 June 20	*FUSE*	18 : 04 : 49	28310	-	905–1181
1999 October 11	*FUSE*	04 : 29 : 36	3662	-	905–1181
1999 October 11	*FUSE*	10 : 33 : 29	5652	-	905–1181
1999 October 13	*FUSE*	11 : 00 : 21	4688	-	905–1120
1992 June 18	*HST*/GHRS	07 : 30 : 19	653	-	1196–1232
1992 June 18	*HST*/GHRS	08 : 32 : 47	490	-	1290–1325
1992 June 18	*HST*/GHRS	08 : 44 : 29	1088	-	1383–1418

Table 6.2: Equivalent widths of the lines shown in Figure 6.2 across all eight *HST* visits.

		Equivalent Width (mÅ)							
Line	Rest λ (Å)	Visit 1	Visit 2	Visit 3	Visit 4	Visit 5	Visit 6	Visit 7	Visit 8
Si III	1294.54	77.0 ± 7.8	86.0 ± 7.7	79.0 ± 7.6	83.0 ± 7.7	80.0 ± 7.7	79.0 ± 7.8	82.0 ± 7.1	78.0 ± 7.8
Si III	1296.73	77.0 ± 7.6	79.0 ± 8.0	76.0 ± 7.5	79.0 ± 7.7	78.0 ± 7.3	80.0 ± 7.9	77.0 ± 7.2	77.0 ± 8.1
Si III	1298.89	150 ± 11	150 ± 12	150 ± 12	150 ± 12	160 ± 13	150 ± 12	150 ± 12	150 ± 12
Si III	1301.15	76.0 ± 7.1	71.0 ± 7.1	74.0 ± 7.1	81.0 ± 7.6	75.0 ± 7.4	77.0 ± 7.1	79.0 ± 7.3	72.0 ± 7.2
Si III	1303.32	77.0 ± 6.9	80.0 ± 7.3	78.0 ± 7.5	75.0 ± 7.4	81.0 ± 7.8	75.0 ± 7.4	80.0 ± 7.2	72.0 ± 7.1
Si III	1312.59	47.0 ± 6.4	43.0 ± 6.1	45.0 ± 6.9	43.0 ± 6.5	45.0 ± 6.0	46.0 ± 6.7	47.0 ± 6.1	48.0 ± 6.4

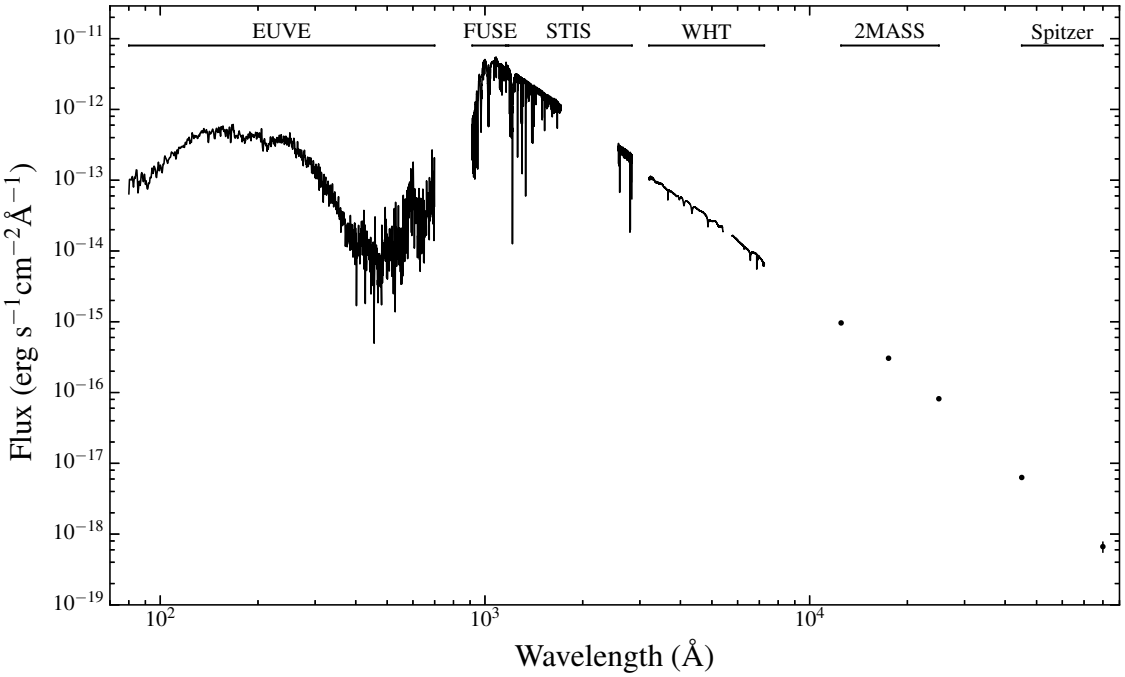

Figure 6.1: Full spectral energy distribution of GD 394 from the extreme ultraviolet to mid-infrared. The 2MASS and *Spitzer* data are taken from Mullally et al. (2007).

full list of all detected metal absorption lines is given in Appendix A.

6.1.1 Spectroscopy

STIS-FUV

To test the accretion spot hypothesis, we obtained eight FUV spectra of GD 394 using the Space Telescope Imaging Spectrograph onboard the *Hubble Space Telescope* (*HST*/STIS). The observations were taken between 2015 August 20-21, timed to fully sample the 1.15 day period seen in the EUV. A summary of the FUV observations is given in Table 6.1, including their phase positions relative to the start of the first observation based on the 1.15 day EUV period. The observations were taken with the FUV-MAMA detector in TIME-TAG mode, using the E140M grating covering the wavelength range 1144–1710Å with an average resolution of $\lambda/91700$ per pixel. The spectra were heavily affected by echelle ripple, so were recalibrated using CalSTIS with an updated Photometric Conversion Table (PHT) file provided by the STIS instrument team (T. Monroe, private communication). Figure 6.2 shows an example section of the spectra.

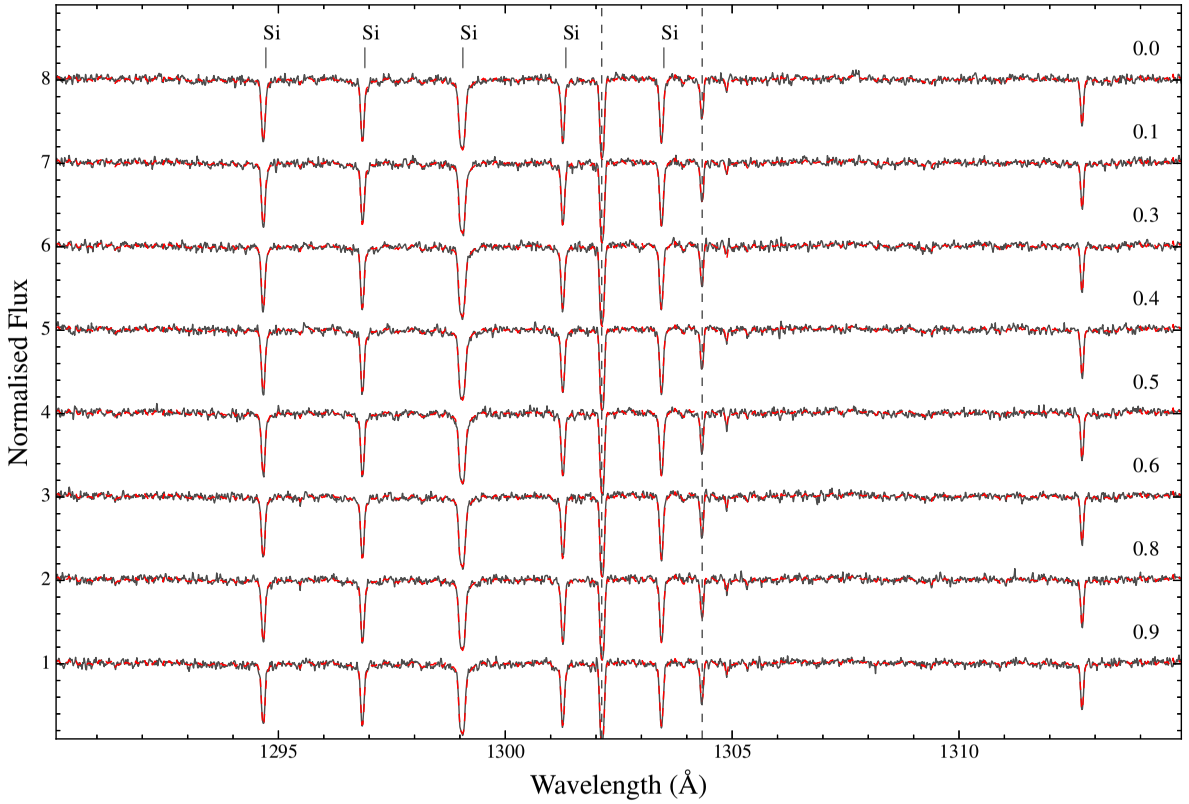

Figure 6.2: Phase-resolved *HST*/STIS spectra of GD 394 showing Si III lines around 1300Å. The phase-folded position in a 1.15 d period, with the start of the first observation defining phase zero, is shown on the right. The coadded spectrum is over-plotted in red, demonstrating the complete lack of variability between the observations. Interstellar O I lines are indicated by the grey dashed lines.

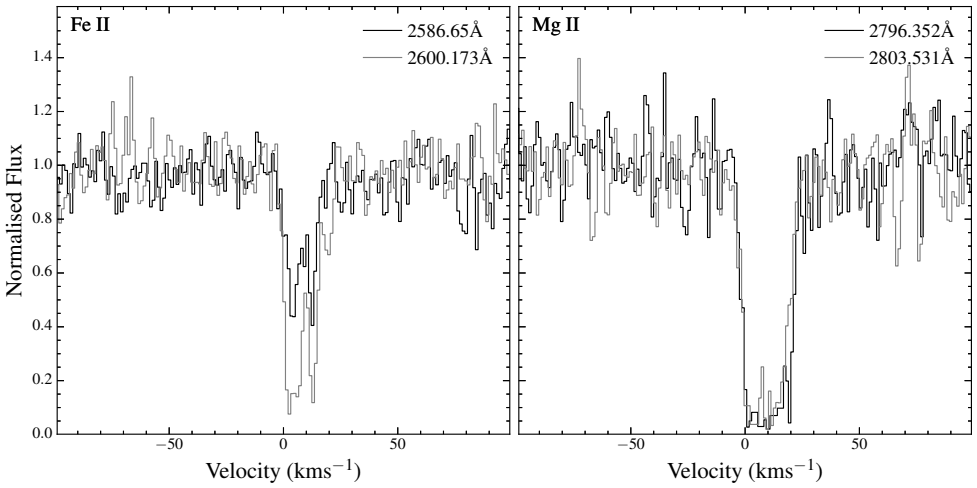

Figure 6.3: STIS near-ultraviolet (NUV) observations of interstellar lines of Fe II andMg II along the line of sight towards GD 394 shown in velocity space.

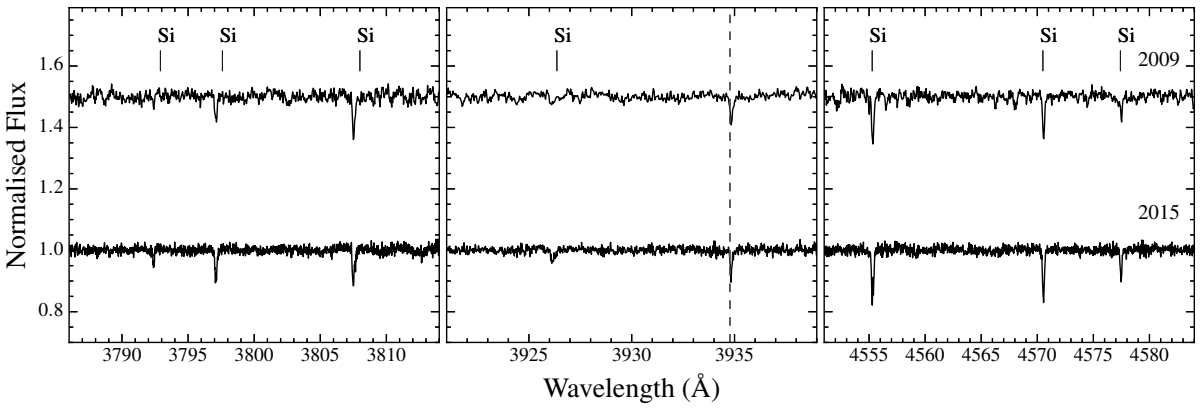

Figure 6.4: Keck/HIRES spectra of GD 394 containing Si III absorption lines, with no change in strength between the two observations. The interstellar Ca K absorption is marked by the dashed line.

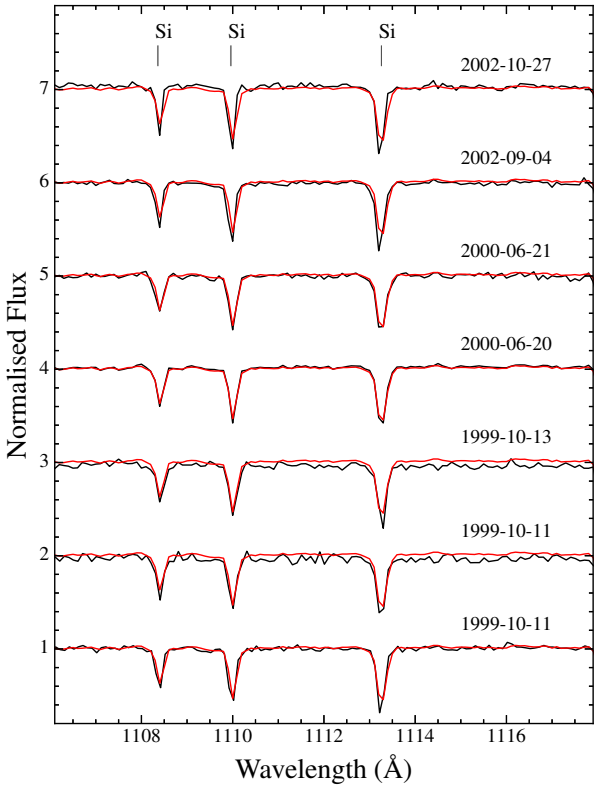

Figure 6.5: Section of time-series *FUSE* spectra of GD 394 compared with a coadd (red), showing no change in absorption line strength.

STIS-NUV

GD 394 was also observed by STIS in near-ultraviolet (NUV) as part of Program ID 13332. A spectrum was obtained on 2013 December 23, which used the E230H grating to cover a wavelength range of 2577–2835 Å with a average resolution of $\lambda/228,000$ per pixel. The spectrum only has S/N $\approx$ 6 but clearly shows several ISM Mg II and Fe II absorption lines blue-shifted by $\approx 10\mathrm{km\,s^{-1}}$ (Figure 6.3).

HIRES

Optical spectroscopy was obtained on 2009 May 23–24 and 2015 November 15 using the High Resolution Echelle Spectrometer (HIRES) on the 10 m W. M. Keck Telescope (Vogt et al., 1994) under Program IDs A284Hr, A284Hb and N116Hb. On both nights 3×300 s exposures were taken covering the wavelength range 3125–5997 Å. On the first night an additional 3×300 s exposures were taken covering the wavelength range 4457–7655 Å using the GG475 filter. All of the exposures used the C5 aperture. The HIRES data were reduced using the REDUX pipeline[2]. Standard data reduction steps were performed including flat fielding, bias subtraction, and two-dimensional wavelength solutions produced from Th-Ar comparison exposures. The spectra were optimally extracted, with hot pixels removed using a median comparison between the individual exposures. Continuum normalization was done using low-order polynomials and ignoring any absorption lines. Spectra from adjacent orders were averaged in overlap regions, and the individual exposures at each epoch were coadded using a signal-to-noise weighted average.

The spectra contain multiple absorption lines from Si (Figure 6.4). The equivalent widths of the absorption lines are the same to within one sigma between the two epochs, so the spectra were coadded to produce a single S/N$\approx$ 140 spectrum.

WHT

Further optical spectroscopy of GD 394 was obtained using the Intermediate dispersion Spectrograph and Imaging System (ISIS) on the 4.2 m William Herschel Telescope (WHT) on 2007 August 6 and 2016 August 13. The 2007 observation used the R1200 grating to cover the wavelength ranges 4520–5262 Å and 8260–9014 Å, with a total exposure time of 2882 s. The 2016 observations used the R600B+R gratings covering 3056–5409Å and 5772–9088 Å with a total exposure time of 1800 s. The raw WHT data were reduced with standard spectroscopic techniques using STARLINK software. Debiasing, flat fielding, sky-subtraction, and optimal extraction were performed using the PAMELA package. MOLLY was

[2] http://www.ucolick.org/~xavier/HIRedux/

used for wavelength and flux calibration of the 1-D spectra [3]. No metal absorption lines are detected in either spectrum, as the 2007 observation did not cover the appropriate wavelength ranges and the 2016 observation has insufficient spectral resolution.

6.1.2 Archival data

In addition to the new observations described above, we retrieved several archival datasets.

GD 394 was observed by the *Far Ultraviolet Spectroscopic Explorer* (*FUSE*) spacecraft on eight occasions between 1999 October 11 and 2002 October 27, covering the wavelength range 925–1180 Å in the FUV. The data were retrieved from the MAST archive and recalibrated using CalFUSE v3.2.3. The spectra from the four separate channels in the *FUSE* instrument were renormalised to the guiding channel and combined.

GD 394 was observed with the *Extreme Ultraviolet Explorer* (*EUVE*) six times between 1993 September 13 and 1995 October 13. We retrieved and reduced the data as described in Barstow et al. (1996) and coadded the data into a single spectrum.

Shipman et al. (1995) used the Goddard High Resolution Spectrograph(GHRS), one of the first-light instruments on *HST*, to observe GD 394 on 1992 June 18. Spectra were taken of three sections of the FUV: Lyman α, the Si II lines around 1300 Å, and the Si IV 1392 Å and 1402 Å doublet, areas which are also covered by our STIS FUV spectrum. The data were retrieved from the MAST database.

GD 394 was also observed multiple times by the *International Ultraviolet Explorer* (*IUE*) in both high and low resolution mode. A full description and analysis of the high-resolution *IUE* spectra is presented in Holberg et al. (1998).

Finally, we retrieved an optical spectrum obtained by Gianninas et al. (2011) from the Montreal White Dwarf Database (MWDD, Dufour et al., 2017) covering the wavelength range 3780–5280Å which we used as a cross check for our fit to the WHT spectra.

6.1.3 Photometric observations

SuperWASP

GD 394 was observed by the Wide-Angle Search for Planets (SuperWASP) on multiple occasions between 2006 November and 2008 August (Faedi et al., 2011). 3506 30 s exposures were taken with a median S/N= 7.5. The data were retrieved from the WASP archive and calibrated using the standard routines described in Pollacco et al. (2006).

[3] PAMELA and MOLLY were written by T. R. Marsh and can be obtained from `http://www.warwick.ac.uk/go/trmarsh`.

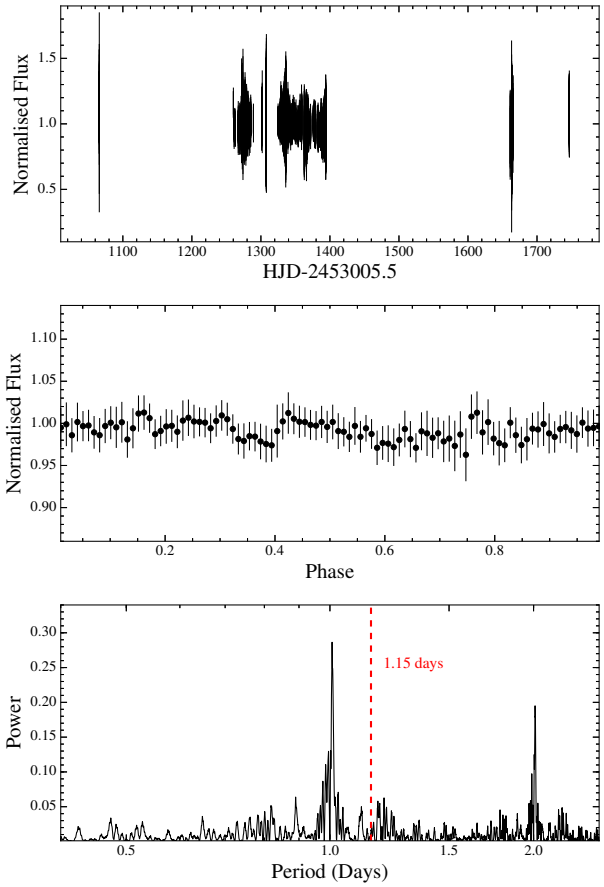

Figure 6.6: Observations of GD 394 made by SuperWASP. Top: coverage of observations between 2006 November and 2008 July. Middle: SuperWASP data binned to 1000 s and folded on a 1.15 d period. Bottom: Lomb-Scargle periodogram, showing no significant peaks apart from a 24 hour alias. No evidence for a 1.15 d periodic variation is seen in either the folded lightcurve or the periodogram.

.

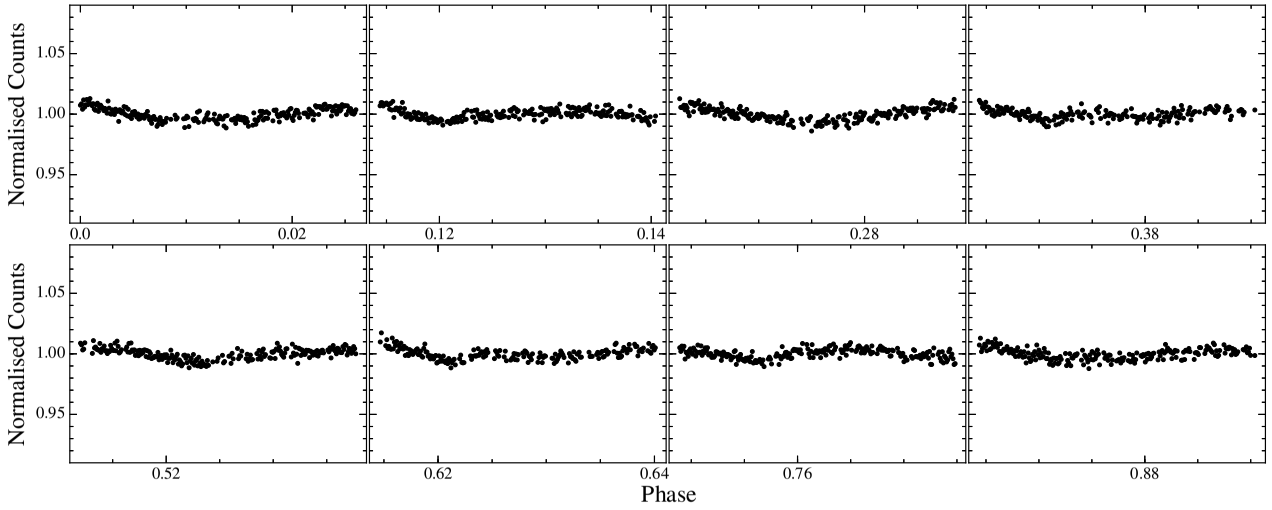

Figure 6.7: FUV lightcurves extracted from the the STIS TIME-TAG event files into 10 s bins and folded onto a 1.15 d period. Flux dropouts due to telescope jitter have been removed and a linear fit subtracted to account for focus variations over each *HST* orbit. Although the lightcurve is still dominated by systematics, the 1.15 d fluctuation seen in the EUV lightcurve is not observed.

W1m

Additional photometry was obtained using the Warwick 1m telescope (W1m) telescope at the Roque de Los Muchachos Observatory on La Palma on 2016 May 14 and 2016 May 16. The telescope has a dual beam camera system with fixed visual and Z band filters and was operated in engineering mode. A cadence of 13 s was achieved using 10 s exposures and a 3 s readout time. Total time on target was 2990 s and 7970 s on the two nights respectively, covering 11 per cent of the 1.15 d EUV period.

Ultraviolet photometry

Finally, both the STIS and *FUSE* spectroscopic observations were obtained using photon-counters, allowing high-cadence lightcurves to be obtained (see for e.g. Wilson et al., 2015; Sandhaus et al., 2016).

The STIS light curve was extracted from the TIME-TAG event files with events from the edge of the detector and around the Lyman α line removed. The echelle spectrum covers most of the detector and GD 394 is relativity bright, so no background subtraction was necessary. Each lightcurve contains multiple irregular flux dropouts of approximately one second. Comparison with the jit files, which record the precise spacecraft pointing during the exposure, showed that each dropout was accompanied by a sharp spike in pointing declination. All times associated with spikes in declination were therefore masked out, regardless of whether flux dropouts were seen.

Furthermore, each lightcurve is dominated by a semi-linear increase in flux over the exposure of $\simeq$ 5 per cent. As this trend is seen in every observation, regardless of phase position within the 1.15 day EUV period of GD 394, it is likely instrumental in origin, probably a result of the telescope focus position varying throughout each *HST* orbit.

The focus position is not recorded, but can be modelled for the imaging instruments[4]. As no focus model is available for STIS, we cannot accurately detrend the data. We obtained focus models for WFC3/UVIS2 and ACS/WFC2 for our observation times. The focus position moved linearly in the same direction in each observation, consistent with having caused the linear increase in flux observed. Dividing by a linear fit removes most of the trend, but still leaves variations in flux that preclude an accurate measurement of variability below the $\approx$ 1 per cent level. The partially detrended lightcurves are shown in Fig 6.7, folded onto a 1.15 d period. The total exposure time covers $\approx$ 20 per cent of this period.

Light-curves from the *FUSE* observations were extracted in a similar fashion, pro-

[4] `http://www.stsci.edu/institute/org/telescopes/Reports/ISR-TEL-2011-01.pdf`, `http://www.stsci.edu/hst/observatory/focus/FocusModel`

viding a useful link between the STIS FUV and *EUVE* observations (Figure 6.1). Unfortunately the observations are affected by aperture drift caused by thermal distortion, so absolute photometry is impossible and we cannot compare between observations. Nevertheless, each individual light-curve is constant, with no evidence for flux variations similar to those detected in the EUV.

6.2 Non-detection of variability

6.2.1 Short-term

Figure 6.2 shows sections of all eight FUV spectra, compared with the coadded spectrum. The spectra show no significant changes in the strength, shape or velocity of the absorption lines. Equivalent widths for all identifiable lines were measured via the formalism given by Vollmann & Eversberg (2006), all of which were constant to within one sigma. The equivalent widths of the lines shown in Figure 6.2 are given in Table 6.2. We thus detect no evidence for an accretion spot in the FUV.

The *FUSE* spectra also show no signs of variability. By coincidence, the *FUSE* observations sample the 1.15 d EUV period fairly evenly, although their spacing in time is too large to accurately map their phase position. Therefore, they also provide no evidence for an accretion spot, although they are a weaker constraint compared to the STIS observations.

The second consequence of the accretion spot hypothesis put forward by Dupuis et al. (2000) is that GD 394 should undergo a periodic variation in optical flux, in anti-phase with the EUV variation, due to flux redistribution. Figure 6.6 shows our SuperWASP lightcurve folded onto the 1.15 d EUV period, along with a Lomb-Scargle periodogram. No significant variation is seen in the lightcurve, and the periodogram does not return a 1.15 d period. Neither do the W1m or UV lightcurves show any variation consistent with a 1.15 d period. This strengthens the conclusion drawn from the lack of spectral variation that the spot hypothesis is incorrect. Additionally, no evidence for transiting debris like that at WD 1145+017 (Vanderburg et al., 2015) is detected in any of the available photometry.

We also searched our STIS spectra for radial velocity variations that could reveal a substellar companion. Saffer et al. (1998) observed GD 394 as part of a search for double-degenerate Type 1A supernova progenitors, finding that the radial velocity remained constant to a precision of $\simeq 30 - 40\,\mathrm{km\,s^{-1}}$. We improve on this precision by simultaneously fitting to the five close Si lines around 1300 Å and find that the radial velocity of GD 394 is constant to a precision of $\approx 0.75\,\mathrm{km\,s^{-1}}$, ruling out an unseen companion with $M \sin i > 8\,M_{\mathrm{Jup}}$ in a 1.15 day orbit.

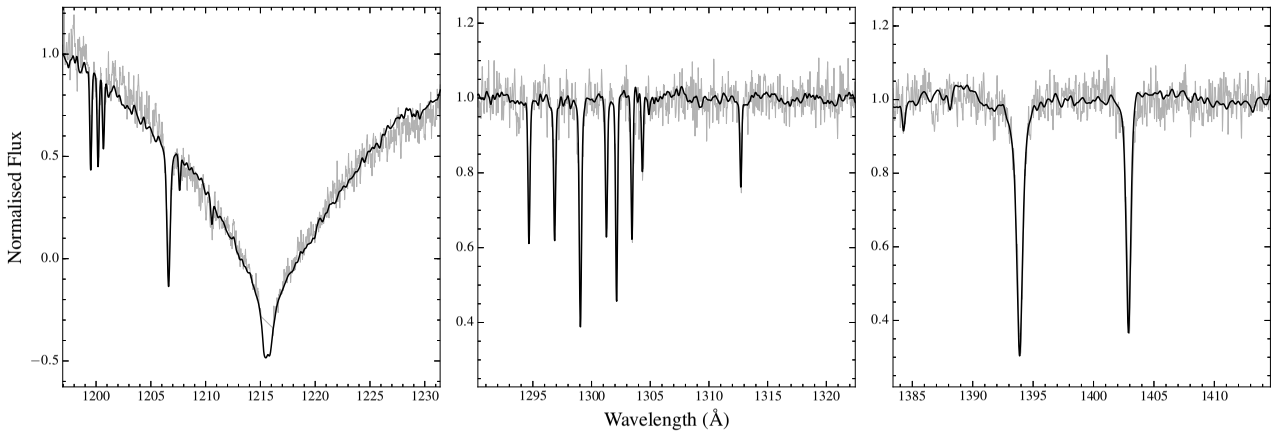

Figure 6.8: Comparison of the 1992 GHRS (grey) and 2015 STIS (black) FUV spectra.

Table 6.3: Equivalent widths of absorption lines detected in the GHRS spectra compared with the coadded STIS spectrum.

		Equivalent Width (mÅ)	
Line	Rest λ (Å)	GHRS (1992)	STIS (2015)
Si II	1206.520	270 ± 170	260 ± 68
Si III	1207.517	16 ± 35	33 ± 20
Si III	1294.545	71 ± 44	80 ± 4.5
Si III	1296.726	80 ± 58	75 ± 4.6
Si III	1298.892	150 ± 61	150 ± 7.3
Si III	1301.149	71 ± 42	72 ± 4.2
Si III	1303.323	100 ± 61	77 ± 4.1
Si III	1312.591	43 ± 42	44 ± 3.8
Si IV	1393.755	490 ± 130	490 ± 36
Si IV	1402.77	340 ± 100	310 ± 17

Table 6.4: Radial velocity of GD 394 over all available epochs, normalised to the ISM lines in the STIS FUV spectra.

Observation	Epoch	$V_{Photosphere}$	V_{ISM}	ΔV	$V_{Adjusted}$
SWP hi	1988.9 ± 6.6	28.9 ± 0.8	−6.18 ± 1.46	−2.88	26.02 ± 1.5
GHRS	1992.464	35.37 ± 2.81	−0.4 ± 3.18	−8.66	26.71 ± 2.3
Lick	1996.68	27.6 ± 1.3	-	-	27.6 ± 1.3
HIRES	2009.39	28.49 ± 1.3	−10.59 ± 1.2	1.53	30.02 ± 1.8
HIRES	2015.87	27.53 ± 1.2	−11.06 ± 0.88	2.00	29.53 ± 1.5
STIS	2015.64	27.66 ± 0.36	−9.06 ± 0.2	0.00	27.66 ± 0.36

6.2.2 Long-term

A comparison between the two epochs of FUV spectroscopy (STIS in 2015, GHRS in 1992), is shown in Figure 6.8. We find no differences between the two spectra, and the equivalent widths of the absorption lines detected by both instruments are identical to within 1 sigma (Table 6.3). As the GHRS spectrum was obtained within two years of the *EUVE* observations, it is reasonable to assume that the EUV variation was already present. The variation must therefore either still have been present when our STIS observations were obtained, or have stopped in such a way as to leave the FUV spectrum unchanged. The lack of change over a 23 year period joins the long term observations of several other accreting white dwarfs (Wilson et al., 2014; Manser et al., 2016b) where no changes in absorption line strength have been detected. Given that the metal diffusion timescales are much shorter than the time between observations, the accretion rates onto metal-polluted white dwarfs are remarkably stable.

We can also place upper limits on any possible long-term changes in the velocities

of the stellar features seen in GD 394. Between 1982 and 2015 various high-dispersion observations have been obtained, including: (1) IUE high dispersion spectra obtained between 1982 and 1994 (Holberg et al., 1998); (2) *HST*/GHRS spectra obtained in 1992 (Shipman et al., 1995); (3) Lick, Mt. Hamilton Observatory spectra in 1996 (Dupuis et al., 2000); (4) Keck/HIRES observations in 2009 and 2015 (this paper); and (5) *HST*/STIS data in 2015 (this paper). These various spectra, obtained in the vacuum ultraviolet and the optical, potentially have different wavelength scales and velocity zero points. By using interstellar lines as an invariant fiducial, we can place these observations on the velocity scale of the STIS data.

IUE High Resolution SWP Spectra: There were four observations obtained in 1982 May 05, 1984 April 15, 1994 January 03 and 1994 January 04, respectively. Because they were all obtained through the SWP large aperture they included wavelength offsets due to location of the stellar image in the slit. The process of coadding these spectra involved small wavelength displacements applied to each spectrum (see Holberg et al., 1998), which were used to coalign the observed stellar and interstellar lines in each spectrum to an arbitrary zero-point prior to coaddition. A detailed examination of this process shows that there were no relative displacements between ISM and stellar lines for the individual spectra above the 10 mÅ level, or approximately $\approx$ 2 km s^{-1}. Thus, we detect no evidence of velocity variations both prior to and during the time span when the *EUVE* 1.15 d variations were observed.

HST/GHRS Spectra: The three ultraviolet spectral bands of GD 394 observed by (Shipman et al., 1995) included both ISM and photosphere lines (Figure 6.8). Dupuis et al. (2000) re-measured the GHRS spectra noting that wavelength calibrations were not obtained for one of the grating settings. We also re-measured the GHRS spectra using the same software as used for the IUE spectra. We find photospheric and ISM velocities of 35.37 ± 2.81km s^{-1} and -0.40 ± 3.18km s^{-1} respectively.

Lick Mt. Hamilton Echelle: Dupuis et al. (2000) observed photospheric Si III features in GD 394 and report a velocity of 27.6 ± 1.3km s^{-1}. No interstellar lines were reported.

Keck/HIRES: Two Keck HIRES spectra (see Section 6.1) were obtained in 2009 and 2015. The photospheric Si III and interstellar Ca III lines from these observations are shown in Figure 6.4. Seven individual Si III lines were measured in the 2015 data but only five were measurable in the 2009 data. The interstellar Ca K line is measurable in both spectra, whilst the Ca H line is barely seen in the 2015 data and is not detected in the 2009 data).

HST/STIS: The photospheric and interstellar velocities presented here from this paper and represent averages from Tables A.1 and A.2.

In Table 6.4 we list the sources, dates and observed photospheric and ISM veloc-

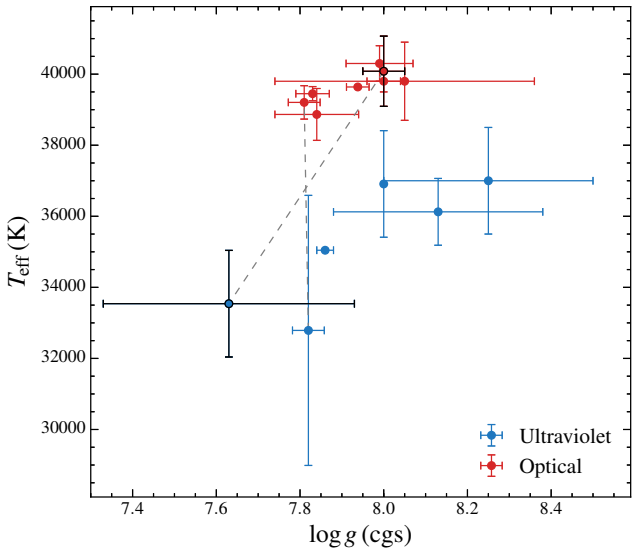

Figure 6.9: Literature determinations of the $T_{\rm eff}$ and $\log g$ of GD 394 as shown in Table 6.5, with the outlier from McMahan (1989) excluded. Multiple determinations from the same paper are joined with a dashed line, and the results from this work are outlined in black. The discrepancy between measurements based on ultraviolet and optical data is clear, as is the low $\log g$ we find from our STIS data.

ities, where available. Also listed are the velocity adjustments (ΔV) necessary to bring the observed ISM velocities to the observed $-9.06 \pm 0.20 \mathrm{km\,s^{-1}}$ ISM velocity of the STIS observations. The final column of Table 6.4 gives the adjusted photospheric velocity. As can be seen there is no evidence that the radial velocity of GD 394 has varied significantly between 1982 and 2015. However we cannot disentangle the radial velocity from the gravitational redshift of the white dwarf, as the range in $\log g$ between various model fits (see Section 6.3) results in gravitational redshifts spanning the range of $\sim 15 - 30\,\mathrm{km\,s^{-1}}$

6.3 Atmospheric parameters and metal abundances

Estimates from various papers in the literature of the atmospheric parameters of GD 394 are collected in Table 6.5 and displayed in Figure 6.9. Apparent in these results is a discrepancy between temperatures from optical and ultraviolet spectroscopy, with the latter being typically cooler by 4000 K (Lajoie & Bergeron, 2007).

6.3.1 STIS

Using the LTE model atmosphere codes described in Koester (2010), we started by fitting the *HST*/STIS spectra, coadding the eight observations into one spectrum with a signal-to-

Table 6.5: Atmospheric parameter determinations for GD 394 from the literature. References: 1. Holberg et al. (1986); 2. McMahan (1989); 3. Finley et al. (1990); 4. Kidder et al. (1991); 5. Vennes (1992); 6. Bergeron et al. (1992); 7. Barstow et al. (1996); 8. Marsh et al. (1997); 9. Vennes et al. (1997); 10. Finley et al. (1997); 11. Dupuis et al. (2000); 12 Lajoie & Bergeron (2007); 13. This work.

$T_{\rm eff}$ (K)	$\log g$ (cgs)	Data	Ref.
36125 ± 40	8.13 ± 0.25	Lyman α	1
44781 ± 366	8.27 ± 0.07	Balmer	2
36910 ± 1500		FUV	3
39800 ± 1100	8.05 ± 0.31	Lyman α/Balmer	4
37000 ± 1500	8.25 ± 0.25	EUV/Lyman α/FUV	5
39450 ± 200	7.83 ± 0.04	Balmer	6
40300 ± 500	7.99 ± 0.08	Lyman α /Balmer	7
38866 ± 730	7.84 ± 0.10	Balmer	8
39800 ± 300	8.00 ± 0.04	Balmer	9
39639 ± 40	7.938 ± 0.027	Balmer	10
35044 ± 25	7.86 ± 0.02	IUE/HUT/GHRS	11
39205 ± 470	7.81 ± 0.038	Balmer	12
32788 ± 3800	7.81 ± 0.038	UV (IUE)	12
34750 ± 2575	7.81 ± 0.038	UV/V	12
33540 ± 1500	7.63 ± 0.30	UV(STIS/FUSE)	13
40082 ± 988	8.00 ± 0.05	Balmer	13

Table 6.6: Characteristics of GD 394 for the different atmospheric parameters measured from ultraviolet and optical spectra, computed using the Montreal evolutionary tables (Holberg & Bergeron, 2006; Kowalski & Saumon, 2006; Tremblay et al., 2011b; Bergeron et al., 2011).

	Ultraviolet	Visible
$T_{\rm eff}$ (K)	33540 ± 1500	40082 ± 988
$\log g$ (cgs)	7.63 ± 0.30	8.00 ± 0.05
Mass ($M_\odot$)	0.50 ± 0.13	0.67 ± 0.03
Radius ($R_\odot$)	0.0179 ± 0.0039	0.0136 ± 0.0049
Distance (pc):	62 ± 14	53.3 ± 2.2
Cooling age (Myr):	6.3 ± 1.5	4.00 ± 0.62

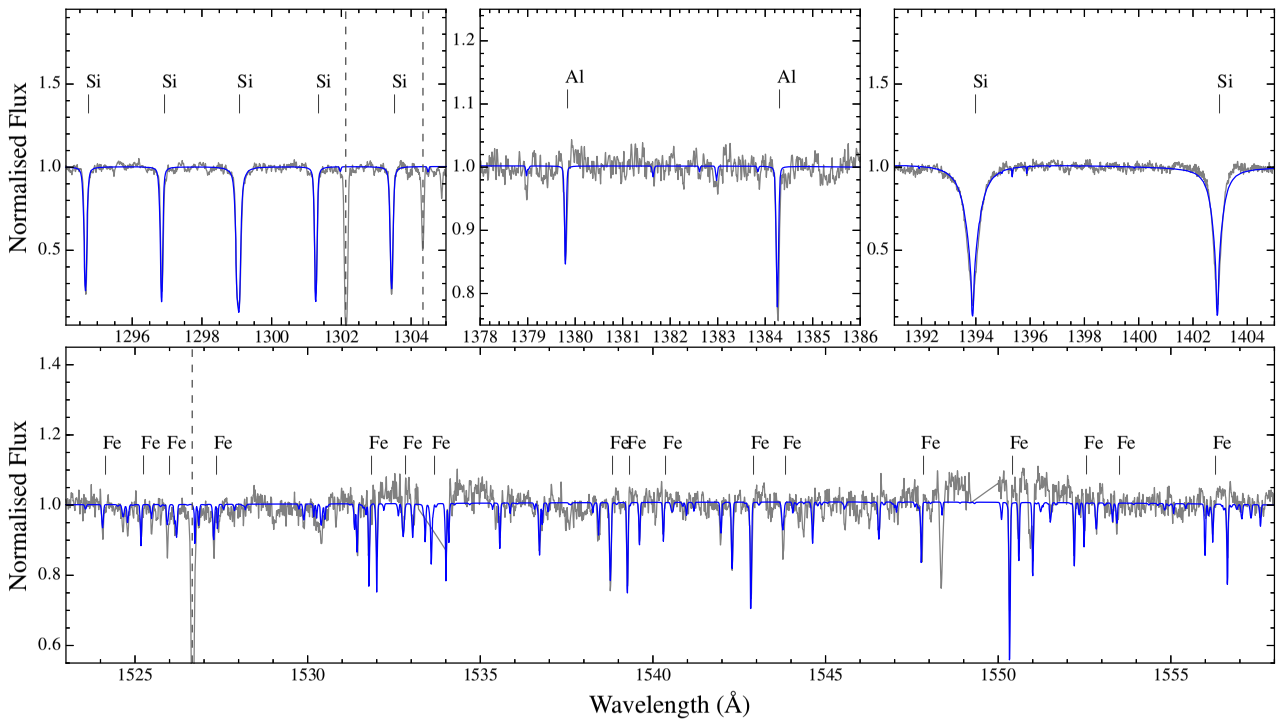

Figure 6.10: Model fit (blue) to the major metal absorption features in the coadded STIS FUV spectrum. The dashed grey lines indicate the position of interstellar absorption lines.

noise ratio of ∼ 80 and resolution of ∼ 0.02 Å. Since the slope of the continuum at this high $T_{\rm eff}$ is not very sensitive to $T_{\rm eff}$, the only feature that determines the result of the fit is the Lyman α line. This leads to a strong degeneracy where a change in $T_{\rm eff}$ can be compensated for by a change in $\log g$. Fortunately there are many silicon lines visible in the spectrum, including the three ionization states, Si II, Si III and Si IV. Fitting each ion separately, we find that the best fit atmospheric parameters to the Lyman α also produces the smallest discrepancies between the three ionization states. We thus adopt $T_{\rm eff} = 33550 \pm 1500$ K and $\log g = 7.63 \pm 0.30$. In addition to Si, we confirm previous detections of Al and Fe (Holberg et al., 1998; Dupuis et al., 2000; Chayer et al., 2000). There are a number of lines that we tentitvly identfy as Ni III, but as they all coincide with strong Fe lines we treat the abundance measured as an upper limit.

6.3.2 FUSE

The absolute flux of the *FUSE* spectrum agrees well with the STIS spectrum in the region of overlap. Extending the model fit to the STIS spectrum to *FUSE* wavelengths, we find that it also agrees well without any changes in $T_{\rm eff}$ or $\log g$, except for the highest Lyman lines where interstellar absorption becomes dominant. The overall fit to the Si and Fe lines (the only ones we detect) is not perfect, but satisfactory. We have not tried to re-fit the abundances, as the STIS spectrum has superior resolution and atomic data that is likely more accurate than in the *FUSE* range.

6.3.3 WHT

Fitting to the Balmer lines returns $T_{\rm eff} = 40082 \pm 988$ K and $\log g = 8.00 \pm 0.05$, higher than the parameters derived from the STIS spectrum. Similar discrepancies between fits to optical and ultraviolet spectra are seen at several hot white dwarfs, although GD 394 is the most pronounced case (Lajoie & Bergeron, 2007). The discrepancy is almost certainly due to our incomplete understanding of white dwarf atmospheric physics. The upcoming *Gaia* Data Release 2 will provide a parallax that can be used to obtain an independent measurement of the mass of GD 394 (Tremblay et al., 2017) which will help resolve this issue. For now, we provide and will discuss the white dwarf parameters inferred from both fits (Table 6.6).

6.3.4 HIRES

The HIRES spectra contain multiple photospheric Si II lines (Figure 6.4), from which we measured a Si abundance of -5.10 ± 0.2. This is clearly incompatible with the abundances obtained from the STIS spectral lines, a discrepancy also reported by Dupuis et al. (2000).

As there are also discrepancies between individual atomic lines in the STIS spectrum this cannot be caused by variation in the line strength between observations, but is more likely due to incomplete atomic data. Several other metal-polluted white dwarfs show similar discrepancies between Si measurements from optical and ultraviolet data (Gänsicke et al., 2012; Xu et al., 2017).

6.3.5 Diffusion, radiative levitation and the origin of the metal lines

Naively assuming that GD 394 has a "standard" DAZ atmosphere, we calculate the strength of radiative levitation of Si according to the procedure given in Koester et al. (2014a) and adopting the atmospheric parameters and Si abundance from the best fit to the STIS spectrum. We find the maximum abundance of Si that can be supported to be $\log(\mathrm{Si/H}) \leq -6.1$, so under the standard accretion-diffusion equilibrium scenario with radiative levitation accounted for GD 394 must be accreting Si at $\dot{M}(\mathrm{Si}) = 1.0 \times 10^6 \mathrm{g\,s^{-1}}$, a low-to-medium rate for DAZ white dwarfs in general (see figure 8 in Koester et al., 2014a). However it is clear that GD 394 is far from a typical DAZ white dwarf given the discrepency between UV and optical fits, EUV variation and the anomalous high-excitation lines discussed below, thus these calculations are suspect. Radiative levitation strengths for Al and Fe were not treated in Koester et al. 2014a, although Chayer et al. 1995b find the radiative support to be low.

Without precise accretion fluxes speculation on the origin of the debris is limited, so we only note that the raw values of $\log(\mathrm{Al/Si}) = -1.11$ and $\log(\mathrm{Fe/Si}) = -0.03$ are close enough to those of the bulk Earth (-0.988 and -0.002 respectively, McDonough, 2000) and the carbon content sufficiently low that there is no reason to doubt that GD 394 is accreting rocky debris from a remnant planetary system (Jura, 2006; Gänsicke et al., 2012).

6.3.6 High-excitation lines

Chayer et al. (2000) identified P v 1117.977 Å and 1128.008 Å absorption lines in the *FUSE* spectrum. The latter line is blended with Fe III and Si IV transitions, so we assume that their P abundance is based on the 1117 Å line[5]. For our best fit model to P v 1117.977Å we obtain $\log(\mathrm{P/H}) = -7.5 \pm 0.2$, in agreement with Chayer et al. (2000). We also detect C IV 1548.202 Å and 1550.774 Å lines at $\log(\mathrm{C/H}) \approx -7.5$, and N v 1238.821 Å and 1242.804 Å lines at $\log(\mathrm{N/H}) \approx -3.7$ (Figure 6.11, left) in the SITS spectrum. All of the lines are at the photospheric velocity (Table A.2), with the possible exception of C IV for which the best fit gives a redshift of $\approx 2\mathrm{km\,s^{-1}}$ relative to adjacent Fe III lines, but this is within the uncertainty of the spectral resolution. Unless this is an unlikely coincidence, these are therefore photospheric features, or are being produced in a layer just above the

[5]We note that Chayer et al. (2000) give the wrong wavelength for this line, 1122Å, in their tables 2 and 3.

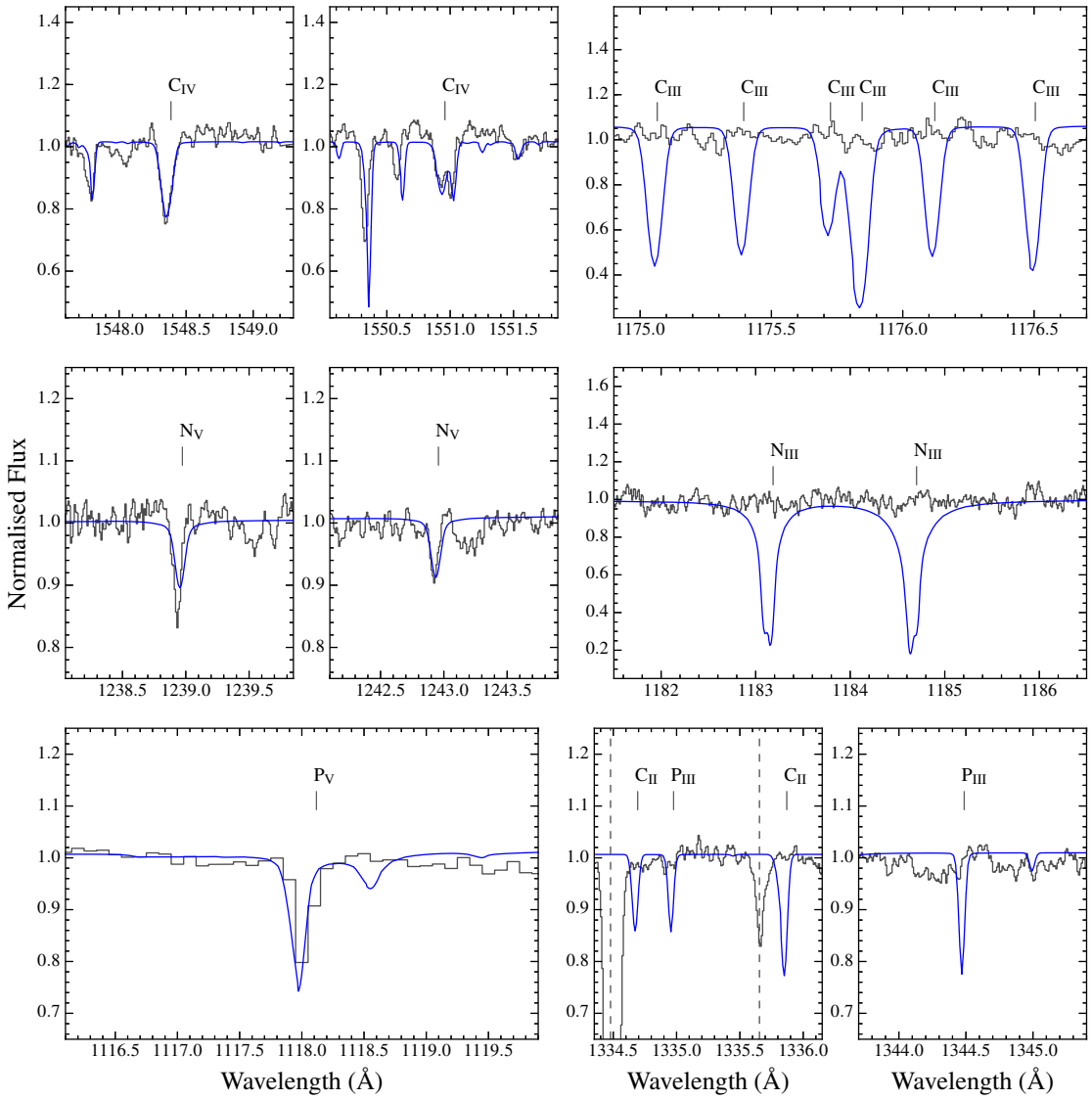

Figure 6.11: Plot showing (left) high-excitation lines of C, N and P in the STIS and FUSE spectra, with a model fit overplotted in blue. The model predicts multiple strong low-excitation lines of the same elements, none of which are detected (right).

Table 6.7: Abundances of metals in the atmosphere of GD 394.

Element		Abundance (log[X/H])		
		STIS	HIRES	High-excitation
6	C	≤ -8.00		-7.50
7	N	≤ -8.00		-3.7
8	O	≤ -5.00		
13	Al	-7.07 ± 0.20		
14	Si	-5.96 ± 0.10	-5.10 ± 0.20	
15	P	≤ -8.00	≤ -6.5	-7.5 ± 0.2
26	Fe	-5.93 ± 0.20		
28	Ni	≤ -7.80		

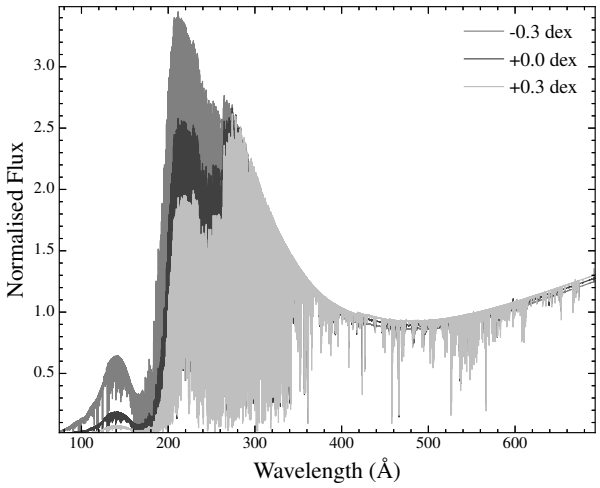

Figure 6.12: EUV models of GD 394 at $T_{\rm eff} = 32500$ K, $\log g = 7.75$. The different spectra show, from light to dark grey, models with metal abundances at the measured value -0.3 dex, 0, and $+0.3$ dex.

photosphere, close enough such that there is no detectable difference in gravitational redshift. We do not detect secondary, clearly circumstellar lines (i.e. outside the gravitational redshift of the white dwarf) such as those detected at multiple white dwarfs by Dickinson et al. (2012).

However, no C II, C III, N III or P III lines are detected in the STIS spectrum, all of which are predicted to be strong based on the measurements from the high-excitation lines (Figure 6.11, right). This non-detection places upper limits on the abundances of all three of C, N and P of $\log({\rm X/H}) \leq -8.00$, clearly incompatible with the measurements from the high-excitation lines (Table 6.7). The higher excitation Si III lines are also too strong for our adopted parameters, requiring $T_{\rm eff} > 40000$ K.

6.4 Modelling the EUV variability

Due to the large number of absorption lines in the EUV spectrum (Figure 6.1), it may be possible that abundance variations too small to be detected in the STIS spectra nevertheless change the EUV flux by the observed 25 per cent. To test this, we simulated the effects of abundance changes on the flux detectable by *EUVE*. The model atmospheres described in Section 6.3 do not extend into the EUV in sufficient detail, so we modelled the EUV spectrum using the using the non-local thermodynamic equilibrium (NLTE) radiative transfer code TLUSTY (Hubeny, 1988; Hubeny & Lanz, 1995), synthesising model spectra with SYNSPEC (Hubeny & Lanz, 2011), including hydrogen Stark broadening profiles as calculated by Tremblay & Bergeron (2009).

A grid of model atmospheres were calculated in NLTE over the temperature range $25000\,\mathrm{K} \leq T_{\mathrm{eff}} \leq 50,000\,\mathrm{K}$ in steps of 2500 K, and surface gravities $7.00 \leq \log g \leq 9.00$ in steps of 0.25 dex. For each T_{eff} and $\log g$ combination we used SYNSPEC to produce model atmospheres with the measured abundances ±0.3 dex. As the uncertainties on these abundances are ≈ 0.2 dex, such a change in abundance should be clearly visible in the STIS spectra. Each model spectrum was then integrated over the combined *EUVE* effective area[6] to measure the effects on the flux produced by the simulated changes in metal abundances (Figure 6.12).

We find that only models with $T_{\mathrm{eff}} \lesssim 30000\,\mathrm{K}$ produce changes in integrated flux > 25 per cent, temperatures which are clearly ruled out by our model atmosphere fit to the spectrum. At the best-fit temperature we find a maximum change in flux of ≈ 10 per cent, with clearly detectable changes in absorption line strength in the FUV. Combined with the lack of optical variation, we therefore confidently rule out an accretion spot as the (primary) source of the EUV flux variation.

6.5 Non-detection of gaseous emission

Ca II 8600 Å emission from a gaseous component to a debris disc has been observed at 8 white dwarfs to date (Gänsicke et al., 2006; Guo et al., 2015). The emission takes a distinct double-peaked morphology induced by the Keplarian orbital motion of the disc material (Horne & Marsh, 1986). Burleigh et al. (2011) observed GD 394 as part of a search for gaseous emission at hot white dwarfs, returning no detections. As gaseous discs can form on ∼ year-long timescales (Wilson et al., 2014), it is worth noting that our 2016 WHT/ISIS observation also failed to detect emission (Figure 6.13). Non-detection of gaseous emission is unsurprising, as in all known cases it is associated with the presence of an infrared

[6] https://archive.stsci.edu/euve/analysis.html

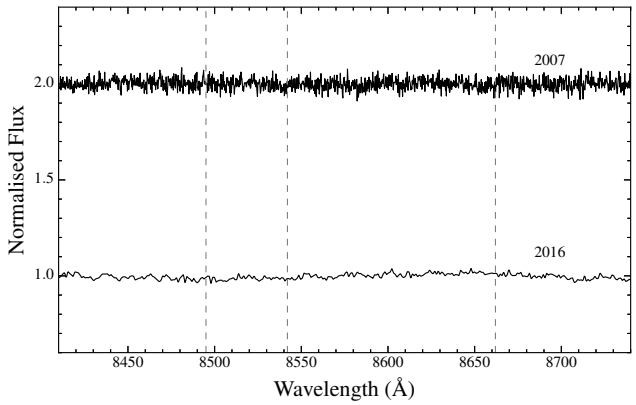

Figure 6.13: WHT/ISIS spectra covering the Ca II 8600Å triplet, illustrating the persistent non-detection of double-peaked gaseous emission. The dashed lines show the rest wavelengths of the Ca II triplet. The 2007 spectrum has been offset by +1 for clarity.

excess from dusty debris (Brinkworth et al., 2012), which was ruled out at GD 394 by Mullally et al. (2007). Dust at GD 394 will sublimate at radii greater than the Roche radius, preventing the formation of a compact dusty debris disc (von Hippel et al., 2007).

6.6 Discussion

GD 394 is not variable at any of the wavelengths and timescales explored here, contrasting strongly with the clear EUV variability observed by Dupuis et al. (2000).

A potential explanation is that the accretion spot hypothesis was correct, but that the spot has dispersed since the *EUVE* observations and GD 394 is now accreting uniformly over its surface. The low accretion rate and lack of Ca II emission lines suggest that the circumstellar environment may be relatively inactive, with the short diffusion timescales removing any proof of higher activity in the past. However, this explanation conflicts with the perfect match between the GHRS and STIS observations (Figure 6.8). The GHRS observations were obtained less than a year before the first *EUVE* observations, so it is unlikely that the EUV variation was not present at that epoch, especially as it was detected in all further *EUVE* observations over the following four years. Any long-term variation in the accretion rate or surface distribution of metals should likely have produced noticeable differences between the STIS and GHRS spectra.

If the EUV variation was still present during all of the observations presented here, then an accretion spot can be ruled out as the cause. An alternative possibility is that GD 394 hosts a planet on a 1.15 day orbit. Multiple hot Jupiter planets have been observed with ultraviolet transits 5–10 per cent deeper than in the optical (Haswell et al., 2012), interpreted

as the transit of a cloud of evaporating material around the planet. Given the small size of GD 394, it is conceivable that an orbiting planet may not transit itself but be surrounded by a hydrogen cloud that clips the white dwarf, causing the EUV variations. The Lyman α absorption seen in main sequence examples (Vidal-Madjar et al., 2003) is masked by the deep, wide photospheric and interstellar absorption at GD 394. Assuming that the 1.15 d signal detected in the EUV is the orbital period of a planet, then the equilibrium surface temperature of the planet will be $\approx$ 1300 K, enough to induce atmospheric evaporation (Tripathi et al., 2015). The mass lost by this planet would also accrete onto GD 394, providing the reservoir for the photospheric metal pollution (see Farihi et al. ???? for an example of a white dwarf with both a low-mass companion and planetary debris). Testing this hypothesis will require high–precision radial velocity measurements, although this will be challenging due to the paucity of photospheric absorption lines at optical wavelengths (Figure 6.4).

As is common in hot white dwarfs, there is a discrepancy in $T_{\rm eff}$ and $\log g$ between our model atmosphere fits to ultraviolet and optical spectra. The fit to the optical spectra results in an inferred white dwarf mass of $0.67 \pm 0.03 M_{\odot}$, which is near the peak of the white dwarf mass distribution (Tremblay et al., 2016) and unremarkable. However, the low mass measured from the STIS spectrum ($0.50 \pm 0.13\,M_{\odot}$) is on the boundary for GD 394 to be a helium core white dwarf (Althaus & Benvenuto, 1997) and, using the initial-to-final mass relationship of Casewell et al. (2009), implies a progenitor mass of $\approx 0.8\,M_{\odot}$, too low for the star to have evolved off the main sequence within the age of the Galaxy. Similar low-mass white dwarfs are plentiful, resulting in a peak at $\approx 0.4\,M_{\odot}$ in multiple measurements of the white dwarf mass distribution (Liebert et al., 2005; Kleinman et al., 2013). The majority of these low mass white dwarfs are found in Post-Common Envelope Binaries (PCEBS Rebassa-Mansergas et al., 2011), and are likely formed by truncation of the core growth of the more massive star during the common-envelope stage. However, 20–30 per cent of white dwarfs in the range 0.25–0.5 $M_{\odot}$ are single stars (Brown et al., 2011). Several formation channels have been suggested for low-mass white dwarfs. A natural outcome of the PCEB model is that the companion merges with the white dwarf before the end of the common envelope phase, but population synthesis studies by Nelemans (2010) predict too few low-mass white dwarfs to match observations. Other proposed explanations include enhanced mass loss on the giant branch for high-metallicity progenitors (Kilic et al., 2007), or mergers of cataclysmic variables due to angular momentum loss induced by mass-transfer (Zorotovic & Schreiber, 2017). Perhaps of most relevance to GD 394, due to the metal pollution which independently establishes the presence of a remnant planetary system, is the prediction of Nelemans & Tauris (1998) that a substellar companion with M$\sim$ 20, $M_{\rm Jup}$ caught in a common envelope could remove enough of the envelope to produce a low mass white dwarf. Although this is higher than our upper limit for a planetary

companion of $M \sin i > 8\,M_{\rm Jup}$, a larger planet or brown dwarf could have been removed by engulfment or tidal disruption, or been eroded by the common envelope to a final mass below our detection limit (Villaver & Livio, 2007; Mustill & Villaver, 2012).

The high excitation lines observed in the STIS and FUSE spectra may be being produced in a high-temperature accretion flow similar to that observed in cataclysmic variables (Patterson & Raymond, 1985), but that would still lead to accretion of C, N and P in the photosphere. Radiative levitation is potentially strong enough to expel all C from the photosphere but the predicted support for N is far too low (Chayer et al., 1995b). Lallement et al. (2011) detected C IV lines without corresponding C III lines at two white dwarfs with similar $T_{\rm eff}$ to GD 394. In contrast, the $T_{\rm eff} = 28000 - 30000$ K white dwarf component of the dwarf nova U Geminorium (U Gem) has N V lines at photospheric wavelengths, which require $T_{\rm eff} \approx 80000$ K to appear (Sion et al., 1998; Long & Gilliland, 1999), but does have low-excitation N lines that require a super-Solar N abundance to fit (Long et al., 2006). If radiative levitation is expelling both N and C at GD 394 then we would expect the same to happen white dwarfs with similar $T_{\rm eff}$; this is clearly not the case.

6.7 Conclusion

We obtained multi-wavelength observations of GD 394 to test the accretion spot hypothesis put forward by Dupuis et al. (2000) to explain the large amplitude flux variations detected in the EUV. We find no evidence for any change in photosphereic metal abundances over the 1.15 d period of the EUV variation, nor on the decades-long timescales covered by various *HST* spectroscopy. No photometric variability is observed beyond the EUV at any waveband. The EUV variation has either stopped, although the agreement between near-contemporaneous spectra and more recent observations disfavours this explanation, or is being caused by some phenomena other than a spot. Distinguishing between these scenarios will require new observations in the EUV (or perhaps soft X-rays).

Beyond a search for variation, our observations show GD 394 to be a highly unusual white dwarf. As with previous studies for multiple hot white dwarfs, we cannot obtain consistent atmospheric parameters between fits to the optical and ultraviolet hydrogen lines. The observed metal lines are also contradictory, especially the presence of photospheric high-excitation lines that predict many low-excitation lines that are not observed.

Chapter 7

Discussion and Conclusions

"It's the end of the world every day, for someone."

Margaret Atwood, The Blind Assassin

7.1 Discussion

With the four investigations presented in Chapters 3–6, I have demonstrated the wide breadth of contributions that observations of remnant planetary systems can make to exoplanetary science. Here I will briefly summarise these chapters and discuss their significance for exoplanet research, followed by suggestions for future research based on upcoming surveys and space missions.

7.1.1 Thesis summary

Chapter 3 presented the discovery of variable emission from a gaseous component to the debris disc at SDSS 1617+1620. This is the first and thus far only gaseous disc component to show significant variability in overall line strength, forming and disappearing again within just eight years. By comparison, the gaseous emission at SDSS J0845+2257 shown in Chapter 4 is much more typical of the class, demonstrating gradual changes in line morphology with little change in overall strength. The variable emission demonstrates that remnant planetary systems around white dwarfs are active on timescales of years, providing an opportunity to test models of planetesimal scattering and disruption. Conversely, the non-detection of any change in the accretion rate onto the white dwarf itself suggests that the accretion process is decoupled from the changes in the debris disc, providing a constraint for disc accretion theories. Ongoing monitoring of this and other discs will search for similar changes in emission that may constrain the occurrence rates and formation mechanisms of the gas.

Chapter 4 presents a comprehensive study of the remnant planetary system at the white dwarf SDSS J0845+2257. I utilised time-series spectroscopy to chart gaseous emission from a debris disc, high-cadence photometry to search for accretion-induced flares and transiting debris, and, most significantly, high-resolution spectroscopy in both ultraviolet and optical wavebands that revealed a plethora of metals accreting onto the white dwarf atmosphere. The metals originate in the orbiting planetesimal debris disc, so by measuring the metal abundances, I was able to explore the bulk chemical composition of the debris. Aspects of the debris chemistry could be compared with the Solar system, namely the relatively high mass fraction of core material, the water content and the high levels of carbon. Comparison with another published study of the same object (Jura et al., 2015) demonstrated some of the outstanding challenges in white dwarf physics that may lead to different results depending on the choice of data and theoretical framework.

Whist the observations of SDSS 0845+2257 demonstrated the utility of polluted white dwarfs for measuring the bulk chemistry of individual extrasolar planetesimals in detail, Chapter 5 instead demonstrates how measuring just a handful of metals in a large sam-

ple of white dwarfs can be used to draw conclusions about exoplanet chemistry in general. In this analysis, I searched for evidence for the existence of "carbon planets" with carbon to oxygen ratios > 0.8. Such objects are indistinguishable from planets with Earth-like chemistry via standard exoplanet detection techniques, but would have surfaces inimical to life as we know it. By placing an upper limit on their occurrence rate, I have provided a constraint that is already informing models of exoplanet formation (Mordasini et al., 2016). Future studies using larger sample sizes and/or different areas of chemistry will further constrain the parameter space of extant planetary compositions.

Finally, observations of metal polluted white dwarfs can reveal objects that are interesting for their own sake, regardless of their contribution to a larger field. In Chapter 6 I present new observations of GD 394, a white dwarf showing unique extreme ultraviolet variability. My observations were partially successful: whilst I was unable to offer a mechanism for the variability that satisfactory explained all of the observations, I was able to comprehensively discount the previously favoured hypothesis of a dark accretion spot and detected high-excitation lines that may be evidence for an accretion interface layer. This project has pushed to the boundaries of currently available instrumentation and theoretical modelling for white dwarf science, and will leave a legacy data set that will aid future attempts to understand the puzzling properties of GD 394.

7.1.2 Future work

The near future of remnant planetary system science, as with many other areas of astronomy, will see a vast increase in the quantity and quality of data available, both in overall sample size and for individual stars. With regards to measuring planetary chemistry, the actual maximum achievable data *quality* is unlikely to increase. Better optical spectroscopy will be obtained when the 30+ m telescopes begin to come online in the 2020s (Gilmozzi & Spyromilio, 2007; Skidmore et al., 2015; Johns et al., 2012), but ultraviolet spectroscopy will be limited to the capabilities of *HST* until at least the mid-2030s, and possibly beyond. What will increase is the number of white dwarfs for which the best data is available, with well over 100 *HST* and dozens of ground-based observations already planned for the next couple of years, more than tripling the sample of white dwarfs at which the debris chemistry can be studied in detail. Future work will therefore resemble combinations of Chapters 4 and 5, exploring detailed chemistry over a large sample size. In this way the limitations of achievable resolution and confidence in the particular diffusion scenario for individual objects will be less concerning, as they will be averaged out over the whole sample. Example areas of planetary chemistry than can be explored include the effects of Mg and Si on mantle chemistry (Unterborn et al., 2017), searches for more iron-rich objects to test the mantle stripping hypothesis put forward in Chapter 4 and, perhaps most intriguingly from a plan-

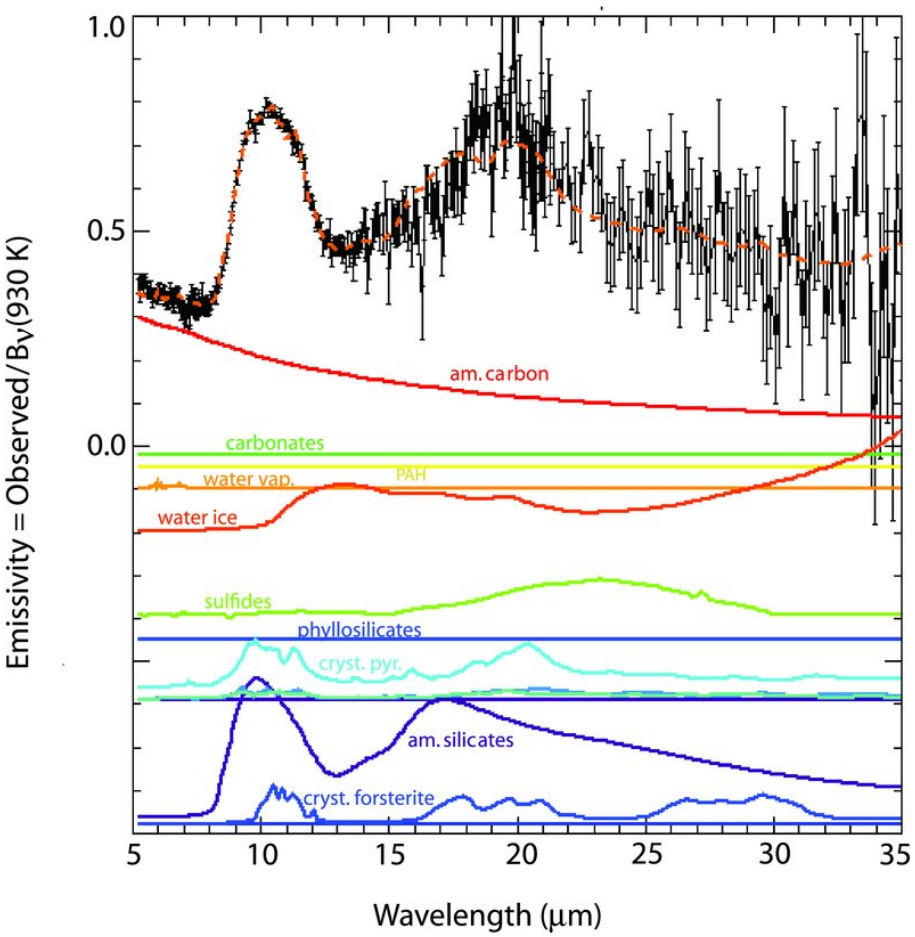

Figure 7.1: *Spitzer*/IRS infrared spectrum of the dusty disc at G 29-38, fitted as a combination of mineral species (Reach et al., 2009). *JWST* will increase both the precision of such observations and the sample of targets at which they can be obtained.

etary habitability point of view, probing the occurrence rate of water-rich objects (Farihi et al., 2013b).

An almost entirely new observational window onto remnant planetary systems will open with the launch of the *James Webb Space Telescope* (*JWST*, Gardner et al., 2006). Placed in orbit around around the Sun-Earth L2 Lagrange point in late 2018, *JWST* will have a 6.5 m segmented primary mirror and four detectors capable of imaging and spectroscopic observations in the infrared over a wavelength range of 0.6–27 microns. Spectroscopic observations of white dwarfs with dusty debris discs will therefore become possible, probing the mineralogy of the debris at a stage before it is sublimated into individual elements. Figure 7.1 shows the one case where this has been carried out, an observation of the bright prototype dusty disc at G 29-38 with the *Spitzer Space Telescope* Infrared Spec-

trograph (IRS) by Reach et al. (2009). The spectrum shows clear emission features, most prominently from amorphous silicates at $\approx$ 10 and 20 microns. However the signal-to-noise of the spectrum is so poor that the precise mineralogy fit is degenerate, and none of the other dust discs were bright enough to enable similar observations. *JWST* will provide improved data for multiple stars, allowing the mineralogy of the debris to be confidently measured and compared across systems. Furthermore, the photospheric debris abundances of the possible targets has now been measured in detail, providing improved constraints to the mineralogical composition. For example, including the amorphous carbon in Figure 7.1 is likely not correct, as discussed in Chapter 5. *JWST* can also be used to search for new infrared excesses indicative of dusty debris, searching for excesses too low or at white dwarfs to faint to be observed with *Spitzer*. The improved spatial resolution and sensitivity offered by *JWST*'s imaging instruments will enable direct imaging searches for substellar and planetary companions.

Moving on from debris chemistry, searches for transiting planets and planetesimals have seen a resurgence after the discovery of transits at WD 1145+017 (Vanderburg et al., 2015). The *Kepler* K2 mission, which was the first to detect the transits at WD 1145+017, is likely to continue observing into 2018 with fields containing hundreds of white dwarfs. Searches for transiting planets or planetary debris can piggyback on surveys of main-sequence stars as the basic strategy is the same. For example, the Next Generation Transit Survey (NGTS), an array of twelve 20 cm telescopes based at Cerro Paranal in Chile, will monitor fields containing hundreds of white dwarfs for months at a time at 30 s cadence. NGTS will be able to detect transits of Mars-sized objects down to 18^{th} magnitude, easily sufficient to detect WD 1145+017 analogues (Braker et al., 2015). Targeted surveys of white dwarfs already known to host planetary systems (i.e., those with observed dusty debris discs and/or heavy metal pollution) with instruments capable of high-precision photometry such as ULTRACAM (Dhillon et al., 2007) may also recover planetary transits, or at least place limits on their occurrence rate.

Beyond the end of the K2 mission, future spacecraft can also be utilised to search for transits at white dwarfs. The *Transiting Exoplanet Survey Satellite* (*TESS*, Ricker et al., 2015), planned for launch in March 2018, will use an array of four wide-field cameras to photometrically survey large areas of the sky for periods of $\sim$ 1 month to 1 year. The small aperture size of the cameras will limit observations to brighter ($V \lesssim 14$) white dwarfs, but still leaves hundreds of targets that will be ideal for follow-up observations with ground-based telescopes. Further into the future, the *Planetary Transits and Oscillations of Stars* (*PLATO*, Rauer et al., 2014) is a much larger transit-hunting spacecraft planned for launch in 2026, which will observe fields of several thousand square degrees for two years at a time down to 16^{th} magnitude. Although white dwarfs are not included in *PLATO*'s baseline

observing strategy, they will be included as part of General Observer programs.

All of these surveys will of course need white dwarfs to target. Identification of new white dwarfs will be made possible by a number of surveys and instruments. Chief among these is the *Gaia* (Gaia Collaboration et al., 2016) spacecraft, launched on 2013 December 19. *Gaia* is a survey satellite intended to make precision astrometry measurements for targets down to 20^{th} magnitude, providing precise positions, parallaxes and proper motions for around a billion stars. Very-low resolution spectra ($R \sim 100$) will be also be taken of all targets, along with high-resolution spectra centred on the Ca II 8600 Å triplet for brighter targets. Included in this sample will be approximately 400 000 new white dwarfs, with preliminary identifications made by combining the astrometric and photometric information (Jordan, 2015). *Gaia* may also be able to detect exoplanets at white dwarfs, possible via transits but more likely via astrometry, whereby the orbit of the white dwarf around the white dwarf-planet barycentre is directly measured thanks to *Gaia*'s excellent spatial precision. Silvotti et al. (2015) predict that around a hundred planets with Jupiter masses and above may be detected in this fashion. However, with the exception of white dwarfs around ≈ 12000 K where the low-resolution spectroscopy may detect the Balmer lines, confirmation and classification of *Gaia* white dwarfs will require follow-up spectroscopy.

Fortunately a large number of multi-object spectrographs are now being planned or commissioned, building on the success of SDSS but moving to 4 m and larger telescopes. WEAVE (Dalton et al., 2014), DESI (Flaugher & Bebek, 2014) and 4MOST (de Jong et al., 2014) will between them cover the majority of the sky, providing spectra of thousands of white dwarfs either as secondary science targets or as calibrators. From this sample the most promising candidates can be observed with the facilities described above to probe their remnant planetary systems.

7.2 Conclusion

Observations of white dwarfs can provide invaluable contributions to exoplanetary science. Here I have presented examples of how they can explore the dynamics of planetary systems via detections of variable debris discs, and provide our best method to measure the bulk chemical composition of rocky exoplanetary material. As the previous section has shown, the future for this area is bright, with many of the major astronomical facilities coming online in the next few years contributing in major ways. White dwarfs represent the end stages of stellar evolution for the majority of stars, so these observations provide an insight into the fate of almost all planetary systems. Many billions of years from now, an alien astronomer looking at the white dwarf left by the Sun may write a very similar thesis.

Appendix A

Absorption line lists for GD 394

Table A.1: Observed photospheric metal absorption lines detected in the FUSE, STIS and HIRES spectra. The rest wavelengths for lines detected in HIRES spectra use the air value, all others use the vacuum value. Each line was fitted with a Gaussian curve using ASTROPY least-squares fitting routines, and the equivalent width measured according to the prescriptions found in Vollmann & Eversberg (2006). *Blended with C IV 1550.77 Å.

Line	Rest λ (Å)	Observed λ (Å)	ΔV (kms^{-1})	Equivalent Width (mÅ)
FUSE				
Fe III	983.88	983.925	13.8 ± 6.17	25.0 ± 3.7
Fe III	985.0	985.889	271.0 ± 14.1	16.0 ± 4.4
Fe III	986.0	986.651	198.0 ± 18.5	3.5 ± 3.5
N III?	989.7	989.784	25.4 ± 17.1	36.0 ± 2.7
N III	991.5	991.899	121.0 ± 15.9	35.0 ± 3.1
Si III	993.52	993.585	19.6 ± 12.6	46.0 ± 2.4
Si III	994.79	994.845	16.7 ± 6.68	81.0 ± 3.1
Si III	997.39	997.468	23.4 ± 3.6	87.0 ± 3.5
Fe III	1017.25	1017.3	15.8 ± 11.8	12.0 ± 2.7
Fe III	1018.29	1018.32	9.82 ± 29.1	−0.4 ± 2.7
Si III	1108.37	1108.41	10.9 ± 12.9	76.0 ± 1.9
Si III	1109.97	1110.01	10.8 ± 5.87	110.0 ± 2.1
Si III	1113.23	1113.27	10.0 ± 0.798	160.0 ± 2.7
Si III/Si IV	1122.49	1122.53	9.66 ± 1.19	120.0 ± 2.7
Si IV	1128.34	1128.38	11.3 ± 4.52	150.0 ± 3.1
Si III	1144.31	1144.43	30.8 ± 32.1	18.0 ± 1.1
STIS				
Si II	1194.496	1194.59	24.3 ± 14.0	20.0 ± 17.0
Si III	1206.5	1206.62	28.9 ± 1.08	260.0 ± 45.0
Si III	1207.517	1207.62	25.5 ± 8.08	34.0 ± 8.1
Fe III?	1210.4	1210.56	40.9 ± 1.53	20.0 ± 13.0
Si III	1235.43	1235.58	35.3 ± 1.53	26.0 ± 7.9
Si III	1235.43	1235.58	35.3 ± 1.53	26.0 ± 7.9
Si III	1238.8	1238.92	30.1 ± 2.65	10.0 ± 8.6
Fe II?	1242.8	1242.91	27.3 ± 5.28	7.2 ± 13.0
Si II	1250.43	1250.54	27.4 ± 3.36	10.0 ± 8.8
Si II	1264.738	1264.85	26.6 ± 1.07	25.0 ± 6.7
Si III	1280.35	1280.47	28.2 ± 2.19	13.0 ± 9.0
Si III	1294.545	1294.67	28.9 ± 0.38	81.0 ± 8.3
Si III	1296.726	1296.87	32.4 ± 0.68	79.0 ± 7.3
Si III	1298.892	1299.06	38.3 ± 0.587	150.0 ± 12.0
Si III	1301.149	1301.27	27.6 ± 3.2	72.0 ± 6.7
Si III	1303.323	1303.44	26.5 ± 3.37	77.0 ± 6.2
Si II	1305.2	1305.33	30.1 ± 59.3	3.7 ± 2.6
Si II	1309.27	1309.39	27.8 ± 8.38	4.5 ± 6.7
Si III	1312.591	1312.71	28.0 ± 0.487	44.0 ± 6.6
Si III	1341.458	1341.59	29.2 ± 2.11	38.0 ± 7.2

Table A.1: Continued.

Line	Rest λ (Å)	Observed λ (Å)	ΔV (kms^{-1})	Equivalent Width (mÅ)
Ni III	1342.1	1342.51	91.9 ± 2.82	35.0 ± 8.0
Si III	1343.409	1343.52	24.4 ± 4.56	22.0 ± 6.7
Si III	1361.596	1361.72	26.3 ± 2.12	24.0 ± 6.8
Si III	1362.37	1362.49	25.9 ± 6.99	11.0 ± 6.6
Si III	1363.459	1363.58	27.2 ± 4.42	21.0 ± 6.5
Si III	1365.253	1365.39	29.2 ± 2.14	34.0 ± 7.4
Si III	1367.027	1367.17	30.6 ± 5.0	16.0 ± 5.8
Si III	1369.44	1369.57	27.8 ± 4.29	13.0 ± 12.0
Si III	1373.03	1373.15	26.6 ± 3.25	6.7 ± 6.1
Al III	1379.67	1379.79	25.6 ± 2.56	8.2 ± 11.0
Al III	1384.132	1384.27	29.4 ± 1.32	21.0 ± 8.0
Si III	1387.99	1388.13	29.5 ± 0.0	11.0 ± 19.0
Si IV	1393.755	1393.88	26.9 ± 0.576	480.0 ± 49.0
Si IV	1402.77	1402.89	26.4 ± 0.38	310.0 ± 34.0
Ni III	1433.6	1433.8	41.7 ± 2.29	14.0 ± 10.0
Si III	1435.772	1435.91	28.7 ± 1.51	32.0 ± 9.1
Ni III	1436.7	1436.86	32.9 ± 10.6	11.0 ± 11.0
Fe/Ni?	1457.2	1457.42	44.4 ± 4.92	5.2 ± 7.8
Fe III	1465.7	1465.89	38.9 ± 13.0	13.0 ± 21.0
Ni III	1467.7	1467.89	37.9 ± 0.0	4.8 ± 5.2
Fe III	1467.7	1467.89	37.9 ± 7.47	4.9 ± 5.3
Ni III	1469.8	1470.0	40.7 ± 6.31	11.0 ± 16.0
Fe III	1469.8	1470.0	40.7 ± 6.49	11.0 ± 16.0
Fe III	1481.1	1481.34	47.9 ± 10.4	9.5 ± 17.0
Si III	1500.241	1500.38	27.4 ± 3.3	53.0 ± 9.8
Si III	1501.15	1501.32	33.9 ± 3.0	59.0 ± 12.0
Si III	1501.197	1501.32	24.3 ± 3.12	61.0 ± 14.0
Si III	1501.78	1502.0	43.7 ± 4.13	49.0 ± 11.0
Si III	1501.827	1501.99	33.0 ± 3.88	50.0 ± 14.0
Fe III	1504.0	1504.16	31.9 ± 16.1	6.3 ± 11.0
Fe III	1505.1	1505.29	37.0 ± 5.42	13.0 ± 9.4
Si III	1506.06	1506.2	27.8 ± 4.1	11.0 ± 8.4
Fe III	1511.6	1511.76	30.9 ± 6.8	6.9 ± 13.0
Fe IV?	1523.9	1524.07	33.6 ± 5.56	4.7 ± 4.3
Fe IV	1523.923	1524.07	29.1 ± 5.59	4.5 ± 4.1
Fe III	1524.5	1524.65	30.3 ± 10.9	3.6 ± 4.0
Fe III	1524.6	1524.78	36.3 ± 0.0	6.2 ± 9.0
Fe III	1525.036	1525.16	24.7 ± 50.0	6.3 ± 8.1
Fe III	1525.798	1525.94	27.7 ± 25.0	6.4 ± 3.7
Fe III?	1526.5	1526.67	33.3 ± 0.767	75.0 ± 13.0
Fe III	1527.141	1527.28	27.9 ± 30.3	7.5 ± 6.8
Fe III	1531.64	1531.78	27.1 ± 6.8	7.7 ± 8.3

Table A.1: Continued.

Line	Rest λ (Å)	Observed λ (Å)	ΔV (kms^{-1})	Equivalent Width (mÅ)
Fe III	1531.864	1531.99	24.5 ± 8.34	7.2 ± 5.1
Fe IV	1532.63	1532.77	27.6 ± 16.8	4.0 ± 3.8
Fe IV	1536.577	1536.72	28.8 ± 8.04	8.8 ± 7.8
Fe III	1538.629	1538.77	26.5 ± 4.15	14.0 ± 8.3
Fe III	1539.123	1539.26	26.6 ± 4.53	10.0 ± 6.4
Fe III	1539.473	1539.61	27.3 ± 11.5	5.4 ± 6.8
Fe III	1540.164	1540.3	26.2 ± 13.2	2.7 ± 6.5
Fe III	1541.831	1541.96	24.7 ± 10.7	5.8 ± 7.5
Fe IV	1542.155	1542.3	27.4 ± 4.89	11.0 ± 8.8
Fe IV	1542.698	1542.84	28.2 ± 2.95	16.0 ± 8.0
Fe III	1543.623	1543.78	29.7 ± 6.75	11.0 ± 9.9
Fe III	1547.637	1547.78	28.0 ± 6.98	11.0 ± 9.1
Fe III	1550.193	1550.33	26.0 ± 3.29	18.0 ± 8.0
Fe III*	1550.862	-	-	-
Fe III	1552.065	1552.19	25.1 ± 9.32	8.3 ± 8.1
Fe IV	1552.349	1552.49	28.1 ± 12.1	4.1 ± 4.9
Fe IV	1552.705	1552.84	26.0 ± 12.4	5.3 ± 8.5
Fe IV	1553.296	1553.44	27.9 ± 8.7	6.5 ± 11.0
Fe III	1556.076	1556.21	26.3 ± 8.62	3.5 ± 6.7
Fe III	1556.498	1556.62	24.0 ± 4.58	6.6 ± 4.5
Al III	1605.766	1605.91	27.6 ± 2.48	27.0 ± 16.0
Fe III?	1607.7	1607.87	30.8 ± 5.13	20.0 ± 14.0
Al III	1611.873	1611.99	22.6 ± 1.52	64.0 ± 30.0
Ni III	1614.0	1614.18	32.9 ± 11.8	9.5 ± 17.0
HIRES				
Si III	3791.439	3791.76	25.4 ± 0.98	5.8 ± 2.2
Si III	3796.124	3796.47	27.3 ± 0.42	18.0 ± 3.3
Si III	3806.525	3806.89	28.8 ± 0.61	28.0 ± 4.6
Si III	3924.468	3924.85	29.2 ± 1.53	6.6 ± 4.4
Si III	4552.622	4553.04	27.5 ± 0.40	38.0 ± 4.3
Si III	4567.84	4568.27	28.2 ± 0.24	32.0 ± 3.2
Si III	4574.757	4575.19	28.4 ± 0.62	18.0 ± 3.3
Si III	5739.734	5740.31	30.1 ± 1.1	20.0 ± 1.8

Table A.2: High-excitation absorbtion lines suspected to be circumstellar detected in the FUSE and STIS spectra.*Blended with Fe III 1550.862 Å.

Line	Rest λ (Å)	Observed λ (Å)	ΔV (kms^{-1})	Equivalent Width (mÅ)
FUSE				
P V	1117.977	1118.03	13.5 ± 3.05	33.0 ± 1.9
STIS				
N V	1238.821	1238.93	26.3 ± 2.85	11.0 ± 8.1
N V	1242.804	1242.92	28.7 ± 4.56	6.7 ± 8.5
C IV	1548.187	1548.35	31.5 ± 2.34	19.0 ± 12.0
C IV*	1550.77	-	-	-

Table A.3: ISM absorption lines detected in the FUSE, STIS and HIRES spectra.

Line	Rest λ (Å)	Observed λ (Å)	ΔV (kms^{-1})	Equivalent Width (mÅ)
FUSE				
O I	988.773	988.66	−34.4 ± 4.76	94.0 ± 3.8
N II?	1084.5	1083.93	−157.0 ± 2.93	63.0 ± 2.1
STIS				
Si II	1190.4158	1190.38	−9.69 ± 0.79	68.0 ± 13.0
Si II	1193.2897	1193.25	−9.07 ± 0.953	89.0 ± 12.0
N I	1199.5496	1199.51	−10.1 ± 2.77	74.0 ± 10.0
N I	1200.2233	1200.18	−10.1 ± 3.12	67.0 ± 10.0
N I	1200.7098	1200.67	−10.0 ± 5.24	51.0 ± 10.0
S II	1253.805	1253.77	−9.48 ± 3.7	19.0 ± 16.0
S II	1259.518	1259.47	−10.9 ± 19.6	12.0 ± 5.9
Si II	1260.4221	1260.39	−8.62 ± 0.949	110.0 ± 8.6
O I	1302.168	1302.13	−8.77 ± 2.29	110.0 ± 7.1
Si II	1304.3702	1304.33	−8.38 ± 4.68	39.0 ± 6.3
C II	1334.532	1334.49	−9.3 ± 0.397	130.0 ± 7.9
C II	1335.708	1335.65	−13.5 ± 25.2	13.0 ± 8.8
Si II	1526.7066	1526.67	−7.18 ± 0.821	75.0 ± 13.0
Al II	1670.7874	1670.74	−8.14 ± 1.01	54.0 ± 20.0
Fe II	2586.65	2586.58	−7.55 ± 4.01	61.0 ± 46.0
Fe II	2600.173	2600.1	−8.17 ± 2.23	120.0 ± 49.0
Mg II	2796.352	2796.26	−10.1 ± 1.54	170.0 ± 74.0
Mg II	2803.531	2803.44	−9.67 ± 1.85	180.0 ± 67.0
HIRES				
Ca II	3933.663	3933.53	−10.2 ± −0.18	12.0 ± 2.1
Ca II	3968.469	3968.32	−11.3 ± −0.53	5.0 ± 0.51

Bibliography

Abazajian, K. N., et al., 2009, ApJS, 182, 543

Adelman-McCarthy, J. K., et al., 2008, ApJS, 175, 297

Agol, E., 2011, ApJ Lett., 731, L31

Aitken, R. G., 1922, PASP, 34, 353

Allègre, C., Manhès, G., Lewin, E., 2001, Earth and Planetary Science Letters, 185, 49

Allègre, C. J., Poirier, J., Humler, E., Hofmann, A. W., 1995, Earth and Planetary Science Letters, 134, 515

Althaus, L. G., Benvenuto, O. G., 1997, ApJ, 477, 313

Althaus, L. G., García-Berro, E., Córsico, A. H., Miller Bertolami, M. M., Romero, A. D., 2009, ApJ Lett., 693, L23

Althaus, L. G., Córsico, A. H., Isern, J., García-Berro, E., 2010, A&AR, 18, 471

Appenzeller, I., et al., 1998, The Messenger, 94, 1

Astropy Collaboration, et al., 2013, 558, A33

Bannister, N. P., Barstow, M. A., Holberg, J. B., Bruhweiler, F. C., 2003, MNRAS, 341, 477

Barstow, M. A., Holberg, J. B., Hubeny, I., Lanz, T., Bruhweiler, F. C., Tweedy, R. W., 1996, MNRAS, 279, 1120

Barstow, M. A., Barstow, J. K., Casewell, S. L., Holberg, J. B., Hubeny, I., 2014, MNRAS, 440, 1607

Batygin, K., Brown, M. E., 2016, aj, 151, 22

Becklin, E. E., Farihi, J., Jura, M., Song, I., Weinberger, A. J., Zuckerman, B., 2005, ApJ Lett., 632, L119

Belardi, C., Kilic, M., Munn, J. A., Gianninas, A., Barber, S. D., Dey, A., Stetson, P. B., 2016, MNRAS, 462, 2506

Bergeron, P., Saffer, R. A., Liebert, J., 1992, ApJ, 394, 228

Bergeron, P., et al., 2011, ApJ, 737, 28

Bond, J. C., O'Brien, D. P., Lauretta, D. S., 2010, ApJ, 715, 1050

Bonsor, A., Farihi, J., Wyatt, M. C., van Lieshout, R., 2017, MNRAS, 468, 154

Braker, I. P., Burleigh, M. R., Lawrie, K. A., Faedi, F., Goad, M. R., West, R. G., 2015, in Dufour, P., Bergeron, P., Fontaine, G., eds., 19th European Workshop on White Dwarfs, vol. 493 of *Astronomical Society of the Pacific Conference Series*, p. 295

Brinkworth, C. S., Gänsicke, B. T., Marsh, T. R., Hoard, D. W., Tappert, C., 2009, ApJ, 696, 1402

Brinkworth, C. S., Gänsicke, B. T., Girven, J. M., Hoard, D. W., Marsh, T. R., Parsons, S. G., Koester, D., 2012, ApJ, 750, 86

Brown, J. C., Veras, D., Gänsicke, B. T., 2017, MNRAS, 468, 1575

Brown, J. M., Kilic, M., Brown, W. R., Kenyon, S. J., 2011, ApJ, 730, 67

Burleigh, M. R., et al., 2011, in Schuh, S., Drechsel, H., Heber, U., eds., American Institute of Physics Conference Series, vol. 1331 of *American Institute of Physics Conference Series*, p. 289

Cameron, A. G. W., 1985, Icarus, 64, 285

Carrasco, J. M., Catalán, S., Jordi, C., Tremblay, P.-E., Napiwotzki, R., Luri, X., Robin, A. C., Kowalski, P. M., 2014, A&A, 565, A11

Casewell, S. L., Dobbie, P. D., Napiwotzki, R., Burleigh, M. R., Barstow, M. A., Jameson, R. F., 2009, MNRAS, 395, 1795

Catalán, S., Isern, J., García-Berro, E., Ribas, I., 2008, MNRAS, 387, 1693

Chayer, P., 2014, MNRAS, 437, L95

Chayer, P., Dupuis, J., 2010a, in Werner, K., Rauch, T., eds., American Institute of Physics Conference Series, vol. 1273 of *American Institute of Physics Conference Series*, p. 394

Chayer, P., Dupuis, J., 2010b, in Werner, K., Rauch, T., eds., American Institute of Physics Conference Series, vol. 1273 of *American Institute of Physics Conference Series*, p. 394

Chayer, P., Leblanc, F., Fontaine, G., Wesemael, F., Michaud, G., Vennes, S., 1994, ApJ Lett., 436, L161

Chayer, P., Fontaine, G., Wesemael, F., 1995a, ApJS, 99, 189

Chayer, P., Vennes, S., Pradhan, A. K., Thejll, P., Beauchamp, A., Fontaine, G., Wesemael, F., 1995b, ApJ, 454, 429

Chayer, P., Kruk, J. W., Ake, T. B., Dupree, A. K., Malina, R. F., Siegmund, O. H. W., Sonneborn, G., Ohl, R. G., 2000, ApJ Lett., 538, L91

Chen, Y.-P., Trager, S. C., Peletier, R. F., Lançon, A., Vazdekis, A., Prugniel, P., Silva, D. R., Gonneau, A., 2014, A&A, 565, A117

Choi, J., Dotter, A., Conroy, C., Cantiello, M., Paxton, B., Johnson, B. D., 2016, ApJ, 823, 102

Clemens, J. C., et al., 1992, ApJ, 391, 773

Dalton, G., et al., 2014, in Ground-based and Airborne Instrumentation for Astronomy V, vol. 9147 of *Proceedings of SPIE*, p. 91470L

Davidsson, B. J. R., 1999, Icarus, 142, 525

de Jong, R. S., et al., 2014, in Ground-based and Airborne Instrumentation for Astronomy V, vol. 9147 of *Proceedings of SPIE*, p. 91470M

Debes, J. H., Sigurdsson, S., 2002, ApJ, 572, 556

Debes, J. H., Walsh, K. J., Stark, C., 2012, ApJ, 747, 148

Dekker, H., D'Odorico, S., Kaufer, A., Delabre, B., Kotzlowski, H., 2000, in Iye, M., Moorwood, A. F., eds., Optical and IR Telescope Instrumentation and Detectors, vol. 4008 of *Society of Photo-Optical Instrumentation Engineers (SPIE) Conference Series*, p. 534

Deming, D., et al., 2013, ApJ, 774, 95

Desharnais, S., Wesemael, F., Chayer, P., Kruk, J. W., Saffer, R. A., 2008, ApJ, 672, 540

Dhillon, V. S., et al., 2007, MNRAS, 378, 825

Dickinson, N. J., Barstow, M. A., Welsh, B. Y., Burleigh, M., Farihi, J., Redfield, S., Unglaub, K., 2012, MNRAS, 423, 1397

Dotter, A., 2016, ApJS, 222, 8

Dressing, C. D., et al., 2015, ApJ, 800, 135

Dufour, P., Bergeron, P., Fontaine, G., 2005, ApJ, 627, 404

Dufour, P., Liebert, J., Fontaine, G., Behara, N., 2007, Nat, 450, 522

Dufour, P., Fontaine, G., Liebert, J., Schmidt, G. D., Behara, N., 2008, ApJ, 683, 978

Dufour, P., Kilic, M., Fontaine, G., Bergeron, P., Melis, C., Bochanski, J., 2012, ApJ, 749, 6

Dufour, P., Blouin, S., Coutu, S., Fortin-Archambault, M., Thibeault, C., Bergeron, P., Fontaine, G., 2017, in Tremblay, P.-E., Gaensicke, B., Marsh, T., eds., 20th European White Dwarf Workshop, vol. 509 of *Astronomical Society of the Pacific Conference Series*, p. 3

Duncan, M. J., Lissauer, J. J., 1998, Icarus, 134, 303

Dupuis, J., Chayer, P., Vennes, S., Christian, D. J., Kruk, J. W., 2000, ApJ, 537, 977

Faedi, F., West, R. G., Burleigh, M. R., Goad, M. R., Hebb, L., 2011, MNRAS, 410, 899

Farihi, J., 2016, New Astronomy Reviews, 71, 9

Farihi, J., Parsons, S. G., Gänsicke, B. T., ????

Farihi, J., Jura, M., Zuckerman, B., 2009, ApJ, 694, 805

Farihi, J., Barstow, M. A., Redfield, S., Dufour, P., Hambly, N. C., 2010, MNRAS, 404, 2123

Farihi, J., Gänsicke, B. T., Steele, P. R., Girven, J., Burleigh, M. R., Breedt, E., Koester, D., 2012, MNRAS, 421, 1635

Farihi, J., Gänsicke, B. T., Koester, D., 2013a, Science, 342, 218

Farihi, J., Gänsicke, B. T., Koester, D., 2013b, MNRAS, 432, 1955

Finley, D. S., Basri, G., Bowyer, S., 1990, ApJ, 359, 483

Finley, D. S., Koester, D., Basri, G., 1997, ApJ, 488, 375

Flaugher, B., Bebek, C., 2014, in Ground-based and Airborne Instrumentation for Astronomy V, vol. 9147 of *Proceedings of SPIE*, p. 91470S

Fontaine, G., Brassard, P., 2005, in Koester, D., Moehler, S., eds., 14th European Workshop on White Dwarfs, vol. 334 of *Astronomical Society of the Pacific Conference Series*, p. 49

Fontaine, G., Michaud, G., 1979, ApJ, 231, 826

Fontaine, G., Brassard, P., Bergeron, P., 2001, PASP, 113, 409

Fortney, J. J., 2012, ApJ Lett., 747, L27

Gaia Collaboration, et al., 2016, 595, A1

Gaidos, E., 2015, ApJ, 804, 40

Gänsicke, B. T., 2011, in Schuh, S., Drechsel, H., Heber, U., eds., American Institute of Physics Conference Series, vol. 1331 of *American Institute of Physics Conference Series*, p. 211

Gänsicke, B. T., Marsh, T. R., Southworth, J., Rebassa-Mansergas, A., 2006, Science, 314, 1908

Gänsicke, B. T., Marsh, T. R., Southworth, J., 2007, MNRAS, 380, L35

Gänsicke, B. T., Koester, D., Marsh, T. R., Rebassa-Mansergas, A., Southworth, J., 2008, MNRAS, 391, L103

Gänsicke, B. T., Koester, D., Girven, J., Marsh, T. R., Steeghs, D., 2010, Science, 327, 188

Gänsicke, B. T., Koester, D., Farihi, J., Girven, J., Parsons, S. G., Breedt, E., 2012, MNRAS, 424, 333

Gänsicke, B. T., et al., 2016, ApJ Lett., 818, L7

Gardner, J. P., et al., 2006, Space Sci. Rev., 123, 485

Genest-Beaulieu, C., Bergeron, P., 2014, ApJ, 796, 128

Gentile Fusillo, N. P., Gänsicke, B. T., Farihi, J., Koester, D., Schreiber, M. R., Pala, A. F., 2017, MNRAS, 468, 971

Gesicki, K., Zijlstra, A. A., Hajduk, M., Szyszka, C., 2014, A&A, 566, A48

Gianninas, A., Bergeron, P., Ruiz, M. T., 2011, ApJ, 743, 138

Gilmozzi, R., Spyromilio, J., 2007, The Messenger, 127

Girven, J., Brinkworth, C. S., Farihi, J., Gänsicke, B. T., Hoard, D. W., Marsh, T. R., Koester, D., 2012, ApJ, 749, 154

Graham, J. R., Matthews, K., Neugebauer, G., Soifer, B. T., 1990, ApJ, 357, 216

Green, J. C., et al., 2012, ApJ, 744, 60

Green, R. F., Schmidt, M., Liebert, J., 1986, ApJS, 61, 305

Grossman, L., 1972, Geochim. Cosmochim. Acta, 36, 597

Guo, J., Tziamtzis, A., Wang, Z., Liu, J., Zhao, J., Wang, S., 2015, ApJ Lett., 810, L17

Gurri, P., Veras, D., Gänsicke, B. T., 2017, MNRAS, 464, 321

Han, E., Wang, S. X., Wright, J. T., Feng, Y. K., Zhao, M., Fakhouri, O., Brown, J. I., Hancock, C., 2014, PASP, 126, 827

Hartmann, S., Nagel, T., Rauch, T., Werner, K., 2011, A&A, 530, A7

Hartmann, S., Nagel, T., Rauch, T., Werner, K., 2014, A&A, 571, A44

Haswell, C. A., et al., 2012, ApJ, 760, 79

Holberg, J. B., Bergeron, P., 2006, AJ, 132, 1221

Holberg, J. B., Basile, J., Wesemael, F., 1986, ApJ, 306, 629

Holberg, J. B., Barstow, M. A., Sion, E. M., 1998, 119, 207

Hollands, M. A., Koester, D., Alekseev, V., Herbert, E. L., Gänsicke, B. T., 2017, MNRAS, 467, 4970

Hook, I. M., Jørgensen, I., Allington-Smith, J. R., Davies, R. L., Metcalfe, N., Murowinski, R. G., Crampton, D., 2004, PASP, 116, 425

Horne, K., Marsh, T. R., 1986, MNRAS, 218, 761

Hubeny, I., 1988, Comput.,Phys.,Comm., 52, 103

Hubeny, I., Lanz, T., 1995, ApJ, 439, 875

Hubeny, I., Lanz, T., 2011, Synspec: General Spectrum Synthesis Program, Astrophysics Source Code Library

Ivezić, Ž., et al., 2007, AJ, 134, 973

Jensen, K. A., Swank, J. H., Petre, R., Guinan, E. F., Sion, E. M., Shipman, H. L., 1986, ApJ Lett., 309, L27

Jessberger, E. K., Christoforidis, A., Kissel, J., 1988, Nat, 332, 691

Johns, M., et al., 2012, in Ground-based and Airborne Telescopes IV, vol. 8444 of *Proceedings of SPIE*, p. 84441H

Jordan, S., 2015, in Dufour, P., Bergeron, P., Fontaine, G., eds., 19th European Workshop on White Dwarfs, vol. 493 of *Astronomical Society of the Pacific Conference Series*, p. 443

Jura, M., 2003, ApJ Lett., 584, L91

Jura, M., 2006, ApJ, 653, 613

Jura, M., 2008, AJ, 135, 1785

Jura, M., Xu, S., 2012, AJ, 143, 6

Jura, M., Young, E. D., 2014, Annual Review of Earth and Planetary Sciences, 42, 45

Jura, M., Xu, S., Klein, B., Koester, D., Zuckerman, B., 2012, ApJ, 750, 69

Jura, M., Dufour, P., Xu, S., Zuckerman, B., Klein, B., Young, E. D., Melis, C., 2015, ApJ, 799, 109

Kalirai, J. S., Hansen, B. M. S., Kelson, D. D., Reitzel, D. B., Rich, R. M., Richer, H. B., 2008, ApJ, 676, 594

Kepler, S. O., Koester, D., Ourique, G., 2016, Science, 352, 67

Kepler, S. O., et al., 2015, MNRAS, 446, 4078

Kidder, K. M., Holberg, J. B., Mason, P. A., 1991, AJ, 101, 579

Kilic, M., von Hippel, T., Leggett, S. K., Winget, D. E., 2005, ApJ Lett., 632, L115

Kilic, M., Stanek, K. Z., Pinsonneault, M. H., 2007, ApJ, 671, 761

Kilkenny, D., 1986, The Observatory, 106, 201

King, A. R., Pringle, J. E., Livio, M., 2007, 376, 1740

Kinnear, T., 2011, Irradiated Gaseous Discs Around White Dwarfs, Master's thesis, University of Warwick

Klein, B., Jura, M., Koester, D., Zuckerman, B., 2011, ApJ, 741, 64

Kleinman, S. J., et al., 2013, ApJS, 204, 5

Koester, D., 2009, A&A, 498, 517

Koester, D., 2010, Memorie della Societa Astronomica Italiana,, 81, 921

Koester, D., 2013, White Dwarf Stars, p. 559

Koester, D., Kepler, S. O., 2015, 583, A86

Koester, D., Knist, S., 2006, A&A, 454, 951

Koester, D., Wilken, D., 2006, A&A, 453, 1051

Koester, D., Weidemann, V., Zeidler, E.-M., 1982, A&A, 116, 147

Koester, D., Provencal, J., Shipman, H. L., 1997, A&A, 320, L57

Koester, D., Gänsicke, B. T., Farihi, J., 2014a, A&A, 566, A34

Koester, D., Provencal, J., Gänsicke, B. T., 2014b, A&A, 568, A118

Kowalski, P. M., Saumon, D., 2006, ApJ Lett., 651, L137

Kreidberg, L., et al., 2014, Nat, 505, 69

Kuchner, M. J., Seager, S., 2005, ArXiv e-prints

Lajoie, C., Bergeron, P., 2007, ApJ, 667, 1126

Lallement, R., Welsh, B. Y., Barstow, M. A., Casewell, S. L., 2011, 533, A140

Lawlor, T. M., MacDonald, J., 2006, MNRAS, 371, 263

Liebert, J., Bergeron, P., Holberg, J. B., 2005, ApJS, 156, 47

Lodders, K., 2003, ApJ, 591, 1220

Lodders, K., Fegley, B., 1998, The planetary scientist's companion, Oxford University Press, New York

Lodders, K., Fegley, B., 2011, Chemistry of the Solar System, RSC Publishing, Cambrige

Long, K. S., Gilliland, R. L., 1999, ApJ, 511, 916

Long, K. S., Brammer, G., Froning, C. S., 2006, ApJ, 648, 541

LSST Science Collaboration, et al., 2009, arXiv:0912.0201

Luhman, K. L., Burgasser, A. J., Bochanski, J. J., 2011, ApJ Lett., 730, L9+

Luyten, W. J., 1922a, PASP, 34, 132

Luyten, W. J., 1922b, PASP, 34, 356

Manser, C. J., Gänsicke, B. T., Koester, D., Marsh, T. R., Southworth, J., 2016a, MNRAS, 462, 1461

Manser, C. J., et al., 2016b, MNRAS, 455, 4467

Marsh, M. C., et al., 1997, MNRAS, 287, 705

Marsh, T. R., 1989, PASP, 101, 1032

Marty, B., 2012, Earth and Planetary Science Letters, 313, 56

McCook, G. P., Sion, E. M., 1999, ApJS, 121, 1

McDonough, W., 2000, in Teisseyre, R., Majewski, E., eds., Earthquake Thermodynamics and Phase Transformation in the Earth's Interior, Elsevier Science Academic Press, p. 5

McMahan, R. K., 1989, ApJ, 336, 409

Melis, C., Jura, M., Albert, L., Klein, B., Zuckerman, B., 2010, ApJ, 722, 1078

Melis, C., Farihi, J., Dufour, P., Zuckerman, B., Burgasser, A. J., Bergeron, P., Bochanski, J., Simcoe, R., 2011, ApJ, 732, 90

Melis, C., et al., 2012, ApJ Lett., 751, L4

Metzger, B. D., Rafikov, R. R., Bochkarev, K. V., 2012, MNRAS, 423, 505

Mordasini, C., van Boekel, R., Mollière, P., Henning, T., Benneke, B., 2016, ApJ, 832, 41

Moriarty, J., Madhusudhan, N., Fischer, D., 2014, ApJ, 787, 81

Mullally, F., Kilic, M., Reach, W. T., Kuchner, M. J., von Hippel, T., Burrows, A., Winget, D. E., 2007, ApJS, 171, 206

Mustill, A. J., Villaver, E., 2012, ApJ, 761, 121

Nelemans, G., 2010, Ap&SS, 329, 25

Nelemans, G., Tauris, T. M., 1998, A&A, 335, L85

Nittler, L. R., McCoy, T. J., Clark, P. E., Murphy, M. E., Trombka, J. I., Jarosewich, E., 2004, Antarctic Meteorite Research, 17, 231

Öberg, K. I., Murray-Clay, R., Bergin, E. A., 2011, ApJ Lett., 743, L16

Ofek, E. O., et al., 2012, PASP, 124, 62

Paquette, C., Pelletier, C., Fontaine, G., Michaud, G., 1986, ApJS, 61, 177

Patterson, J., Raymond, J. C., 1985, ApJ, 292, 535

Pelletier, C., Fontaine, G., Wesemael, F., Michaud, G., Wegner, G., 1986, ApJ, 307, 242

Poirier, J.-P., 1994, Physics of the Earth and Planetary Interiors, 85, 319

Pollacco, D. L., et al., 2006, PASP, 118, 1407

Provencal, J. L., Shipman, H. L., Thejll, P., Vennes, S., 2000, ApJ, 542, 1041

Raddi, R., Gänsicke, B. T., Koester, D., Farihi, J., Hermes, J. J., Scaringi, S., Breedt, E., Girven, J., 2015, 450, 2083

Rafikov, R. R., 2011, MNRAS, 416, L55

Rappaport, S., Gary, B. L., Kaye, T., Vanderburg, A., Croll, B., Benni, P., Foote, J., 2016, MNRAS, 458, 3904

Rauer, H., et al., 2014, Experimental Astronomy, 38, 249

Reach, W. T., Lisse, C., von Hippel, T., Mullally, F., 2009, ApJ, 693, 697

Rebassa-Mansergas, A., Nebot Gómez-Morán, A., Schreiber, M. R., Girven, J., Gänsicke, B. T., 2011, MNRAS, 413, 1121

Redfield, S., Farihi, J., Cauley, P. W., Parsons, S. G., Gänsicke, B. T., Duvvuri, G. M., 2017, ApJ, 839, 42

Ricker, G. R., et al., 2015, Journal of Astronomical Telescopes, Instruments, and Systems, 1, 014003

Rocchetto, M., Farihi, J., Gänsicke, B. T., Bergfors, C., 2015, MNRAS, 449, 574

Rodriguez, D. R., Zuckerman, B., Melis, C., Song, I., 2011, ApJ Lett., 732, L29

Sackmann, I.-J., Boothroyd, A. I., Kraemer, K. E., 1993, ApJ, 418, 457

Saffer, R. A., Livio, M., Yungelson, L. R., 1998, ApJ, 502, 394

Sandhaus, P. H., Debes, J. H., Ely, J., Hines, D. C., Bourque, M., 2016, ApJ, 823, 49

Saumon, D., Chabrier, G., van Horn, H. M., 1995, 99, 713

Schlafly, E. F., Finkbeiner, D. P., 2011, ApJ, 737, 103

Schröder, K.-P., Connon Smith, R., 2008, MNRAS, 386, 155

Schuh, S. L., Dreizler, S., Wolff, B., 2002, 382, 164

Seager, S., Kuchner, M., Hier-Majumder, C. A., Militzer, B., 2007, ApJ, 669, 1279

Sfeir, D. M., Lallement, R., Crifo, F., Welsh, B. Y., 1999, 346, 785

Shipman, H. L., et al., 1995, AJ, 109, 1220

Siess, L., 2007, 476, 893

Silvotti, R., Sozzetti, A., Lattanzi, M., Morbidelli, R., 2015, in Dufour, P., Bergeron, P., Fontaine, G., eds., 19th European Workshop on White Dwarfs, vol. 493 of *Astronomical Society of the Pacific Conference Series*, p. 455

Sion, E. M., Cheng, F. H., Szkody, P., Sparks, W., Gänsicke, B., Huang, M., Mattei, J., 1998, ApJ, 496, 449

Skidmore, W., TMT International Science Development Teams, Science Advisory Committee, T., 2015, Research in Astronomy and Astrophysics, 15, 1945

Sohl, F., Wagner, F. W., Rauer, H., 2012, ArXiv e-prints

Teske, J. K., Cunha, K., Schuler, S. C., Griffith, C. A., Smith, V. V., 2013, ApJ, 778, 132

Thiabaud, A., Marboeuf, U., Alibert, Y., Leya, I., Mezger, K., 2015, 580, A30

Tremblay, P.-E., Bergeron, P., 2009, ApJ, 696, 1755

Tremblay, P.-E., Bergeron, P., Gianninas, A., 2011a, ApJ, 730, 128

Tremblay, P.-E., Ludwig, H.-G., Steffen, M., Bergeron, P., Freytag, B., 2011b, A&A, 531, L19+

Tremblay, P.-E., Cummings, J., Kalirai, J. S., Gänsicke, B. T., Gentile-Fusillo, N., Raddi, R., 2016, MNRAS, 461, 2100

Tremblay, P.-E., et al., 2017, MNRAS, 465, 2849

Tripathi, A., Kratter, K. M., Murray-Clay, R. A., Krumholz, M. R., 2015, ApJ, 808, 173

Unterborn, C. T., Hull, S. D., Stixrude, L. P., Teske, J. K., Johnson, J. A., Panero, W. R., 2017, ArXiv e-prints

van Maanen, A., 1917, PASP, 29, 258

van Maanen, A., 1919, PASP, 31, 42

Vanderburg, A., et al., 2015, Nat, 526, 546

Vennes, S., 1992, ApJ, 390, 590

Vennes, S., Thejll, P. A., Galvan, R. G., Dupuis, J., 1997, ApJ, 480, 714

Vennes, S., Chayer, P., Dupuis, J., Lanz, T., 2006, ApJ, 652, 1554

Vennes, S., Kawka, A., Németh, P., 2010, MNRAS, 404, L40

Vennes, S., Kawka, A., Németh, P., 2011, MNRAS, 413, 2545

Veras, D., 2016a, Royal Society Open Science, 3, 150571

Veras, D., 2016b, MNRAS, 463, 2958

Veras, D., Gänsicke, B. T., 2015, MNRAS, 447, 1049

Veras, D., Jacobson, S. A., Gänsicke, B. T., 2014a, MNRAS, 445, 2794

Veras, D., Leinhardt, Z. M., Bonsor, A., Gänsicke, B. T., 2014b, MNRAS, 445, 2244

Veras, D., Shannon, A., Gänsicke, B. T., 2014c, MNRAS, 445, 4175

Veras, D., Carter, P. J., Leinhardt, Z. M., Gänsicke, B. T., 2017, MNRAS, 465, 1008

Vernet, J., et al., 2011, A&A, 536, A105

Vidal-Madjar, A., Lecavelier des Etangs, A., Désert, J.-M., Ballester, G. E., Ferlet, R., Hébrard, G., Mayor, M., 2003, Nat, 422, 143

Villaver, E., Livio, M., 2007, ApJ, 661, 1192

Vogt, S. S., et al., 1994, in Crawford, D. L., Craine, E. R., eds., Instrumentation in Astronomy VIII, vol. 2198 of *Proceedings of SPIE*, p. 362

Vollmann, K., Eversberg, T., 2006, Astronomische Nachrichten, 327, 862

von Hippel, T., Kuchner, M. J., Kilic, M., Mullally, F., Reach, W. T., 2007, ApJ, 662, 544

von Steiger, R., Zurbuchen, T. H., 2016, ApJ, 816, 13

Weidemann, V., Koester, D., 1995, A&A, 297, 216

Weidenschilling, S. J., 1978, Icarus, 35, 99

Weiss, L. M., Marcy, G. W., 2014, ApJ Lett., 783, L6

Williams, K. A., Bolte, M., Koester, D., 2009, ApJ, 693, 355

Wilson, D. J., Gänsicke, B. T., Koester, D., Raddi, R., Breedt, E., Southworth, J., Parsons, S. G., 2014, MNRAS, 445, 1878

Wilson, D. J., Gänsicke, B. T., Koester, D., Toloza, O., Pala, A. F., Breedt, E., Parsons, S. G., 2015, MNRAS, 451, 3237

Wilson, D. J., Gänsicke, B. T., Farihi, J., Koester, D., 2016, MNRAS

Wolszczan, A., Frail, D. A., 1992, Nat, 355, 145

Wyatt, M. C., Farihi, J., Pringle, J. E., Bonsor, A., 2014, MNRAS, 439, 3371

Xu, S., Jura, M., 2014, ApJ Lett., 792, L39

Xu, S., Jura, M., Klein, B., Koester, D., Zuckerman, B., 2013, ApJ, 766, 132

Xu, S., Jura, M., Koester, D., Klein, B., Zuckerman, B., 2014, ApJ, 783, 79

Xu, S., Jura, M., Dufour, P., Zuckerman, B., 2016, ApJ Lett., 816, L22

Xu, S., Zuckerman, B., Dufour, P., Young, E. D., Klein, B., Jura, M., 2017, ApJ Lett., 836, L7

Zhang, Y., Yin, Q.-Z., 2012, Proceedings of the National Academy of Science, 109, 19579

Zorotovic, M., Schreiber, M. R., 2017, MNRAS, 466, L63

Zuckerman, B., 2014, ArXiv e-prints no. 1410.2575

Zuckerman, B., Becklin, E. E., 1987, Nat, 330, 138

Zuckerman, B., Koester, D., Reid, I. N., Hünsch, M., 2003, ApJ, 596, 477

Zuckerman, B., Koester, D., Melis, C., Hansen, B. M., Jura, M., 2007, ApJ, 671, 872

Zuckerman, B., Melis, C., Klein, B., Koester, D., Jura, M., 2010, ApJ, 722, 725

Zuckerman, B., Koester, D., Dufour, P., Melis, C., Klein, B., Jura, M., 2011, ApJ, 739, 101